THE UNIVERSITY OF QUEENSLAND

AUSTRALIA

FORMATION AND DYNAMICAL EVOLUTION OF YOUNG STAR CLUSTERS: UNCOVERING THE MYSTERY OF MULTIPLE STELLAR POPULATIONS

Pouria Khalaj

Bachelor of Science (Physics)

A thesis submitted for the degree of Doctor of Philosophy at

The University of Queensland in 2016

School of Mathematics and Physics

Abstract

Many observations and theoretical models suggest that stars form in groups or clusters and then scatter into their host Galaxy. Star clusters provide us with rich samples of stars of known distance, metallicity and age. In addition, stars in a cluster cover a wide spectrum of masses and are consequently in different phases of their evolution. Therefore, star clusters can be viewed as the Rosetta Stone of star formation and evolution. In this thesis, I study the formation and dynamical evolution of open and globular clusters (OCs and GCs) through the use of N-body and Monte Carlo simulations.

The thesis starts by devising a novel approach to find the mass function and binary fraction of OCs (Chapter 2). My method to find the mass function is based on a maximum likelihood approach combined with a Kolmogorov Smirnov test and is more accurate than typical least squares methods. I then apply my method to Praesepe as an example of a young OC in the Milky Way, using photometric and astrometric data from the SDSS and PPMXL catalogues. I find the possible cluster members of Praesepe using the proper motions of stars in the field of the cluster followed by comparing the position of possible members in a colour-magnitude (CMD) diagram with theoretical isochrones. To find the binary fraction, I perform a series of Monte Carlo simulations to compare the observed CMD of Praesepe with synthetic isochrones. My method can be readily used with *Gaia* data to robustly correct the mass function of OCs for the effect of unresolved binaries.

The remainder of the thesis is devoted to the study of globular clusters (GCs), which are older and more massive than OCs. In particular I focus on the origin of multiple stellar populations (MSPs) whose origin has remained a mystery despite almost a decade of intense research.

Chapter 3 discusses the so-called mass budget problem in GCs with MSPs. First, I study the effect of a top heavy initial mass function (IMF) on the fraction of chemically peculiar stars as well as the mass-to-light ratio of GCs with MSPs. I consider two different cases for the origin of MSPs, i.e. asymptotic giant branch (AGB) stars and fast-rotating massive stars (FRMS). In addition, I consider different retention fractions for compact remnants as well as different mass-loss levels.

For both the AGB and FRMS scenario, I derive the range of IMF high-mass slopes and mass-loss levels which produce the observed fraction of chemically peculiar stars and mass-to-light ratios of Galactic GCs. I then show that the higher helium abundance and shorter lifetimes of chemically peculiar stars in conjunction with the fact that stellar mass functions strongly increase towards lower masses, boosts the fraction of chemically peculiar stars which have left the main sequence. This implies that one needs to correct the observed number ratio of evolved chemically peculiar stars to infer the actual number ratio.

I then study the effect of primordial gas expulsion and its link to significant mass loss in globular clusters with multiple stellar populations in Chapter 4. By comparing the outcome of my N-body and Monte Carlo simulations with the observational data of Galactic GCs, I determine the initial mass and size of GCs as well as the gas expulsion time scales required to explain the large fraction of chemically peculiar stars in GCs with MSPs. Moreover, I show that primordial gas expulsion leads to an anti-correlation between the final mass of GCs and the observed number fraction of such stars which is not supported by observations.

In Chapter 5, I address the question of whether significant mass-loss induced by primordial gas expulsion could have happened in the GCs of the Fornax dwarf spheroidal galaxy. Recently, Larsen et al. (2012) found a large ratio of metal poor GCs to field stars in Fornax. This large ratio limits the maximum amount of mass-loss that could have happened in Fornax GCs to 80%. This is considered as evidence against significant mass-loss in GCs that require mass-loss levels of $\sim 90\%$ or more to explain the observed large fraction of chemically peculiar stars in GCs with MSPs. Using a series of numerical simulations (orbit integration) I provide a solution to this problem. I follow the orbit of unbound stars of Fornax GCs in the potential field of Fornax and the Milky Way over a Hubble time. I demonstrate that stars can leave the Fornax galaxy if they have become unbound as a result of gas expulsion but not if they have become unbound due to stellar evolution.

Finally I conclude the thesis in Chapter 6 by stating the major outcomes of my study and their implications and also suggest a number of possible research directions for future work.

Declaration by author

This thesis is composed of my original work, and contains no material previously published or written by another person except where due reference has been made in the text. I have clearly stated the contribution by others to jointly-authored works that I have included in my thesis.

I have clearly stated the contribution of others to my thesis as a whole, including statistical assistance, survey design, data analysis, significant technical procedures, professional editorial advice, and any other original research work used or reported in my thesis. The content of my thesis is the result of work I have carried out since the commencement of my research higher degree candidature and does not include a substantial part of work that has been submitted to qualify for the award of any other degree or diploma in any university or other tertiary institution. I have clearly stated which parts of my thesis, if any, have been submitted to qualify for another award.

I acknowledge that an electronic copy of my thesis must be lodged with the University Library and, subject to the policy and procedures of The University of Queensland, the thesis be made available for research and study in accordance with the Copyright Act 1968 unless a period of embargo has been approved by the Dean of the Graduate School.

I acknowledge that copyright of all material contained in my thesis resides with the copyright holder(s) of that material. Where appropriate I have obtained copyright permission from the copyright holder to reproduce material in this thesis.

Publications during candidature

Peer-reviewed publications

- **Khalaj P.**, Baumgardt H., 2013, MNRAS, 434, 3236, arXiv:1307.2020: *The stellar mass function, binary content and radial structure of the open cluster Praesepe derived from PP-MXL and SDSS data*

- **Khalaj P.**, Baumgardt H., 2015, MNRAS, 452, 924, arXiv:1506.05303: *Dynamical constraints on the origin of multiple stellar populations in globular clusters*

- **Khalaj P.**, Baumgardt H., 2016, MNRAS, 457, 479, arXiv:1512.05260: *Limits on the significant mass-loss scenario based on the globular cluster of the Fornax dwarf spheroidal galaxy*

- Sheikhi N., Hasheminia M., **Khalaj P.**, Haghi H., Zonoozi A. H., Baumgardt H., 2016, MNRAS, 457, 1028, arXiv:1601.02186: *The Binary Fraction and Mass Segregation in Alpha Persei Open Cluster*

Publications included in this thesis

Paper One (incorporated as Chapter 2)

Khalaj P., Baumgardt H., 2013, MNRAS, 434, 3236, arXiv:1307.2020: *The stellar mass function, binary content and radial structure of the open cluster Praesepe derived from PPMXL and SDSS data*

Contributor	Statement of contribution
Pouria Khalaj (Candidate)	Design of the project (50%)
	Implementation and data analysis (100%)
	Wrote and edited paper (95%)
Holger Baumgardt	Design of the project (50%)
	Wrote and edited paper (5%)

Paper Two (incorporated as Chapter 4)

Khalaj P., Baumgardt H., 2015, MNRAS, 452, 924, arXiv:1506.05303: *Dynamical constraints on the origin of multiple stellar populations in globular clusters*

Contributor	Statement of contribution
Pouria Khalaj (Candidate)	Design of the project (70%)
	Implementation and data analysis (100%)
	Wrote and edited paper (95%)
Holger Baumgardt	Design of the project (30%)
	Wrote and edited paper (5%)

Paper Three (incorporated as Chapter 5)

Khalaj P., Baumgardt H., 2016, MNRAS, 457, 479, arXiv:1512.05260: *Limits on the significant mass-loss scenario based on the globular cluster of the Fornax dwarf spheroidal galaxy*

Contributor	Statement of contribution
Pouria Khalaj (Candidate)	Design of the project (80%)
	Implementation and data analysis (100%)
	Wrote and edited paper (95%)
Holger Baumgardt	Design of the project (20%)
	Wrote and edited paper (5%)

Contributions by others to the thesis

No contributions by others.

Statement of parts of the thesis submitted to qualify for the award of another degree

None.

Acknowledgements

I would like to express my gratitude to my principal supervisor Holger Baumgardt who is not only a great advisor but also a kind and a humble person. I enjoyed every moment of working with him and I owe my progress in PhD and the knowledge that I have gained to his mentorship. I also thank my second supervisor Michael Drinkwater for his invaluable feedback and comments.

I would like to thank Hosein Haghi and Elham Zonoozi who walked me through the first steps of this field. I appreciate their hospitality during my visits to the Institute for Advanced Studies in Basic Sciences in Zanjan.

I thank Pavel Kroupa and Corinne Charbonnel for giving me the opportunity to present my work at the Argelander Institute for Astronomy in Bonn and the International Space Science Institute in Bern respectively.

I am grateful to my friends and all the members of the UQ astro group who warmly welcomed me and created many memorable moments for me here in Australia. My sincere thanks to David Parkinson who helped me with my mid-candidature and thesis review milestones. In addition, a big thank you to all the staff of the School of Mathematics and Physics, in particular the postgraduate research administration officer, Murray Kane.

I wish to thank my beloved family. I owe a great debt of gratitude to my parents and my fiancée Elmira for their support, love, patience and encouragement.

Keywords

dynamical evolution, fornax dsph, gas expulsion, globular clusters, mass function, multiple stellar populations, numerical simulations, open clusters

Australian and New Zealand Standard Research Classifications (ANZSRC)

ANZSRC code: 020103 Cosmology and Extragalactic Astronomy: 10%

ANZSRC code: 020104 Galactic Astronomy: 90%

Fields of Research (FoR) Classification

FoR code: 0201, Astronomical and Space Sciences, 100%

Contents

List of Figures

List of Tables

List of Abbreviations and Symbols

2MASS	2-Micron All-Sky Survey
2D	two-dimensional, projected
$\langle x \rangle$	expected value of x
AGB	Asymptotic Giant Branch (stars)
Al	Aluminum
a	scale radius of the plummer model
a_g	plummer scale radius of the gas reservoir
a_1	plummer scale radius of FG stars
a_2	plummer scale radius of SG stars
α_{high}	index of the power-law mass function at the high-mass end
α_{low}	index of the power-law mass function at the low-mass end
CMD	Colour Magnitude Diagram
deg	degree
dSph	Dwarf spheroidal (galaxy)
e	eccentricity
$\exp(x)$	the natural exponential function, i.e. e^x
f_{bin}	binary fraction
FG	First Generation (stars), stars with normal abundance
FRMS	Fast Rotating Massive Stars
γ	logarithmic density slope
GC	Globular Cluster
GMC	Giant Molecular Cloud
GPU	Graphics Processing Unit
Gyr	gigayear

He   Helium

IMF   Initial Mass Function

kpc   kiloparsec

K-S   Kolmogorov Smirnov

λ ratio of the scale-radius of the density profile SG to FG stars, i.e. $\lambda \equiv a_2/a_1$

IC   Intermediate Cusp

LC   Large Core

$\mathcal{L}$ logarithm of the likelihood

log   base-10 logarithm, i.e. $\log \equiv \log_{10}$

LMC   Large Magellanic Cloud

$L_\odot$ Solar luminosity

mag   magnitude, unit of brightness

$\mathrm{mas\,yr^{-1}}$ milliarcseconds per year

M_c cluster mass

MC   Monte Carlo

MD   Mass Dependant

Mg   Magnesium

M_g mass of the gas reservoir in the cluster

MI   Mass Independent

MSPs   Multiple Stellar Populations

$M_\star$ stellar mass

$M_\odot$ Solar mass

m_t turnover point of the mass-function

μ proper motion

Myr   megayear

Na   Sodium

O   Oxygen

OC   Open Cluster

Ω angular velocity

ω Cen   Omega Centauri

Υ mass to light ratio, i.e. $\Upsilon \equiv M/L$

pc   parsec

ϕ	gravitational potential
PPMXL	Positions and Proper Motions Extended Large (Catalogue)
R_a	apocentric distance of the orbit
R_G	distance of the object with respect to the host galaxy
R_p	pericentric distance of the orbit
$R_\mathrm{c}, r_\mathrm{c}$	core radius
$R_\mathrm{h}, r_\mathrm{h}$	half-mass radius
ρ	mass density
r_s	scale radius
$R_\mathrm{t}, r_\mathrm{t}$	tidal radius
$r_{x,y}$	Pearson correlation coefficient
SC	Steep Cusp
SDSS DR9	Sloan Digital Skye Survey Data Release 9
SG	Second Generation (stars)
Σ	surface density
σ_v	velocity dispersion
SN(e)	Supernova(e)
SSP	Single Stellar population
T_exp	gas expulsion time scale
T_dyn	dynamical time scale
T_cr	crossing time
τ	ratio of the gas expulsion time scale to crossing time, i.e. $\tau \equiv T_\mathrm{exp}/T_\mathrm{cr}$
$\mathrm{T_{dis}}$	disruption time
$\mathrm{T_{diss}}$	dissolution time
T_r	radial period
T_ψ	azimuthal period
V_c	circular velocity
V_∞	asymptotic velocity of the galaxy rotation curve
V_G	velocity of the object with respect to the host galaxy
WC	Weak Cusp
$\xi(m)$	mass function

<div align="right">

1

</div>

Introduction

This chapter gives an overview of star clusters and underlines their significance in astrophysics. I also outline some of the important topics and open questions in star cluster research that still await a comprehensive answer. A more detailed background about each of the introduced topics is given in the following chapters of the thesis.

1.1 Star clusters

Star clusters, systems of self-gravitating stars containing $\sim 10^2$ to 10^7 stars. They show a large variation in their physical parameters like size, mass, chemical abundance of different elements (metallicity), etc., but in the Milky Way they can be broadly categorized into two groups: open clusters (OCs) and globular clusters (GCs), where the latter ones are older, more massive and metal-poor. Table 1.1 compares the basic properties of OCs and GCs in the Milky Way.

1.1.1 Significance of studying star clusters

There are several reasons why star clusters are important in astrophysics. First, star clusters are believed to be fundamental building blocks of galaxies (Kroupa, 2005; Assmann et al., 2011). It is a widely accepted notion that almost all stars do not form in isolation but in massive star clusters and then scatter into the galaxy. This is supported by the observed distribution of O-type stars (Parker & Goodwin, 2007) which are mostly located in young clusters or associations, or studies such as Baumgardt et al. (2008) who showed that assuming a power-law initial mass function (IMF) for gas embedded star clusters in the Milky Way, all halo field stars could originate from

Table 1.1: A comparison between the parameters of the Galactic OCs and GCs. This table is reproduced from Binney & Tremaine (2011). The data of GCs and OCs are taken from Harris (1996) and Piskunov et al. (2007).

Parameter	GCs	OCs
central density	$8 \times 10^3 \, \mathrm{M_\odot \, pc^{-3}}$	$10 \, \mathrm{M_\odot \, pc^{-3}}$
half-mass radius	$3 \, \mathrm{pc}$	$2 \, \mathrm{pc}$
tidal radius	$35 \, \mathrm{pc}$	$10 \, \mathrm{pc}$
central velocity dispersion	$6 \, \mathrm{km \, s^{-1}}$	$0.3 \, \mathrm{km \, s^{-1}}$
mass-to-light ratio	$2 \, \mathrm{M_\odot \, L_\odot^{-1}}$	$1 \, \mathrm{M_\odot \, L_\odot^{-1}}$
mass	$2 \times 10^5 \, \mathrm{M_\odot}$	$300 \, \mathrm{M_\odot}$
age	$10 \, \mathrm{Gyr}$	$300 \, \mathrm{Myr}$
population	II (metal-poor)	I (metal-rich)

dissolved star clusters either due to residual gas expulsion or dynamical evolution. Star clusters play an important role in the formation of galaxies (Searle & Zinn, 1978; Ashman & Zepf, 1992; Brodie & Strader, 2006) and the chemical enrichment/evolution of galaxies. Many astrophysical parameters of galaxies, such as the integrated galactic IMF have a strong correlation with those of star clusters (Kroupa & Weidner, 2003). Star clusters provide us with rich samples of stars with known distance, luminosity and metallicity using which we can infer the mass function and study star formation and evolution. Their age and richness allows us to constrain astrophysical and cosmological theories which are not directly related to them, e.g. constraints on the age of the universe (Krauss & Chaboyer, 2003). Moreover, they can be used as a proxy for the tidal field and the density profile of their host galaxy (e.g. Cole et al. 2012; Hasani Zonoozi et al. 2016). Star clusters can also be the environment in which intermediate-mass black holes form (e.g. Portegies Zwart et al. 2006; Giersz et al. 2015). All these aspects make star clusters one of the most intriguing objects in astrophysics.

1.1.2   The role of computer simulations

Star clusters are complex stellar systems and their study requires knowledge from different areas of physics, mathematics and computational science. To study clusters comprehensively, one needs to consider many details such as the dynamics of the gas out of which the cluster formed, stellar evolution, the dynamics of binary (or higher order) systems within the cluster, the effect of external fields (e.g. giant molecular clouds and galactic tidal fields). In addition, star clusters have gone through major dynamical evolution since their formation, except for very young star clusters. As

a result their current observed properties, such as the density profile of stars or the mass function, differ from the initial conditions under which they have formed. Due to such a high degree of complexity one can not only rely on an approach which is purely theoretical or observational, as these methods are unable and extremely inefficient to answer fundamental questions about clusters. To overcome this issue and bridge the gap between the current properties of star clusters and their initial conditions, computer simulations are now widely used in this field of research.

Over the years a number of techniques, computer software and hardware have been developed to address the formation and the evolution of stellar systems. At the core of most of these developments is "dealing with the N-body problem", i.e. determining the position ($\vec{r}$) and the velocity ($\vec{v}$) of N particles in a self-gravitating system at all future times using the initial conditions of particles ($\vec{r_0}, \vec{v_0}$). Holmberg (1941) studied the mutual tidal disturbance of two interacting stellar systems passing each other at a very small distance. They had 37 particles (mass elements) in each system and integrated their orbits numerically. To calculate the total force exerted on each particle, they took advantage of the fact that both the gravitational force and the intensity of light obey the inverse-square law. In particular, the particles in their study were represented by light-bulbs whose candle power was proportional to the mass of each particle. The total intensity of light at each point (proportional to the total gravitational force at that point) was then measured using photocells. von Hoerner (1960) did the first computer calculations for $N = 16$ particles. Later on, Aarseth (1963) performed the numerical calculation of the orbit of a hundred-body system on a computer.

It was soon realized that the formation of binaries and higher-order systems as well as a description for stellar evolution in the numerical calculations are highly important and one needs to take them into account to obtain a realistic picture of the evolution of stellar systems. Moreover, the need for a reliable and a high-accuracy integration scheme which was specifically tuned for N-body calculations, led to the development of a family of codes named NBODY1 to NBODY6 (Aarseth, 2000, 2003). In parallel to the improvements in computer codes, the development of a special-purpose computer named GRAPE (Gravity Pipe; Ito et al. 1990; Ebisuzaki et al. 1993; Makino et al. 2003), as well as general-purpose high performance computation devices such as graphics processing units (GPUs) paved the way for astrophysicists to perform collisional simulations of clusters with $N > 10^4$ particles.

NBODY6 is a collisional code which has been accelerated using GPUs (Nitadori & Aarseth, 2012) and is widely used in the community. It includes the dynamical formation of higher order

systems (binaries, triples, quadruples, etc.), stellar evolution of single and binary stars (and their collision) as well as a 3D external tidal field. The NBODY code family has revolutionized our understanding about clusters. In particular it has let us perform direct N-body simulations of real clusters with the same number of particles, e.g. M67 performed by Hurley et al. (2005) using NBODY4 or Palomar 4 and 14 done by Zonoozi et al. (2011, 2014) using NBODY6. Moreover, one can name the work of Baumgardt (2001) and Baumgardt & Makino (2003) who utilized the NBODY4 code on the GRAPE6 special-purpose computer and showed that the lifetimes of star clusters are significantly lower than what was believed before based on the Chandrasekhar's theory of stellar encounters and escape rate from star clusters (Chandrasekhar, 1942). An extension of NBODY6 is NBODY6TT (Renaud et al., 2011; Renaud & Gieles, 2013, 2015) which has enabled us to include a realistic time-dependent galactic tidal field in the simulations and study the early evolution phase of star clusters in interacting/merging galaxies such as Antennae galaxies. NBODY6++GPU is another extension which has been tuned to run on supercomputers by utilizing hybrid parallelization methods (MPI, GPU, OpenMP, and AVX/SSE). NBODY6++GPU has let us simulate GCs with $N = 10^6$ with primordial binaries (see the DRAGON project; Wang et al. 2016). This is considered as a breakthrough in collisional N-body simulations.

In addition to N-body simulations, Monte Carlo (MC) codes based on solving the Fokker-Planck equation (e.g. Cohn 1979) have been also developed to study star clusters. Examples of such codes include the cluster evolution code (CMC; Hénon 1971; Joshi 2000; Pattabiraman et al. 2013) and the Monte Carlo cluster simulator (MOCCA; Giersz et al. 2008, 2013, 2015). MC codes have been shown to follow the outcome of N-body simulations closely, albeit they need to be calibrated using N-body simulations first. Since MC codes such as MOCCA are faster compared to N-body codes, one can for example run simulations with a large fraction of primordial binaries (see e.g. Giersz et al. 2014), whose evolution is computationally expensive. Moreover, they allow us to make a large grid of runs and study a large parameter space for star clusters.

1.2 Challenges ahead

In spite of many years of research on the formation and evolution of star clusters, there are still many unanswered questions and challenges which still exist and need to be addressed. The focus of this thesis is on two of these challenges which are explained in greater detail in the following sections.

1.2.1 IMF and the binary fraction

The IMF is a vital tool with which stellar formation and evolution theories can be put to a test. The question if and how the IMF depends on the environment has crucial consequences for star formation theories as well as the dynamical evolution of stellar systems and their survival rate (Kouwenhoven et al., 2014). Although numerous studies have been conducted on the mass-function of field stars, OB associations, OCs and GCs (e.g. Massey et al. 1995; Kroupa 2001; Chabrier 2003; Marks et al. 2012), the exact mathematical form of the IMF (e.g. power-law vs. log-normal) is still a matter of debate, since deriving the IMF is not trivial for a number of reasons. What we can measure for star clusters is in fact the present-day mass function (PDMF) and not the IMF. Except for very young star clusters (i.e. $T < 1\,\mathrm{Myr}$), the PDMF of star clusters is different from their IMF as the cluster loses mass due to both stellar evolution (mainly at the high-mass end) and dynamical evolution (mainly at the low-mass end) and this mass-loss needs to be accounted for if one wants to infer the IMF from the PDMF. The mass-loss strongly depends on the initial conditions of star clusters such as the mass and size of the star cluster as well as the strength of the tidal field (Baumgardt & Makino, 2003) and even the IMF itself. In other words, to determine the IMF properly, stellar evolution and dynamical evolution both need to be considered and cannot be decoupled.

Moreover, in the process of obtaining the PDMF, one will encounter several difficulties. First, one needs to distinguish between genuine members of star clusters and background stars. This is especially important for the low-mass end of the IMF where stars are harder to observe and photometric errors are larger. A commonly employed technique is to determine the possible members of a star cluster based on the distribution of their proper motions in the velocity space (also known as the vector diagram) as well as comparing their positions in a colour magnitude diagram (CMD) with standard evolutionary tracks and isochrones. Second, since star clusters have a considerable population of binary systems of order $\sim 5 - 50\,\mathrm{per\,cent}$ (Davis et al., 2008; Ji & Bregman, 2013; Sollima et al., 2007) for GCs and $\sim 30 - 60\,\mathrm{per\,cent}$ for open clusters (Fan et al., 1996; Sana et al., 2009, 2011), one has to correct the PDMF for the effect of unresolved binaries or higher order systems. In unresolved binaries, faint (low-mass) stars cannot be detected and the overall measured luminosity of the system will be mistakenly attributed to the brighter companion only. This leads to a faulty estimation of the stellar masses as well as underestimating the number of low-mass stars. Third, to fit a mathematical function to the empirical distribution of stellar masses, great care needs to be exercised. For example, the least-squares methods which

are frequently used are biased and in a case of a power-law mass function, the estimated power-law index can be off by 1.0 (when the true index is 2.5; Clauset et al. 2007). In this case more sophisticated methods such as maximum likelihood estimation, which are bias free, must be used.

In addition to the effect that binaries have on the observed mass function, they can also affect other measured properties of clusters or their evolution. For example, the dynamical mass or the virial ratio[1] of a star cluster which is determined by measuring the radial velocity dispersion can be overestimated due to the effect that unresolved binaries have on the perceived radial motion of stars in star clusters. Kouwenhoven & de Grijs (2008, 2009) showed that the factor by which the dynamical mass can be overestimated due to unresolved binaries vary from 0.1 for clusters with intermediate densities ($n = 0.1 - 10^7 \, \mathrm{pc}^{-3}$) to 10 for sparse clusters ($n \sim 0.1 \, \mathrm{pc}^{-3}$). As a result, devising a method to systematically determine the true binary fraction of a star cluster and correcting the effect of unresolved binaries on the IMF is of vital importance.

There are several direct methods with which one can detect the binaries, such as the direct observation of both components (visual binaries), the detection of the change in position of the primary component in the sky due to the gravitational pull of an unseen companion (astrometric binaries), detecting the periodic changes in the light curve of a star (eclipsing binaries[2]), detection of periodic motions of absorption lines in the observed spectra of a star or both stars (single and double-line spectroscopic binaries). These methods, however, require many hours of direct observation of a carefully selected sample of stars. Unresolved binaries leave a fingerprint in the CMD, i.e. for equal-mass binaries they form a second sequence of stars which is $\sim 0.75 \, \mathrm{mag}$ above the main-sequence of single stars and for smaller mass-ratios the second sequence will blend in with the single-star sequence (Hurley & Tout, 1998). This (the second sequence of stars in the CMD), instead of direct observation of binaries, can be used to estimate the binary fraction.

1.2.2   Multiple stellar populations (MSPs) in GCs

Observational evidence

It is generally assumed that all stars in star clusters are born in close proximity to each other, and in well-mixed molecular clouds by a rapid star formation process and therefore have similar ages and metallicities (Lada & Lada, 2003). As a result, star clusters should only host a single

---

[1]The ratio of the total kinetic to the potential energy of the cluster
[2]Other phenomena such as star spots or stellar oscillations can also be the cause of such changes in the observed light curve of a star but they have different patterns which distinguishes them from eclipsing binaries

population of stars, i.e. they are bona fide single stellar population systems. However, recent observations of GCs show a statistically significant star-to-star variation in the abundance of light elements, such as Na, O, Mg or Al (e.g., Minniti et al. 1996; Carretta et al. 2009, 2010; Marino et al. 2011; Gratton et al. 2013). These abundance anomalies of light elements are not associated with any spread in the iron abundance for the majority of GCs except for a few cases such as ω Cen (Gratton et al., 2004). Such massive GCs are thought to be different than normal GCs and have a different origin, for example being the remnant of a disrupted dwarf galaxy (Meza et al., 2005; Pfeffer et al., 2014). Moreover, these peculiarities in the abundance patterns distinguishes chemically peculiar stars from other stars in the cluster as well as field stars.

In addition to the abundance anomalies mentioned above, the CMD of some GCs split into two or more evolutionary sequences (e.g., ω Cen Rey et al. 2004 and Bedin et al. 2004; NGC 2808 D'Antona & Caloi 2004, Piotto et al. 2007 and Milone et al. 2012c; NGC 1851 Milone et al. 2008; 47 Tuc Milone et al. 2012a; NGC 6397 Milone et al. 2012b; M22 Marino et al. 2012; GCs in Fornax D'Antona et al. 2013).

These findings are indicative of self-enrichment in GCs and suggest that star clusters are comprised of at least two stellar populations, in direct contradiction to the conventional star formation scenario described earlier. We refer to these two populations as first-generation (FG) and second-generation (SG) stars for convenience and to be consistent with previous studies such as Decressin et al. (2008). In our terminology FG and SG stars correspond to stars with normal (or primordial) and enriched chemical compositions respectively.

The observations show that the number ratio of SG to FG stars, N_2/N_1, is around unity although with some spread (D'Antona & Caloi, 2008; Bastian & Lardo, 2015). Further studies on MSPs have shown that they exhibit different spatial (ω Cen Bellini et al. 2009; several GCs Lardo et al. 2011; 47 Tuc Nataf et al. 2011; M15 Larsen et al. 2015) and dynamical distributions (47 Tuc Richer et al. 2013 and Kučinskas et al. 2014). However, Dalessandro et al. (2014) found that the different populations in NGC 6362 share the same radial distribution which is the first evidence of fully spatially mixed MSPs ever observed in a GC.

All old Galactic GCs which have been surveyed to date in detail have been shown to host MSPs with the exception of Ruprecht 106 (Villanova et al., 2013). It is believed that all old clusters with a present-day mass larger than $\sim 4 \times 10^4 \, M_\odot$ show an anti-correlation between the abundance of Na and that of O (Carretta et al., 2010). This mass limit includes almost all of the Galactic GCs. As a result, the Na-O anti-correlation (i.e. star-to-star variation of Na and O), which signals the

existence of MSPs seems to be an intrinsic property of all GCs and as suggested by Carretta et al. (2010) can be considered as the definition of a GC. In other words bona fide GCs are those which exhibit the Na-O anti-correlation. This definition of GCs separates them from OCs (younger and less massive star clusters) which do not show any sign of the Na-O anti-correlation (Pancino et al., 2010; Carretta et al., 2010; Bragaglia et al., 2013, 2014) and therefore are comprised of only a single population of stars.

Formation scenarios of MSPs

Several scenarios have been proposed to address the origin of multiple stellar generations in GCs (Decressin et al. 2007a,b; de Mink et al. 2009; Renzini 2008; D'Ercole et al. 2010; Conroy & Spergel 2011; Ventura et al. 2001; Valcarce & Catelan 2011 and Bastian et al. 2013, Denissenkov & Hartwick 2014) among which the four main scenarios are: (1) fast rotating massive stars (FRMS) $(20 - 120\,M_\odot$; Prantzos & Charbonnel 2006; Maeder & Meynet 2006; Decressin et al. 2007a,b); (2) asymptotic giant branch (AGB) stars $(4 - 9\,M_\odot$; Ventura et al. 2001; D'Ercole et al. 2008, 2010; Ventura & D'Antona 2011); (3) massive $(10 - 100\,M_\odot)$ and intermediate mass $(4 - 10\,M_\odot)$ binaries (de Mink et al., 2009) and (4) early disc accretion in low-mass pre-main-sequence stars (enriched gas comes from stars with $M > 10\,M_\odot$)(Bastian et al., 2013).

In the FRMS scenario, stars that spin at a rate close to their critical break-up speed can lose extensive amounts of mass via stellar winds which are slow enough to be retained in the gravitational potential well of the cluster and form circumstellar discs out of which SG stars will be born. In the AGB and massive binary scenarios, these slow winds come from the envelopes of evolving intermediate-mass stars in their AGB phase and numerous massive interacting binaries in the core of clusters respectively. SG stars in the FRMS scenario need to form on a very short time-scale, $t < 8.8\,Myr$ (Krause et al., 2013), before the burst of the first supernova (SN), since SN winds can destroy circumstellar discs formed around fast-rotating FG stars and interrupt the star formation (Decressin et al., 2007a). In the AGB scenario, on the other hand, the formation of SG stars is triggered after all SNe have gone off and the cluster has been cleared of SN II ejecta $(t > 28\,Myr)$ (D'Ercole et al., 2008), otherwise AGB ejecta will be polluted by SN ejecta which will cause the iron abundance of SG stars to differ from that of FG stars, in contradiction with observations. Bastian et al. (2013) proposed a model in which GCs do not need to go through different instances of star formation to produce chemically peculiar stars. According to this model, interacting massive binaries $(M > 10\,M_\odot)$ supply the intra-cluster medium with

enriched material which will be accreted by low-mass stars ($M < 2\,\mathrm{M_\odot}$) while they are still in their pre-main-sequence phase. The main difference between this model and other models is that stars with different chemical abundances belong to the same generation of stars. The main caveat of this model is that the circumstellar discs around accreting low-mass stars need to survive for 5 to 10 Myr which is a questionable assumption in GCs with a denser core (Bastian et al., 2013). In addition, it cannot explain why there are two distinct sequences in the CMD instead of a continuous spread.

In a recent study, Bastian et al. (2015) tested the yields of all the proposed models in the literature for their consistency with observations and showed that all the proposed models over-produce He for a given change in Na and O. Hence none of the scenarios which has been put forth so far is able to explain all the observed GCs.

In addition to this discrepancy between the theoretical yields and observations, the ejecta in the FRMS and AGB scenarios are not enough to form a large population of SG stars and explain the roughly equal number of FG and SG stars found in observations (D'Antona & Caloi, 2008; Bastian & Lardo, 2015). Assuming a canonical Kroupa (2001) IMF, the total mass which is lost by all FRMS and AGB stars, constitutes between $\sim 4\%$ to 9% of the initial mass of all FG stars (de Mink et al., 2009). If we assume that the gas which is lost by this mechanism entirely turns into SG stars, i.e. star formation efficiency is 100%, the number ratio of SG stars to FG stars is expected to be at most $\sim 10\%$. This issue, which is referred to as the mass-budget problem, does not exist for the massive and intermediate-mass binaries as they provide more ejecta than AGB and fast-rotating massive stars combined. In addition their ejecta are further mixed with an approximately equal amount of pristine gas which doubles the mass of the available gas for star formation. As a result there is a substantial amount of polluted gas to form a large number of SG stars (de Mink et al., 2009).

To address the mass-budget problem two solutions have been proposed: either a cluster must have been at least 10-20 times more massive and have undergone significant mass-loss ($\sim 90\%$) or the cluster IMF must have been strongly top-heavy, i.e. it initially had many more massive stars than predicted by a canonical IMF. There is observational evidence against both of these solutions. First, observations of GCs in a number of dwarf galaxies, such as the Fornax dwarf spheroidal (dSph) galaxy, show a high ratio of metal-poor GCs to field stars which cannot be explained if star clusters were initially 10 times more massive and underwent significant mass-loss (Larsen et al., 2012, 2014a). Second, Dabringhausen et al. (2009) found that a top-heavy IMF will

lead to high mass-to-light (M/L) ratios in old stellar systems ($T = 12$ Gyr) such as ultra compact dwarf galaxies (UCDs) and GCs.

As a result the origin of abundance anomalies in GCs is still a matter of debate. In addition, there is little known about the initial conditions of GCs with MSPs (e.g. mass and radius) according to different scenarios or the role of mechanisms such as gas expulsion in their formation and evolution. More specifically, the following questions, which still await a comprehensive answer, will determine which of the proposed scenarios for the origin of MSPs is correct.

- What are the required initial conditions that such a significant mass-loss is a universal process happening to every cluster almost independently of its mass, size, location in the galaxy, etc.?

- What are the required conditions under which the final number ratio of SG to FG stars as well as the M/L ratios of GCs with MSPs match the observations?

- What is the time-scale over which the clusters lose 90% of their mass?

1.3   Aims and thesis outline

Given the importance of star clusters and the aforementioned challenges and open questions in this field, the aims of the thesis are twofold: (1) devising a method to determine the mass function considering the effect of unresolved binaries and testing it on a real cluster; (2) constraining the formation scenarios of MSPs and deriving the initial conditions of GCs with MSPs. To reach the aforementioned aims, I make use of N-body and MC simulations.

The present thesis is based on three publications and has been structured as follows. In Chapter 2 which entails Paper I (Khalaj & Baumgardt, 2013), I introduce a novel method to obtain the mass function and the true binary fraction of a star cluster and correct the mass function for the effect of unresolved binaries. I test my method on Praesepe which is a young OC. To do so, I determine the possible cluster members of Praesepe on the basis of their proper motion as well as their position in the CMD.

In Chapter 3 I study the solutions to the mass-budget problem, i.e. top-heavy IMF and significant mass-loss, in GCs with MSPs and I derive the range of mass-loss levels and the high-mass index of the IMF which are in agreement with the observed fraction of SG stars and M/L ratios of Galactic GCs. I also discuss the role of dynamical evolution and helium-enhancement on

my results.

Chapters 4 and 5, which are respectively comprised of Paper II and III (Khalaj & Baumgardt, 2015, 2016), examine the viability of the significant mass-loss scenario in Galactic and Fornax GCs according to the AGB and FRMS scenario. In Chapter 4 I first discuss the possible mass-loss mechanisms in GCs. I then make a large grid of N-body simulations in order to investigate if mass-loss as a result of primordial gas expulsion can be responsible for the large fraction of SG stars in GCs with MSPs. I setup clusters with two stellar populations in which 10 per cent of all stars are SG stars. I simulate clusters with different initial masses, different ratios of the half-mass radius of first to SG stars, different primordial gas fractions and Galactic tidal fields with varying strength. I then let my clusters undergo primordial gas loss and obtain their final properties such as mass, half-mass radius and the fraction of SG stars. Using my N-body grid I then perform an MC analysis to constrain the initial masses, radii and required gas expulsion time-scales of GCs with MSPs. In Chapter 5, I study the problem of the large fraction of metal-poor GCs to field stars in the Fornax dSph and provide a solution to reconcile it with the significant mass-loss scenario. I use a series of numerical simulations (i.e. numerical galactic orbit integration) to determine the limit of mass-loss from the Fornax dSph as a function of the initial orbital radii of its GCs and the speed with which stars leave Fornax GCs. I consider a set of cored and cuspy density profiles for Fornax and specify the attained mass-loss by both the AGB and the FRMS scenario.

Finally, in Chapter 6, I summarize the main outcomes of this study and the implications of the results.

2

The stellar mass function, binary content and radial structure of the open cluster Praesepe

Khalaj P., Baumgardt H., 2013, MNRAS, 434, 3236

In this chapter[1] we study Praesepe as an example of a nearby young Galactic OC. In particular, we determine Praesepe members based on the Positions and Proper Motions Extended Large (PPMXL) catalogue (Roeser et al., 2010) and the Sloan Digital Skye Survey Data (SDSS) Data Release 9 (DR9) and derive its stellar mass function and binary fraction using a novel approach.

The chapter is structured as follows. We first review the previous studies conducted on Praesepe in Section 2.1. We then discuss the observational data in Section 2.2. In Section 2.3 we describe the procedures we have followed to determine possible members. Our results regarding the mass function and binary fraction of Praesepe are presented in Section 2.4 and Section 2.5. We finally summarize the main results in Section 2.6.

2.1 Previous studies

With a distance modulus of $(m - M)_0 = 6.30 \pm 0.07$ mag (van Leeuwen, 2009) ($d = 181.97^{+5.96}_{-5.77}$ pc) Praesepe is one of the nearest clusters to the Sun. Due to its proximity, Praesepe has been studied extensively in the past. However, so far no consensus on the stellar distribution and low-mass mass function has been reached. Proper motion studies of the bright members were first carried out by Klein Wassink (1927), Jones & Cudworth (1983) and Jones & Stauffer (1991), who

---

[1]This chapter is based on Khalaj & Baumgardt (2013) and the published version is available at http://dx.doi.org/10.1093/mnras/stt1239

determined members down to $V \sim 18\,\mathrm{mag}$, corresponding to masses of about $0.3\,\mathrm{M_\odot}$. Hambly et al. (1995) presented cluster members down to $0.1\,\mathrm{M_\odot}$ in the central $19\,\mathrm{deg^2}$ using images taken by the United Kingdom Schmidt Telescope. They found evidence for mass segregation in Praesepe and a rising mass function from $1\,\mathrm{M_\odot}$ down to $0.1\,\mathrm{M_\odot}$, the limit of their survey. Pinfield et al. (1997) conducted a photometric survey of Praesepe in RIZ-bands down to $I = 21.5\,\mathrm{mag}$ using the Isaac Newton Telescope (INT). They also found a rising mass function $(\xi(m) \sim \mathrm{d}N/\mathrm{d}m \sim m^{-\alpha})$ from $0.15\,\mathrm{M_\odot}$ down to $0.07\,\mathrm{M_\odot}$ with slope $\alpha \geq 1.5$. In contrast, using proper motions derived from the Two Micron All Sky Survey (2MASS) and the Palomar Observatory Sky Survey, Adams et al. (2002) found that the low-mass stellar mass function below $0.4\,\mathrm{M_\odot}$ can be fitted by a flat mass function with $\alpha \approx 0$ and only a marginal radial dependence of the mass function. Chappelle et al. (2005) probed the central $2.6\,\mathrm{deg^2}$ of Praesepe using I-band data down to $I \sim 21.3\,\mathrm{mag}$ and Z-band data down to $Z \sim 20.5\,\mathrm{mag}$, from images taken by the INT/Wide Field Camera (WFC) and near-infrared follow-up measurements using the United Kingdom Infrared Telescope (UKIRT) Fast Track Imager. They found a rising mass function from $1\,\mathrm{M_\odot}$ down to $0.1\,\mathrm{M_\odot}$. González-García et al. (2006) conducted deep photometric searches for sub-stellar members of Praesepe using the Sloan i' and z' broad-band filters, with the 3.5-meter and the 5-meter Hale telescopes on the Calar Alto and Palomar Observatories. The total area that they surveyed was $1177\,\mathrm{arcmin^2}$ and the 5σ detection limit of their survey was $i' = 24.5\,\mathrm{mag}$ and $z' = 24\,\mathrm{mag}$ which corresponds to $m = 50 - 55\,\mathrm{M_{Jup}}$. They found that the mass function of Praesepe strongly depends on the adopted cluster age and at the youngest possible ages of Praesepe $(500 - 700\,\mathrm{Myr})$, their analysis suggests a rapidly decreasing mass function for brown dwarfs. Kraus & Hillenbrand (2007) combined archival survey data from SDSS, 2MASS, United States Naval Observatory (USNO) Catalogue B1.0 (USNO-B1.0) and USNO CCD[2] Astrograph Catalogue 2.0 and found 1010 stars in Praesepe as candidate members with probability $p > 80\,\mathrm{per\,cent}$. Their result for the mass function of Praesepe is similar to that of Hambly et al. (1995), i.e a rise from $1\,\mathrm{M_\odot}$ down to $0.1\,\mathrm{M_\odot}$. Boudreault et al. (2010) performed an optical (I_c-band) and near-infrared (J and K_s-band) photometric survey of the innermost $3.1\,\mathrm{deg^2}$ of Praesepe with 5σ detection limits of $I_c = 23.4\,\mathrm{mag}$ and $J = 20.0\,\mathrm{mag}$. They observed that the mass function of Praesepe rises from $0.6\,\mathrm{M_\odot}$ down to $0.1\,\mathrm{M_\odot}$ with $\alpha = 1.8 \pm 0.1$ and turns over at $\sim 0.1\,\mathrm{M_\odot}$. Baker et al. (2010) found a moderately rising mass function with $\alpha = 1.11 \pm 0.37$ for the mass range $0.6\,\mathrm{M_\odot}$ to $0.125\,\mathrm{M_\odot}$ in the UKIRT Infrared Deep Sky Survey Galactic Clusters Survey (UKIDSS GCS) for $Z < 18\,\mathrm{mag}$. Using observations

---

[2]Charged-coupled device

from the Large Binocular Telescope in the $rizY$ bands, Wang et al. (2011) identified 62 cluster member candidates (40 of which are sub-stellar) within the central $0.59\,\mathrm{deg}^2$ of Praesepe down to a 5σ detection limit of $i \sim 25.6\,\mathrm{mag}$ ($\sim 40\,\mathrm{M_{Jup}}$). They found that the mass function of Praesepe shows a rise from $105\,\mathrm{M_{Jup}}$ to $60\,\mathrm{M_{Jup}}$ and then a turnover at $\sim 60\,\mathrm{M_{Jup}}$. More recently, Boudreault et al. (2012) found 1116 cluster candidates in a $\sim 36\,\mathrm{deg}^2$ field based on a 3σ astrometric and five-band ($ZYJHK$) photometric selection, using the DR9 of UKIDSS GCS. They found that the mass function of Praesepe has a maximum at $\sim 0.6\,\mathrm{M_\odot}$ and then decreases to the lowest mass bin of $0.056\,\mathrm{M_\odot}$.

For a summary of the mass ranges covered and mass function slopes derived in various previous studies of Praesepe as well as a comparison with the mass function that we have derived for Praesepe, refer to Section 2.4.3 (Table 2.4).

2.2   Observational data

In this study we combine data from the PPMXL catalogue (Roeser et al., 2010) with z magnitudes from SDSS DR9 (Ahn et al., 2012). PPMXL catalogue combines the USNO-B1.0 (Monet et al., 2003) and 2MASS catalogues (Skrutskie et al., 2006) yielding the largest collection of proper motions in the International Celestial Reference Frame (ICRS) to date (Roeser et al., 2010). USNO-B1.0 contains the positions of more than one billion objects taken photographically around 1960; 2MASS is an all-sky survey conducted in the years 1997 to 2001 in the J, H and K_s bands. In PPMXL, data from USNO-B1.0 are used as the first epoch images and those from 2MASS as the second epoch images, deriving the mean positions and proper motions for 910,468,710 objects from the brightest magnitudes down to $V \approx 20\,\mathrm{mag}$ (Roeser et al., 2010). Mean errors of the proper motions vary from ~ 4 milliarcseconds per year ($\mathrm{mas\,yr^{-1}}$) for $J < 10\,\mathrm{mag}$ to more than $10\ \mathrm{mas\,yr^{-1}}$ at $J > 16\,\mathrm{mag}$.

The field of Praesepe is also covered in the SDSS DR9. A cross-matching between SDSS and PPMXL shows that SDSS is ~ 95 per cent complete within $5\,\mathrm{deg}$ from the centre of Praesepe for stars with $J \leq 15.5\,\mathrm{mag}$ but does not contain stars beyond $5\overset{\circ}{.}5$ from the centre of Praesepe. SDSS data covers five optical bands ($ugriz$) to a depth of $g \sim 23\,\mathrm{mag}$ (York et al., 2000).

Table 2.1: Praesepe parameters. (α_0, δ_0): cluster centre (see Section 2.3.3) ; (μ_α, μ_δ): mean proper motion of the cluster; (e_α, e_δ): proper motion mean error; σ_v: 1D velocity dispersion

Parameter	Value	Reference
α_0	$08^h 39^m 37^s$	Our work
δ_0	$+19°35'02''$	
$(m - M)_0$	$6.30 \pm 0.07\,\mathrm{mag}$	van Leeuwen (2009)
μ_α	$-35.81\,\mathrm{mas\,yr^{-1}}$	
e_α	$0.29\,\mathrm{mas\,yr^{-1}}$	
μ_δ	$-12.85\,\mathrm{mas\,yr^{-1}}$	
e_δ	$0.24\,\mathrm{mas\,yr^{-1}}$	
σ_v	$0.67 \pm 0.23\,\mathrm{km\,s^{-1}}$	Madsen et al. (2002)
$\log{(\mathrm{age})}$	$8.77 \pm 0.1\,\mathrm{dex}$	Fossati et al. (2008)
$E(B - V)$	$0.027 \pm 0.004\,\mathrm{mag}$	Taylor (2006)
[Fe/H]	$0.11 \pm 0.03\,\mathrm{dex}$	An et al. (2007)

2.3 Membership determination

2.3.1 Astrometric membership

We restrict our study to a radius of 3.5 degrees from the centre of Praesepe ($\alpha = 8^h 40^m 00^s$, $\delta = 19°30'00''$ Lynga 1995). The reason of this choice is that the tidal radius of Praesepe is $r_t = 3°.5 \pm 0°.1$ (Kraus & Hillenbrand, 2007) suggesting that stars beyond this point are more likely to be background stars. We present our estimation of the background contamination within this radius in Section 2.3.4.

Within the search area, cluster members are selected based on proper motions followed by two photometric tests, both of which are described in more detail further below. We restrict ourselves to stars with $J < 15.5\,\mathrm{mag}$ whose proper motion errors are about $\sim 4\,\mathrm{mas\,yr^{-1}}$. For fainter stars the proper motion errors become much larger than $10\,\mathrm{mas\,yr^{-1}}$. A comparison of PPMXL with Boudreault et al. (2012) shows that PPMXL is about 93 per cent complete down to $J = 15.5\,\mathrm{mag}$, but becomes incomplete for fainter magnitudes.

We first select cluster members based on their proper motions. We use a χ^2 test to separate cluster members from field stars, i.e. for each star i, we calculate a χ^2 value according to:

$$\chi_i^2 = \frac{(\mu_{\alpha i} - \bar{\mu}_\alpha)^2}{e_{\alpha i}^2 + e_\alpha^2 + \sigma_\alpha^2} + \frac{(\mu_{\delta i} - \bar{\mu}_\delta)^2}{e_{\delta i}^2 + e_\delta^2 + \sigma_\delta^2} < 6.17 \tag{2.1}$$

where $\mu_{\alpha i}$ and $\bar{\mu}_\alpha$ are the proper motion of star i and the average cluster proper motion in right
ascension, $\mu_{\delta i}$ and $\bar{\mu}_\delta$ are the proper motion of star i and the average cluster proper motion in
declination, $e_{\alpha i}$, e_α, $e_{\delta i}$, e_δ are the corresponding errors and σ_α and σ_δ are the components of
the internal velocity dispersion. For the mean cluster motion and the corresponding errors we
use $\bar{\mu}_\alpha = -35.81 \, \mathrm{mas \, yr^{-1}}$, $\bar{\mu}_\alpha = -12.85 \, \mathrm{mas \, yr^{-1}}$, $e_\alpha = 0.29 \, \mathrm{mas \, yr^{-1}}$ and $e_\delta = 0.24 \, \mathrm{mas \, yr^{-1}}$ as
determined by van Leeuwen (2009). We also assume a one-dimensional (1D) internal velocity
dispersion of $\sigma_v = 0.67 \pm 0.23 \, \mathrm{km \, s^{-1}}$ (Madsen et al., 2002), which corresponds to a proper motion
of $\sigma_v = 0.78 \, \mathrm{mas \, yr^{-1}}$ at the distance of Praesepe. As the threshold separating members from
non-members we assume $\chi^2 = 6.17$, equivalent to a 95.4 per cent (2σ) limit for two independent
degrees of freedom. Table 2.1 summarizes the parameters for Praesepe.

We ignore stars with very large proper motion errors ($e_\alpha > 15 \, \mathrm{mas \, yr^{-1}}$) in PPMXL since a
separation into field and cluster stars is not possible for them given the absolute value of the proper
motion of Praesepe (see also Figure 2.1). We ignore projection effects due to the different location
of stars on the sky since they amount to only $0.07 \, \mathrm{mas \, yr^{-1}}$ difference in proper motion, significantly
smaller than the error bars in PPMXL. We also ignore distance effects due to the different radial
distances of stars along the light of sight. This distance effect only adds an uncertainty of about
$2 \, \mathrm{mas \, yr^{-1}}$ which is small compared to the typical proper motion error of PPMXL, although it
could be important for bright stars.

Figure 2.1 shows the proper motions of all PPMXL stars in a field of $3\overset{\circ}{.}5$ in radius. Stars
that pass our kinematic test are shown in red. From 45870 stars with $J \leq 15.5 \, \mathrm{mag}$ and $e_\alpha, e_\delta \leq$
$10 \, \mathrm{mas \, yr^{-1}}$ that reside within $3\overset{\circ}{.}5$ from the cluster centre, 1613 stars meet our χ^2 criterion.

2.3.2   Photometric membership

We use the latest version of the PADOVA stellar evolution models[3] from Marigo et al. (2008) and
Girardi et al. (2010) to estimate the colours and magnitudes of the cluster members based on their
metallicity, age and extinction. We use the J and K_s bands of the PADOVA models to create an
isochrone. In addition to PADOVA isochrones, we also use two more isochrones from Hauschildt
et al. (1999) (NextGen models) and Allard et al. (2011) (BT-Settl models) for comparison. In our
study, we adopt an age of 590 Myr (Fossati et al., 2008), an extinction of $E(B - V) = 0.027 \, \mathrm{mag}$

---

[3] http://stev.oapd.inaf.it/cgi-bin/cmd
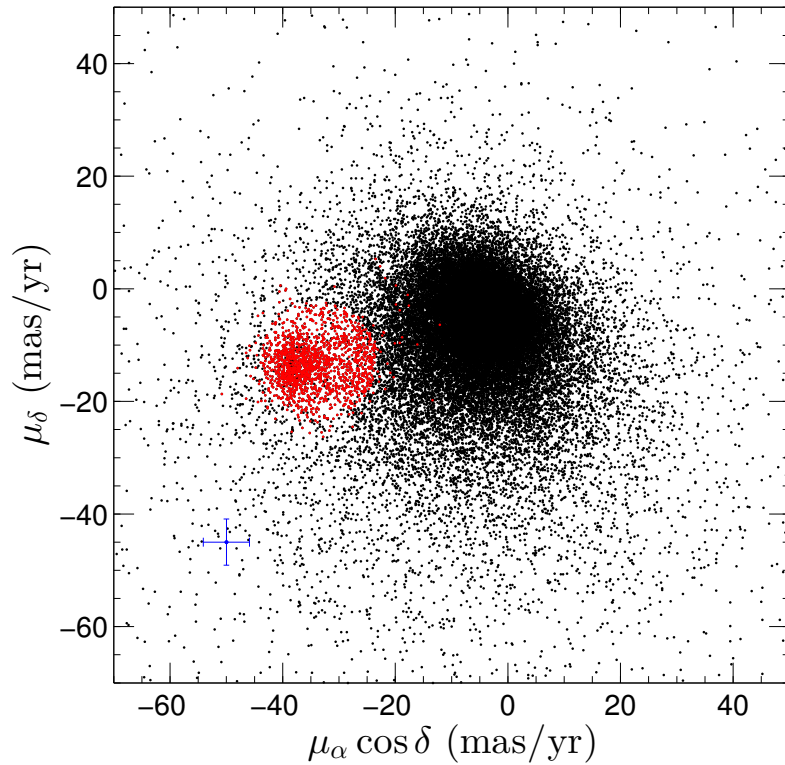
Figure 2.1: Plot of the proper motions of all PPMXL stars in a field of 3°.5 from the centre of Praesepe (black dots) and the stars that satisfy the proper motion test described by Eq. (2.1) (red dots). The mode of the proper motion errors is shown by the blue cross in the lower left corner.
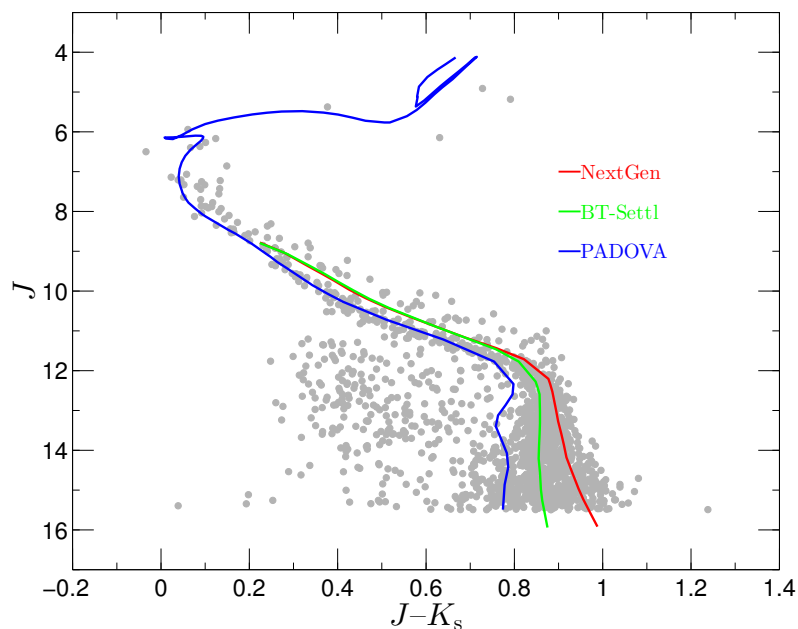
Figure 2.2: CMD of the stars selected by proper motions (filled grey circles). Solid blue, green and red lines show the PADOVA (left), BT-Settl (middle) and NextGen (right) isochrones respectively.
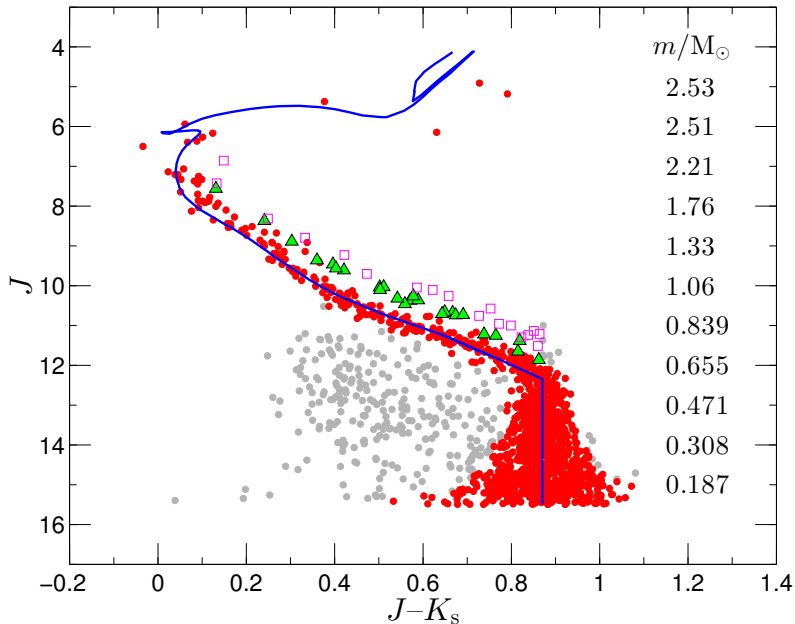
Figure 2.3: CMD of the stars selected by proper motion and photometry. Filled red circles show stars that satisfy both tests (1286 stars). The filled grey circles show stars that do not pass the photometric test. Inspection of the spatial position of these stars shows that they are evenly spread across the survey region and the distribution of their χ^2 values shows no clustering around zero, hence these stars are most likely field stars. The green-filled triangles show possible binaries (25 stars) and open magenta squares show possible multiples (18 stars). The blue line denotes the modified PADOVA isochrone.

(Taylor, 2006) and a distance modulus of $(m - M)_0 = 6.30 \pm 0.07$ mag (van Leeuwen, 2009) for Praesepe. A number of values have been found for the metallicity of Praesepe: $+0.13 \pm 0.007$ dex (Boesgaard & Budge, 1988); $+0.125 \pm 0.032$ dex (Boesgaard, 1989); [Fe/H] $= +0.038 \pm 0.039$ dex (Friel & Boesgaard, 1992); 0.11 ± 0.03 dex from spectroscopy and $+0.20 \pm 0.04$ dex from photometry (An et al., 2007) and $+0.27 \pm 0.10$ dex (Pace et al., 2008). Since the location of stars in the CMD is not very sensitive to the adopted metallicity, we only consider [Fe/H]$=0.11 \pm 0.03$ dex (An et al., 2007).

Figure 2.2 shows the distribution of the stars that pass the kinematic test in a CMD as well as the corresponding PADOVA (T=590 Myr, [Fe/H]=0.11 dex), NextGen and BT-Settl (both with T=590 Myr, [Fe/H]=0 dex) isochrones for comparison. We require that photometric members lie within 2.5σ of the isochrones in the J vs $J - K_s$ CMD where σ refers to the mean error of photometry for each star. It can be seen from Figure 2.2 that the proper motion selected stars agree reasonably well with the PADOVA isochrone down to $J = 11.75$ mag, which corresponds to about 0.7 M$_\odot$. However, starting from $J = 11.75$ mag, the PADOVA isochrone disagrees with
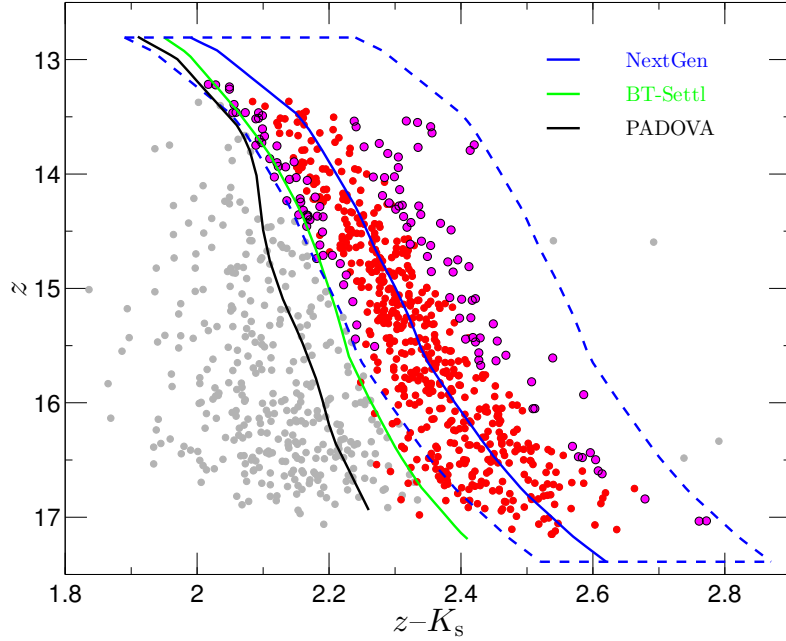
Figure 2.4: CMD of all stars with $J > 12\,\mathrm{mag}$ which are selected by the first photometric test (1020 stars). Filled red circles show stars lie within 2.5σ of the isochrone (528 stars). The filled magenta circles show those stars which are designated as candidate members due to their spatial position and χ^2 distribution of proper motions (124 stars). The filled grey circles show the stars that fail the second photometric test, hence they are assumed as non-members (368 stars). PADOVA (left), BT-Settl (middle) and NextGen (right) isochrones are represented by black, green and solid blue lines respectively.

the actual location of the possible Praesepe members in the CMD as the isochrone predicts faint (low-mass) stars to be bluer than observed. Since this disagreement is virtually insensitive to the assumed age, metallicity and distance modulus, we reason that this is due to the inherent limitations in the PADOVA isochrone for low-mass stars. Similar results have been obtained by Röser et al. (2011) for the Hyades. The focus of PADOVA isochrones in particular has been on the high-mass and evolved stars which produce the bulk of the luminosity of a cluster, whereas NextGen and BT-Settl isochrones aim to reproduce the evolutionary tracks of very low-mass stars (NextGen) even down to the planetary regime (BT-Settl). Low-mass stars (dwarfs) are cool enough to allow for the formation of molecules such as TiO and H_2O. The existence of molecules and dust in the atmosphere of a star affects opacity and changes the spectrum of a star significantly. The model atmospheres for cool stars are still debated and far from satisfactory. As a result, the uncertainties which are involved in the modeling of stellar atmospheres in different optical properties is the reason why the aforementioned isochrones differ in the low-mass range and they do not necessarily match the actual location of stars in the low-mass end.
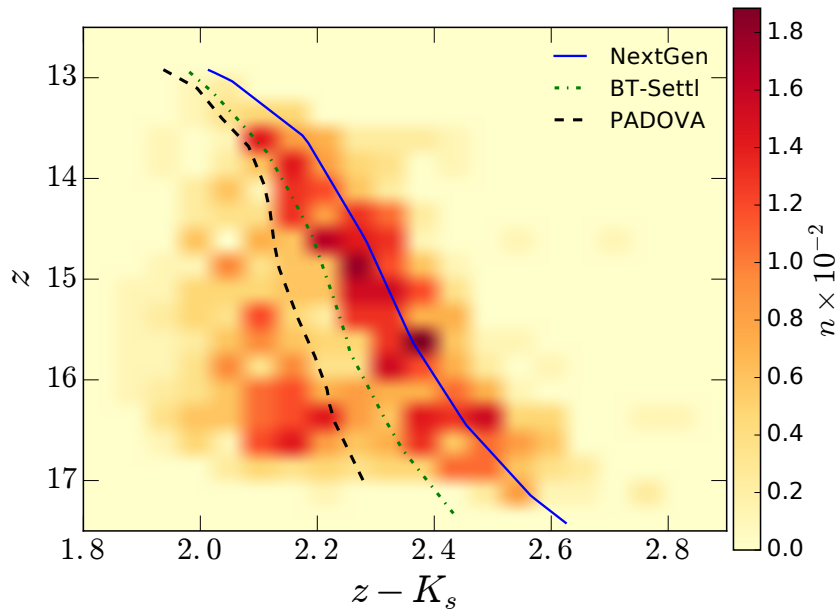
Figure 2.5: The normalized density of stars at different positions in the CMD (2D histogram). Stars shown in this figure are the same as Figure 2.4. Field stars and the possible cluster members which occupy two dense areas in the CMD (darker areas) are clearly separated from each other. The NextGen isochrone matches the actual location of possible members.

In order to select faint cluster members photometrically, we shift the PADOVA isochrone by $+0.1$ mag for magnitudes fainter than $J = 11.75$ mag. This seems better than using the BT-Settl or NextGen isochrones since these isochrones are still a bit off at faint magnitudes and they are off at bright magnitudes as well.

Figure 2.3 depicts the stars that satisfy both the proper motion and photometric requirements (filled red circles). The blue line is the modified isochrone which determines the photometric membership of the PM-selected members and it matches the average location of the cluster members very well. The green-filled triangles and open magenta squares show the possible binary and multiple stars which are discussed in Section 2.5. We would like to emphasize that the shift we introduced in the PADOVA isochrone is not random. We have shifted the PADOVA isochrone in a way that it has a colour index equal to the mean colour index of all stars with $J > 12$ which have passed the astrometric test. A possible consequence of this shift on our results can be contamination by field stars at the low-mass end. However, since we will perform a second photometric test (explained below) which further filters out field stars, this is of no concern. Moreover, since the shift is horizontal, i.e. we have only changed the colours and not the magnitudes, and we will later calculate the stellar masses based on J magnitudes only, such a shift will not affect our mass

Table 2.2: Celestial coordinates, proper motions, magnitudes and the masses of the possible members of Praesepe sorted by right ascension. Table 2 is available in its entirety in the electronic version of Khalaj & Baumgardt (2013).

RA (J2000)	Dec. (J2000)	$\mu_\alpha \cos \delta$	μ_δ	J	K_s	Mass
(deg)	(deg)	(mas yr^{-1})	(mas yr^{-1})	(mag)	(mag)	(M$_\odot$)
126.423399	+19.511820	-33.0 ± 4.2	-14.0 ± 4.2	15.066 ± 0.039	14.168 ± 0.048	0.183
126.572703	+19.726598	-36.2 ± 4.2	-13.7 ± 4.2	13.896 ± 0.025	12.981 ± 0.024	0.327
126.597027	+19.551072	-35.6 ± 4.2	-22.8 ± 4.2	14.643 ± 0.032	13.696 ± 0.034	0.225
...	...	...	...	...	...	...
133.536124	+18.477437	-27.1 ± 3.7	-08.6 ± 3.7	11.910 ± 0.023	11.081 ± 0.020	0.675
133.541163	+19.946329	-26.6 ± 3.7	-12.8 ± 3.7	12.233 ± 0.020	11.385 ± 0.021	0.618
133.580451	+19.718509	-36.0 ± 3.7	-21.4 ± 3.7	11.090 ± 0.022	10.452 ± 0.018	0.825

determination for stars.

There are 1286 stars that satisfy both tests, however, due to the relatively large errors of proper motion and photometry of faint stars we expect a significant contamination of field stars for magnitudes $J > 12$ mag. In order to remove possible contaminants with $J > 12$ mag we apply a second photometric test using z magnitudes from SDSS and K_s magnitudes from 2MASS. Figure 2.4 and 2.5 show the position and the distribution of all stars with $J > 12$ mag in a z versus $z - K_\mathrm{s}$ diagram. One can see that in this CMD, the NextGen isochrone matches the actual position of possible members. As a result we use this isochrone to remove background stars photometrically. We require that each photometric member lies within 2.5σ of the isochrone (filled red circles) or its colour index differs by no more than $-0.1/+0.25$ mag from the corresponding colour index of the isochrone at the same magnitude (filled magenta circles). This additional condition is added since we observe that there are a number of stars (enclosed by the dashed blue lines in Figure 2.4), which are not identified as photometric members due to their small photometric errors but are concentrated towards the cluster centre and have a χ^2 distribution clustered around zero. As a result we keep these stars as photometric members. In contrast, the stars shown as filled grey circles in Figure 2.4 have a flat χ^2 distribution and are uniformly spread in our 3.5-degree survey field. We end up with 893 stars which satisfy the astrometric and all photometric tests. Figure 2.6 shows the spatial distribution of these stars. We also obtain the mass of the possible members by interpolating the theoretical masses from the PADOVA isochrone using the J magnitudes. These masses are listed in Table 2.2.
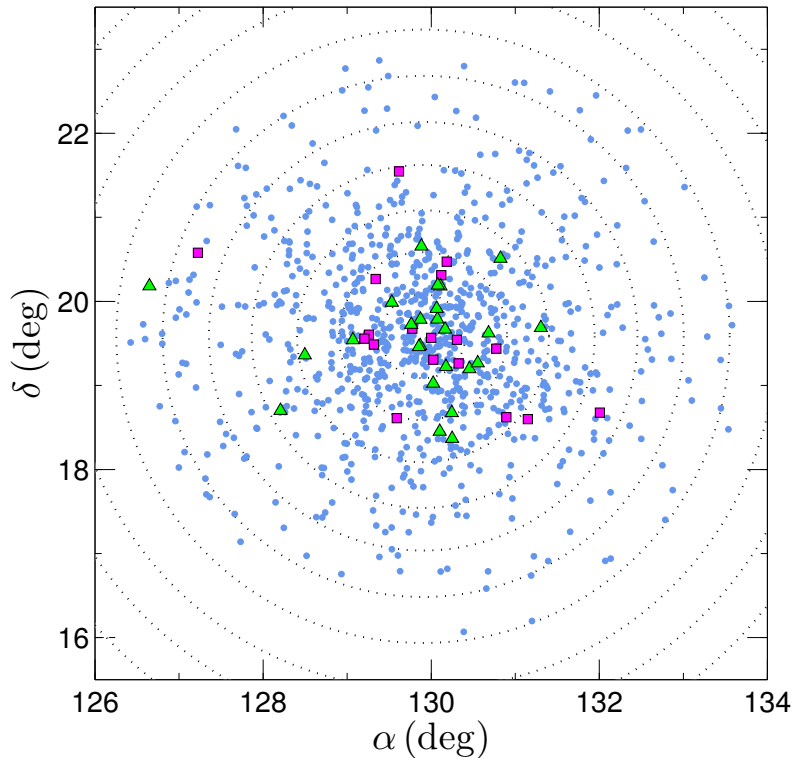
Figure 2.6: Spatial distribution of the possible cluster members of Praesepe (893 stars) with respect to the new centre of Praesepe. The filled green triangles and the filled magenta squares show possible binaries and multiples. Dotted grey circles are spaced by 0°.5.

2.3.3   Cluster centre

Before obtaining surface density plots, we first determine a new coordinate for the cluster centre (density centre). The density centre as defined by von Hoerner (1963) is the density weighted average of the positions of all stars:

$$\vec{r}_{d,j} \equiv \frac{\sum_i \vec{r}_i \rho_j^{(i)}}{\sum_i \rho_j^{(i)}} \tag{2.2}$$

where $\rho_j^{(i)}$ is the local density estimator of order j around the ith particle with position vector $\vec{r}_i$. We replace the 3D density estimator $\rho_j^{(i)}$ by the surface density $\Sigma_j^{(i)}$. To estimate $\vec{r}_{d,j}$ we adopt the unbiased form of the density estimator introduced by Casertano & Hut (1985) and consider the 10 nearest neighbours of each star to obtain $\Sigma_j^{(i)}$. We then obtain the new coordinate of the cluster centre as follows:

$$\alpha_{\text{centre}} = 8^h 39^m 37^s \quad \delta_{\text{centre}} = 19°35'02''$$

This new centre differs by about 5″ from the coordinate of the cluster centre given by Lynga

(1995) ($\alpha_{\text{centre}} = 8^h 40^m 00^s, \delta_{\text{centre}} = 19°30'00''$).

2.3.4 Surface density profile

To determine the distribution of member stars and the possible background stars, we first consider a field of 5° and divide this field into 18 radial bins from 0° to 5° where SDSS is ~ 95 per cent complete.

We then consider all stars that satisfy the astrometric and photometric selection criteria in this field and plot the surface density of faint ($11 < J \leq 15.5$), bright ($J \leq 11$) and all stars ($J \leq 15.5$) in each bin as a function of radius from the new centre of Praesepe in Figure 2.7. At the distance of Praesepe $J = 11$ mag corresponds to $m = 0.84 \, M_\odot$. Error bars only consider the statistical uncertainties in the number of stars. One can see that the density profiles do not level off beyond the tidal radius of Praesepe. This is in agreement with Küpper et al. (2010) who showed that the surface density profiles of star clusters extend beyond the tidal radius due to stars escaping the cluster. To estimate an upper limit for the density of background stars, we therefore consider the density of the last radial bin and find that the background density of stars is 2.17 ± 0.34 stars/deg^2, implying that there are still about 84 background stars within a field of 3.5 degrees from the centre of Praesepe. Since we found 893 candidate stars in total within the same area, the background contamination is ~ 10 per cent and needs to be considered when determining the mass function of cluster members and the total cluster mass. We will statistically subtract these background stars when deriving the mass function. The details of this subtraction are explained in Section 2.4.

Figure 2.8 shows the cumulative sums of stellar masses for faint, bright and all stars as a function of radius in the search field of 3°.5. The two-dimensional half-number radius and half-mass radius are 1°.34 and 1°.23 which correspond to 4.25 pc and 3.90 pc respectively. Assuming that the corresponding 3D radii are 1/3 larger than the projected radii, we find that the 3D half-number and half-mass radii are 5.67 and 5.20 pc respectively. Table 2.3 summarizes half-mass and half-number radii corresponding to faint, bright and all stars. The fact that the 2D half-mass and half-number radii of all cluster stars are about 2 times larger than those of bright stars evidently shows that Praesepe is strongly mass segregated. Mass segregation of Praesepe can also be inferred from Figure 2.9 which shows the average mass of the possible cluster members as a function of radius from the new cluster centre. One can see that the average mass of stars is $0.96 \pm 0.08 \, M_\odot$ inside 0.3 pc and drops down to $\sim 0.45 \, M_\odot$ outside the half-mass radius.

Table 2.3: Table of projected half-number and half-mass radii for cluster members

Type of stars	Number of stars	Half-number radius (2D)	Half-mass radius (2D)
Faint Stars	759 stars	1°.23	1°.34
$11 < J \leq 15.5$		3.90 pc	4.25 pc
Bright Stars	134 stars	0°.65	0°.64
$J \leq 11$		2.07 pc	2.04 pc
All Stars	893 stars	1°.34	1°.23
$J \leq 15.5$		4.25 pc	3.90 pc
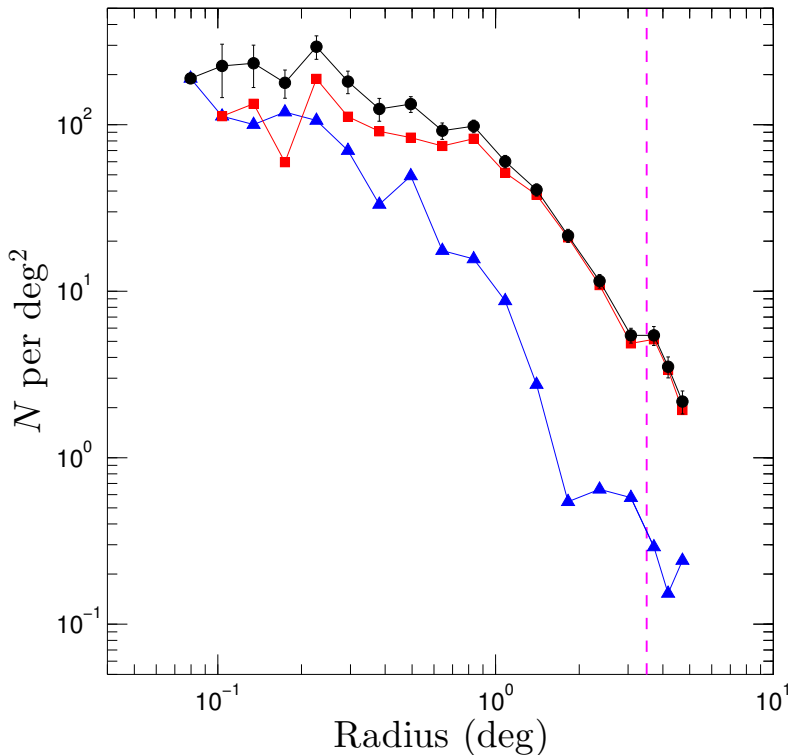
Figure 2.7: Surface density of all ($J \leq 15.5$, upper line), faint ($11 < J \leq 15.5$, middle line) and bright ($J \leq 11$, lower line) possible members in a 5-degree field around the centre of Praesepe. The dashed magenta line marks the tidal radius of Praesepe. To avoid confusion only error bars of the density of all stars are shown. The error bars are Poissonian.

2.4   Stellar mass function

As shown before, possible cluster members are mainly located within 3.5 degrees of the cluster centre so we restrict our study to stars within this radius when deriving the mass function. To obtain the mass function of the cluster members, we must statistically subtract the background level. The is done as follows:
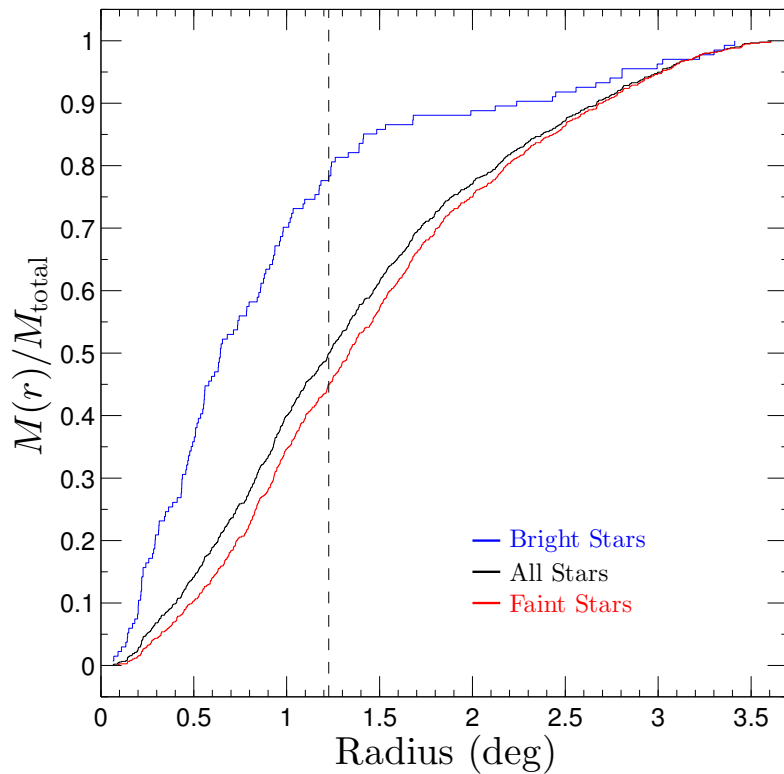
Figure 2.8: Normalized cumulative sums of stellar masses for bright (upper line), faint (lower line) and all (middle line) cluster members as functions of radius in a field of $3°\!.5$ from the new cluster centre. The dashed line intersects the total cumulative curve at half the maximum value corresponding to a half mass radius of $1°\!.23$ which is equivalent to $3.90\,\mathrm{pc}$.
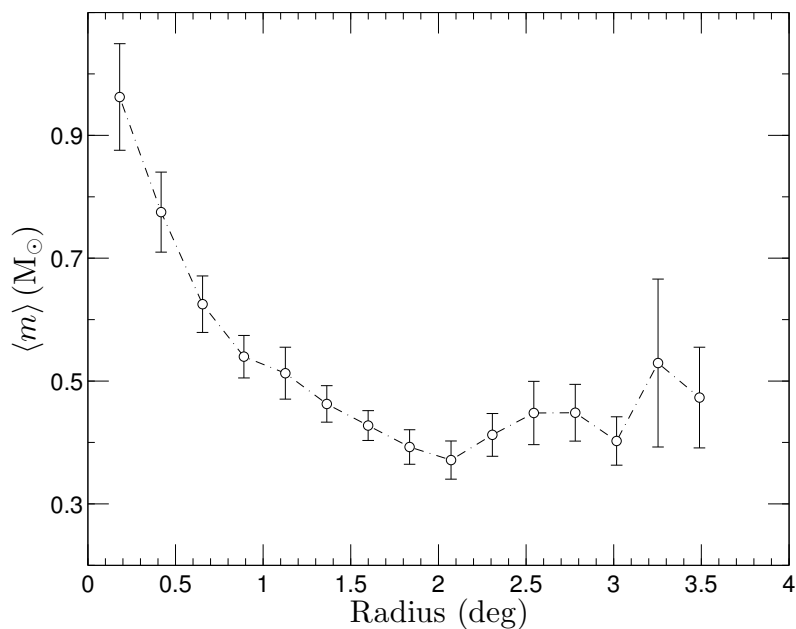
Figure 2.9: The average mass of the possible cluster members as a function of radius from the centre of Praesepe. The average mass is roughly constant beyond $1°\!.5$.

1. In Figure 2.7, we assume that all stars which reside between $4°$ and $5°$ are backgrounds stars.

2. We derive the mass function of these background stars.

3. We generate 84 random stars distributed according to the mass function derived in the previous step.

4. Using these stars, we select possible members with similar mass and remove them from the list of possible members.

The mass function for the possible members after background subtraction is shown in Figure 2.10. This figure shows that the mass function of Praesepe cannot be fitted by a single power-law distribution $\xi(m) = \mathrm{d}N/\mathrm{d}m \sim m^{-\alpha}$. As a result we assume that the mass function is described by a two-stage power-law distribution with a turnover at m_{t}, so that the mass function of stars with masses higher than m_{t}, hereafter high mass stars, is fitted by $\xi(m) \sim m^{-\alpha_{\mathrm{high}}}$, whereas the mass function of those lower than m_{t}, hereafter low mass stars, is fitted by $\xi(m) \sim m^{-\alpha_{\mathrm{low}}}$. The method we use to derive m_{t} and the value of each α is based on a maximum-likelihood fitting combined with a Kolmogorov-Smirnov test to evaluate the goodness of the fit. This method was introduced by Clauset et al. (2007) for the case that the exponent of the power-law α is greater than unity and there exists a lower bound to the data. We re-derive the relations for both $\alpha > 1$ and $\alpha < 1$ and when the data is bounded on two sides. The case of two-sided bounds is important in our case, since stars more massive than $2.20\,\mathrm{M}_\odot$ have evolved off the main sequence while stars less massive than $0.15\,\mathrm{M}_\odot$ are too faint to be detected. The details of this method and the derivation of α values and their corresponding errors are presented in sections 2.4.1 and 2.4.2. This method provides much more accurate results compared to using a least-squares method on binned data (Clauset et al., 2007).

2.4.1 Deriving α and its error $\sigma(\alpha)$

For a power law distribution with both lower and upper bounds (m_{min}, m_{max}) the probability density function is

$$p(x) = Cm^{-\alpha}$$

where C is the normalisation constant and $\alpha \neq 1$.

The likelihood of the data given the model with scaling parameter α is

$$p(m|\alpha) = \prod_{i=1}^{n}(1-\alpha)\frac{m_i^{-\alpha}}{m_{\max}^{1-\alpha} - m_{\min}^{1-\alpha}}$$

The logarithm $\mathcal{L}$ of the likelihood is

$$\mathcal{L} = \ln p(m|\alpha) = \ln \prod_{i=1}^{n}(1-\alpha)\frac{m_i^{-\alpha}}{m_{\max}^{1-\alpha} - m_{\min}^{1-\alpha}}$$

The *maximum likelihood estimate* for α is obtained when

$$\frac{\partial\mathcal{L}}{\partial\alpha} = 0$$

Setting $X = \dfrac{m_{\max}}{m_{\min}}$, we obtain

$$\frac{\partial\mathcal{L}}{\partial\alpha} = \frac{n}{\alpha-1} - \sum_{i=1}^{n}\ln\frac{m_i}{m_{\min}} + n\frac{\ln X}{1-X^{\alpha-1}}$$

$$\rightarrow \alpha = 1 + n\left[\sum_{i=1}^{n}\ln\frac{m_i}{m_{\min}} - n\frac{\ln X}{1-X^{\alpha-1}}\right]^{-1} \tag{2.3}$$

Equation (2.3) is a general formula which holds for both $\alpha < 1$ and $\alpha > 1$. In general one needs to use numerical methods to calculate α from equation (2.3) since there is no general analytic solution to this equation. However, if we assume that there is only a lower bound on data then for $\alpha > 1$ the last term of equation (2.3) vanishes and there is an analytic solution as follows (also given in Clauset et al. 2007)

$$\alpha = 1 + n\left[\sum_{i=1}^{n}\ln\frac{m_i}{m_{\min}}\right]^{-1}$$

To estimate the error of α we need to calculate the variance of α as explained in Fisher (1922) which is

$$\sigma^2(\alpha) = -\left(\frac{\partial^2\mathcal{L}}{\partial\alpha^2}\right)^{-1} \tag{2.4}$$

By substituting $\mathcal{L}$ into equation (2.4) one obtains

$$\sigma(\alpha) = \frac{1}{\sqrt{n}}\left((\alpha-1)^{-2} - \ln^2 X\frac{X^{\alpha-1}}{(1-X^{\alpha-1})^2}\right)^{-1/2} \tag{2.5}$$

Again if we assume that there is only a lower bound on data then for $\alpha > 1$, equation (2.5) reduces to the following equation which is given in Clauset et al. (2007)

$$\rightarrow \sigma(\alpha) = \frac{|\alpha - 1|}{\sqrt{n}}$$

2.4.2   Finding the mass function turnover (break point)

So far we have derived equation (2.3) and equation (2.5) to estimate α and its error $\sigma(\alpha)$. However, often mass functions of stellar clusters show a turnover. To find the mass function turnover we proceed as follows:

1. Decide on the mass range in which the turnover (m_t) lies. Let I_M denote the selected mass range.

2. Pick a mass (say m_x) from I_M.

3. Fit two power law functions to the data. One from m_min to m_x and the other from m_x to m_max. Calculate the corresponding α values using (2.3). Note that m_min and m_max correspond to the whole mass range and not to I_M defined in the 1st step.

4. Make two theoretical power law distributions using the calculated α values and combine these two theoretical distributions to obtain one overall distribution for the whole mass range.

5. Compare this distribution with the observed distribution using a Kolmogorov Smirnov (K-S) test and record the K-S statistic D.

6. Vary m_x in I_M until D obtains a minimum. The mass for which D becomes minimized is the turnover.

Following the procedure explained above, one can see that m_t, α and $\sigma(\alpha)$ are calculated all at once.

Using the method mentioned above, we find that a K-S test indicates with high confidence (5 per cent significance level) that the turnover in the mass function is at $m_\mathrm{t} = 0.65\,\mathrm{M_\odot}$ which is also visible in the figure. We also obtain $\alpha_\mathrm{low} = 0.85 \pm 0.10$ and $\alpha_\mathrm{high} = 2.88 \pm 0.22$ for low and high mass stars respectively. According to the K-S test our result for the overall mass function

would also be consistent with a turnover at $0.5\,\mathrm{M_\odot}$ and in such a case the mass functions slopes would be $\alpha_{\mathrm{low}} = 0.72 \pm 0.13$ and $\alpha_{\mathrm{high}} = 2.51 \pm 0.15$ (close to $\alpha = 2.35$ found by Salpeter 1955).

The slope and the turnover point of the mass function reflect the underlying thermodynamics, feedback physics, galactic properties and the different physical processes involved in the formation of low and high-mass stars (Guszejnov & Hopkins, 2015). If the content of the cluster is fully mixed the turnover point is expected to be the same and not vary with radius. In such a case the mass segregation only changes the relative ratio of high to low-mass stars at each radius which only affects the slope of the mass function. Since the total mass of Praesepe is about $\sim 500\,\mathrm{M_\odot}$ and the 3D half-mass radius is $\sim 5.20\,\mathrm{pc}$, the age of Praesepe is approximately ~ 5 times its relaxation time and one can assume that the stellar content of the cluster has thoroughly mixed in the entire cluster, meaning that the location of the turnover in the mass function should not change from one point to another. We therefore fix the location of the turnover and derive the mass function slopes inside and outside the half-mass radius. We find that the mass function slope of massive stars inside the half-mass radius ($\alpha = 2.32 \pm 0.24$) is less steep than the overall slope ($\alpha_{\mathrm{high}} = 2.88 \pm 0.22$). However in the outer radial bin, the mass function of massive stars becomes steeper ($\alpha = 4.90 \pm 0.51$), and this is again indicating mass segregation in Praesepe.

To correct for the effect of unresolved binaries on the observed mass function, we did a series of a simulations which are discussed in Section 2.5.

2.4.3   Comparison to other works

Table 2.4 compares mass function slopes for Praesepe as obtained by various studies within the last 20 years. In this table only those studies whose mass range overlaps our studied mass range are listed.

We obtain $\alpha = 0.85 \pm 0.10$ for stars in the mass range $0.15 \leq m/\,\mathrm{M_\odot} \leq 0.65$. Within the error bars, this value is in good agreement with Baker et al. (2010) and Boudreault et al. (2012), however it is steeper than the value found by Adams et al. (2002). This disagreement, as discussed by Boudreault et al. (2010), is most likely due to the fact that the membership criterion of Adams et al. (2002) is based on a threshold for the membership probability of only $p = 0.01$, which increases the likelihood of contamination by background stars. The value that we have found for the low-mass slope of the mass function is less steep than the values found by Hambly et al. (1995)($\alpha = 1.5$), Kraus & Hillenbrand (2007)($\alpha = 1.4 \pm 0.2$) and Boudreault et al. (2010)($\alpha = 1.8 \pm 0.1$). The discrepancy with Boudreault et al. (2010) is due to the fact that they identified the members of
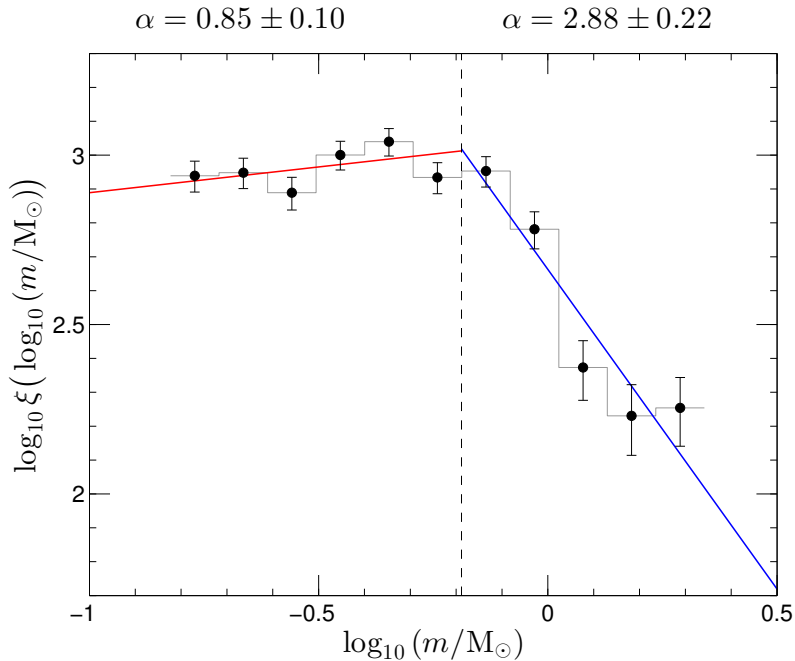
Figure 2.10: Mass function of stars in Praesepe corrected for background stars. Error bars of data points are Poissonian. Dashed line which corresponds to $m = 0.65\,M_\odot$ shows the point at which the mass functions has a turnover. Red ($\alpha = 0.85 \pm 0.10$) and blue ($\alpha = 2.88 \pm 0.22$) lines show the best fit to the mass function of low-mass and high-mass stars respectively. While in this figure data is binned, the procedure we use to determine the α values does not work with binned data.

Praesepe only through photometry, while Boudreault et al. (2012) used proper motions combined with photometry, which led to the rejection of more background stars. Boudreault et al. (2012) found 1116 members for Praesepe among which 855 stars have $J \leq 15.5\,\mathrm{mag}$ (our survey limit) and 552 of these stars ($\sim 65\,\mathrm{per\,cent}$) are recovered by our analysis.

Hence, three recent independent studies (our work, Boudreault et al. 2012 and Baker et al. 2010) show a turnover at $\sim 0.5 \pm 0.1\,M_\odot$ in the mass function and a slope of $\alpha \approx 0.8$ for the mass function before the turnover.

2.5   Binary fraction

Figure 2.3 shows that there are a number of stars which reside above the main sequence of the isochrone (filled green triangles). This deviation is significantly outside the error bars for the photometry, so it suggests the presence of binary systems in the cluster. The CMD shows that there are also stars (depicted by open magenta squares in Figure 2.3) that are more than 0.75 mag above the isochrone. Since these stars show a strong concentration towards the cluster centre

Table 2.4: A comparison of different profiles obtained for global mass function of Praesepe.

Reference	Low-mass slope of the mass function	High-mass slope of the mass function
This work	$\alpha = 0.85 \pm 0.10$	$\alpha = 2.88 \pm 0.22$
	$0.15 \leq m/\mathrm{M}_\odot \leq 0.65$	$0.65 \leq M/M_\odot \leq 2.20$
corrected for binaries	$\alpha = 1.05 \pm 0.05$	$\alpha = 2.80 \pm 0.05$
Boudreault et al. (2012)	$\alpha = 0.63 \pm 0.11^a$	–
	$0.062 \leq m/\mathrm{M}_\odot \leq 0.695$	–
Boudreault et al. (2010)	$\alpha = 1.8 \pm 0.1$	–
	$0.1 \leq m/\mathrm{M}_\odot \leq 0.6$	–
	$\alpha = 1.10 \pm 0.37$	–
	(Z band) $0.125 \leq m/\mathrm{M}_\odot \leq 0.6$	–
Baker et al. (2010)	$\alpha = 1.07$	–
	(J band) $0.20 \leq m/\mathrm{M}_\odot \leq 0.5$	–
	$\alpha = 1.09$	–
	(K band) $0.20 \leq m/\mathrm{M}_\odot \leq 0.5$	–
Kraus & Hillenbrand (2007)	$\alpha = 1.4 \pm 0.2$	–
	$0.12 \leq m/\mathrm{M}_\odot \leq 1$	–
Adams et al. (2002)	$\alpha = 0$	$\alpha = 1.6$
	$0.1 \leq m/\mathrm{M}_\odot \leq 0.4$	$0.4 \leq m/\mathrm{M}_\odot \leq 1$
Hambly et al. (1995)	$\alpha = 1.5$	
	$0.1 \leq m/\mathrm{M}_\odot \leq 0.5$	

a) The value of $\alpha = 0.63 \pm 0.11$ is not reported in Boudreault et al. (2012). We derive this value using the original data given in Table 3 of the corresponding paper.

as shown in Figure 2.6, they are most likely cluster members and are therefore either binaries or higher order multiple systems.[4]

There are 25 stars that deviate from the isochrone by more than 2.5σ, where σ refers to the mean error of the photometry. The corresponding binary fraction, which we define as the fraction of binary systems $f_{\mathrm{bin}} = N_{\mathrm{bin}}/(N_{\mathrm{sing}} + N_{\mathrm{bin}})$ is therefore 8.47 per cent ± 1.55 per cent for $7.05 \leq J \leq 12.35$.

In order to recover the true binary fraction and the true mass function, we simulate the effect of binaries through a number of MC simulations by constructing non-random pairs out of the single stars, assuming that the likelihood of each star to be chosen as a primary increases linearly with the logarithm of its mass, similar to what is seen in recent simulations of star formation (e.g. Bate 2009).

---

[4]By higher order multiples we mean triple, quadruple and more complex systems.
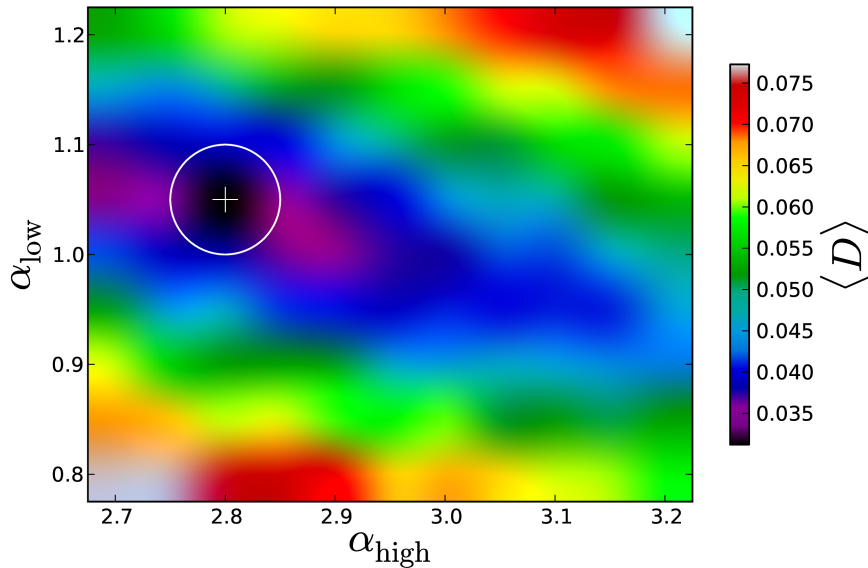
Figure 2.11: The value of the K-S statistic D between the outcome of the simulations (averaged over 50 different random seed numbers) and the observed mass function as a function of α_{low} and α_{high} for an assumed binary fraction of $f_{\mathrm{bin}} = 35$ per cent. The white cross shows the location of the best match with observation. The white circle represents the lower limit of the errors in our simulation

The procedure that we have adopted to derive the true binary fraction and mass function in our simulations is as follows:

1. Create a model cluster using a two-stage mass function with a slope for low-mass stars α_{low} and a slope for high-mass stars α_{high}.

2. Derive J and K_{s} magnitudes of the stars using the modified PADOVA isochrone.

3. Select each primary component of a binary with a probability which is proportional to $\log_{10}(m_{\mathrm{prim}}/m_{\mathrm{min}})$. Here m_{prim} is the mass of each primary component and m_{min} is the minimum mass of all stars in the mass function.

4. Select each secondary component (J_2, K_{s2}) based on a uniform (flat) distribution for mass ratios ($q = m_s/m_p$) between $0 < q < 1$.

5. Compute the total magnitude of the binary system:

$$J_{\mathrm{(binary)}} = -2.5 \log(10^{-0.4 J_1} + 10^{-0.4 J_2}) \tag{2.6}$$

$$K_{\mathrm{s(binary)}} = -2.5 \log(10^{-0.4 K_{s1}} + 10^{-0.4 K_{s2}}) \tag{2.7}$$

6. Add synthetic photometric errors to the magnitudes derived in the previous section. The synthetic photometric errors are generated in such way that they replicate the photometric errors of stars in PPMXL.

7. Determine the binary systems that deviate significantly from the isochrone and count them as observed binaries.

8. Compare the observed binary fraction in the simulation with the binary fraction from the simulation and the mass function of the single stars and non-detected binaries with the observed mass function.

9. Change the parameters of the IMF and the assumed binary fraction until the best match in terms of the K-S statistic D with the observed mass function and the observed binary fraction is found.

The range of parameters that we use in our simulations to generate the model clusters is:

- $\alpha_{\rm low} \in [0.8 : 0.05 : 1.2]$

- $m_{\rm t} = 0.65\,{\rm M}_\odot$

- $\alpha_{\rm high} \in [2.7 : 0.05 : 3.2]$

In order to reduce statistical random errors we run our simulation for 50 different random seed numbers and then take an average over the K-S statistic D and $f_{\rm bin}$(observed) for each set of given parameters.

According to our simulations, an assumed binary fraction of $f_{\rm bin} = 35\,{\rm per\,cent} \pm 5\,{\rm per\,cent}$ in the mass range $0.6 \leq m/\,{\rm M}_\odot \leq 2.20$ ($7.05 \leq J \leq 12.35$) and an IMF with $\alpha_{\rm low} = 1.05 \pm 0.05$ and $\alpha_{\rm high} = 2.80 \pm 0.05$ yields the best agreement with the observed mass function and observed binary fraction. The fact that $\alpha_{\rm low}$ which is obtained from simulations is steeper than the observed (uncorrected) value is to be expected since many low-mass stars will be hidden in binaries with more massive companions.

Figure 2.11 shows the value of K-S statistic D as a function of $\alpha_{\rm low}$ and $\alpha_{\rm high}$ for $f_{\rm bin} = 35\,{\rm per\,cent}$. The best match with the observation is obtained by minimizing the value of D and its location in the parameter space is shown by the white cross. As shown in the figure, one can see that the value of D strongly depends on $\alpha_{\rm low}$ in contrast to $\alpha_{\rm high}$ which does not change the value of D significantly.

Our simulations also reveal that due to photometric errors, a fraction of binaries scatter above the isochrone by more than $\Delta J = 0.75 \, \mathrm{mag}$ and are identified as fake multiples. According to our simulations, from 18 multiples detected in the CMD, 7 ± 2 can be explained by binaries this way. The rest are likely to be genuine multiples.

For comparison, Bouvier et al. (2001) found a binary fraction of $25.3 \pm 5.4 \, \mathrm{per\,cent}$ for 149 G and K dwarfs observed in Praesepe using adaptive optics. According to our best fitting model, we find a binary fraction of $30 \pm 5 \, \mathrm{per\,cent}$ for the same mass range which is roughly consistent with the results of Bouvier et al. (2001).

Finally, we estimate the total cluster mass. By summing up the masses of members obtained from our modified PADOVA isochrone and subtracting the contribution of contaminants we derive a total mass of $424 \, \mathrm{M_\odot}$. By extending the global mass function profile to $0.08 \, \mathrm{M_\odot}$ to compensate for missing low mass stars, this value increases to $448 \, \mathrm{M_\odot}$. Assuming that there are no black holes or neutron stars left in the cluster, we also extend the global mass function profile to an initial mass of $8 \, \mathrm{M_\odot}$ to calculate the contribution of white dwarfs to the total mass. We adopt the semi-empirical relation from Kalirai et al. (2008) which gives the final mass of white dwarfs as a function of the initial masses of the main-sequence progenitors. After this correction, the total mass is $465 \, \mathrm{M_\odot}$. Due to binaries, which increase the mass by approximately a factor of 0.35, we derive a total mass of $\approx 630 \, \mathrm{M_\odot}$ for Praesepe.

2.6   Summary

We have identified 893 possible members of Praesepe using proper motions from the PPMXL catalogue and J and K_s photometry from the 2MASS and z photometry from SDSS in a field of $3°\!.5$ from the cluster centre.

We then calculated a new density centre for the cluster as defined by von Hoerner (1963) using the unbiased form of the local density estimator from Casertano & Hut (1985). Using this new cluster centre ($\alpha_{\mathrm{centre}} = 8^h 39^m 37^s$, $\delta_{\mathrm{centre}} = 19°35'02''$) we derived the surface density profile, 2D half-number ($4.25 \, \mathrm{pc}$) and half-mass radii ($3.90 \, \mathrm{pc}$) for Praesepe. We found that Praesepe is strongly mass segregated.

We derived the global and radial mass functions of Praesepe. The global mass function of Praesepe is a two-stage power law with $\alpha_{\mathrm{low}} = 0.85 \pm 0.10$ and $\alpha_{\mathrm{high}} = 2.88 \pm 0.22$ for low and high mass stars respectively and with a turnover at $0.65 \, \mathrm{M_\odot}$. The value we have obtained for the slope

of the mass function for low-mass stars ($\alpha_{\text{low}} = 0.85 \pm 0.10$) is consistent with Baker et al. (2010) and Boudreault et al. (2012). The presence and location of the turnover in the mass function at $m = 0.65\,\text{M}_\odot$ is in agreement with Boudreault et al. (2012) who found that the mass function of Praesepe has a maximum at $\sim 0.6\,\text{M}_\odot$. We also found that the high-mass slope of the radial mass functions increases from inner to outer radii, providing further evidence for mass segregation in Praesepe.

From an inspection of the CMD of Praesepe, we also identified 25 binaries and 18 multiple stars. Including unresolved binaries in the CMD, we did a series of simulations to recover the true binary fraction and the true IMF. According to our simulations the model which shows the best agreement with the observed mass function and binary fraction has an underlying mass function similar to the observed mass function but an overall binary fraction of $f_{\text{bin}} = 35\,\text{per cent} \pm 5\,\text{per cent}$.

Finally, we derive a mass of $424\,\text{M}_\odot$ for Praesepe from the visible stars after subtracting the contribution of contaminants. By considering the contribution of low mass stars, white dwarfs and unresolved binaries this value increases to $\approx 630\,\text{M}_\odot$

3

Solutions to the mass-budget problem in GCs
with MSPs

In this chapter we study the possible solutions to the mass-budget problem in GCs with MSPs, i.e. top-heavy IMF and significant mass-loss. For both the AGB and FRMS scenario, we derive the range of mass-loss levels and IMF high-mass slopes which produce the observed fraction of chemically peculiar stars and M/L ratios of Galactic GCs.

The chapter is structured as follows. In Section 3.1 the possible solutions to the mass-budget problem are studied. Section 3.2 discusses the effect of helium-enhancement on the observed number ratio of SG stars and we summarize the chapter in Section 3.3.

3.1 M/L ratios of MSPs

In Chapter 1.2.2 it was mentioned that Dabringhausen et al. (2009) found that a top-heavy IMF will lead to high M/L ratios in old stellar systems ($t = 12\,\mathrm{Gyr}$) such as UCDs and GCs. However, the results obtained by Dabringhausen et al. (2009) do not necessarily hold for GCs. There are three reasons that can be mentioned for this.

First, they assumed that UCDs are single stellar population (SSP) systems. The M/L ratio for a GC with MSPs can be lower than that of a system with only an SSP. This can be shown as follows. The M/L ratio of an SSP in the V-band is

$$\Upsilon_V(\mathrm{SSP}) = \frac{M}{L_V} = \frac{M_1 + M_{\mathrm{rem}}}{L_{V1}} = \frac{M_1}{L_{V1}} + \frac{M_{\mathrm{rem}}}{L_{V1}} \tag{3.1}$$
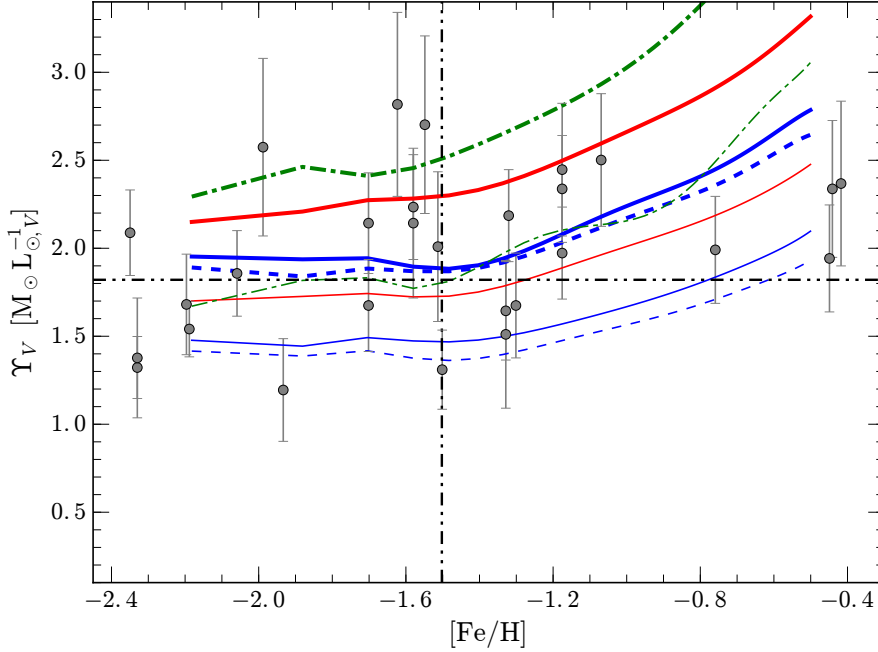
Figure 3.1: Mass-to-light ratio of a sample of Galactic GCs (Baumgardt et al. 2016, MNRAS, submitted) and that of a SSP derived from either PARSEC (blue lines) and Dartmouth isochrones (red lines) as a function of metallicity in the V-band. The dashed and solid lines correspond to Chabrier (2003) and Kroupa (2001) IMFs, and the thin and thick lines denote SSPs with ages of $T = 8\,\mathrm{Gyr}$ and $T = 12\,\mathrm{Gyr}$ respectively. The dash-dotted green lines correspond to Dartmouth M/L ratios with $[\alpha/\mathrm{Fe}] = +0.4$. The dashed black lines mark the weighted mean metallicity and the M/L ratio of the sample, i.e. $[\mathrm{Fe/H}] = -1.5$ and $\Upsilon_V = 1.8\,\mathrm{M_\odot\,L_{\odot,V}^{-1}}$. One can see that the M/L ratios of the Galactic GCs do not show any clear trend with metallicity. Therefore, we use the mean M/L ratio as the observational constraint.

where M_1, M_rem and L_{V1} are the total mass of long-lived low-mass stars, total mass of remnants and the total luminosity in the V-band. Here we have assumed that M_rem does not include the mass of the gas which has been lost by massive stars (via e.g. stellar winds or SN explosions), i.e. the cluster is gas free. For a GC with MSPs the ejected gas from FG stars will turn into new stars. Assuming that the IMF of SG stars only extends to $\lesssim 0.8\,\mathrm{M_\odot}$[1], they will not create any remnants after a Hubble time. The luminosity and mass of SG stars can be approximated by

$$M_2 = M_1\frac{N_2}{N_1}, \quad L_{V2} = L_{V1}\frac{N_2}{N_1} \tag{3.2}$$

---

[1]The upper mass limit of stars which do not produce any remnants can vary depending on the age and the metallicity of the cluster. As a result, $0.8\,\mathrm{M_\odot}$ can be considered as a lower limit which corresponds to very old GCs ($T > 10\,\mathrm{Gyr}$), for younger clusters it is larger.

So Υ_V for such a system is equal to

$$\Upsilon_V(\text{MSP}) = \frac{M_1 + M_1 \times \frac{N_2}{N_1} + M_{\text{rem}}}{L_{V1} + L_{V1} \times \frac{N_2}{N_1}} = \frac{M_1(1 + N_2/N_1) + M_{\text{rem}}}{L_{V1}(1 + N_2/N_1)} = \frac{M_1}{L_{V1}} + \frac{M_{\text{rem}}}{L_{V1}(1 + N_2/N_1)}$$

$$\Upsilon_V(\text{MSP}) = \frac{M_1}{L_{V1}} + \frac{M_{\text{rem}}}{L_{V1}} \frac{1}{(1 + N_2/N_1)} \tag{3.3}$$

Note that the upper mass limit of the IMF of SG stars is not known yet. It can extend from the upper mass-limit of long-lived stars in a GC ($\sim 0.8 - 1.0\,\text{M}_\odot$) to $8.0\,\text{M}_\odot$. In this chapter we assume the former which means that SG stars will not produce any remnants. This assumption is based on the studies of Prantzos & Charbonnel (2006) and Decressin et al. (2007b) which state that such an assumption minimizes the constraint on the IMF of polluters (i.e. FG stars). In other words if we assume that the upper mass limit is larger, then resolving the mass-budget problem requires higher mass-loss levels or shallower high-mass slopes for the IMF, i.e. the mass-budget problem gets even worse. SG stars cannot be more massive than $8.0\,\text{M}_\odot$, since in this case they will explode as SN and in the AGB scenario this will cause the iron abundance of SG stars to be different from that of FG stars which is not consistent with observations (D'Ercole et al., 2008). Depending on the age and the metallicity of the cluster the upper mass limit of long-lived stars in GCs lies in the range $\sim 0.8 - 1.0\,\text{M}_\odot$. In our models in this chapter (explained further below) we assume that the upper mass limit for the IMF of SG stars is $1.0\,\text{M}_\odot$, this lets us leave the break point of the Chabrier (2003) IMF unchanged (which is at $1.0\,\text{M}_\odot$) and only change the slope of the mass function at the high-mass end. Note that later in Chapter 4, to be consistent with D'Ercole et al. (2008) we assume that the IMF of SG stars extends to $8.0\,\text{M}_\odot$.

A comparison between equation (3.1) and equation (3.3) shows that they differ only in the second term by a factor of $1/(1 + N_2/N_1)$. Since N_2/N_1 is always non-negative we conclude that $\Upsilon_V(\text{MSP}) \leq \Upsilon_V(\text{SSP})$, i.e.

$$\frac{N_2}{N_1} > 0 \implies \frac{1}{(1 + N_2/N_1)} < 1 \implies \Upsilon_V(\text{MSP}) \leq \Upsilon_V(\text{SSP})$$

Second, for an SSP a top-heavy IMF leads to an increase in M_{rem} and consequently $\Upsilon_V(\text{SSP})$. For a GC with MSPs this is not the case as can be seen from equation (3.3). A top-heavy IMF increases M_{rem} but it also increases N_2/N_1. Since these parameters are respectively in the numerator and denominator of equation (3.3) they can cancel out or weaken the effect of each other. The exact behavior of equation (3.3) highly depends on the enrichment scenario (e.g. AGB

or FRMS).

Third, dynamical evolution can affect M/L ratios of GCs (e.g. Baumgardt & Makino 2003). Dabringhausen et al. (2009) ignored this effect as UCDs have a relaxation time which is of the order of a Hubble time or larger (Dabringhausen et al., 2009). This implies that in contrast to GCs the effect of the dynamical evolution on UCDs is negligible.

These reasons motivated us to examine the effect of a top-heavy IMF in conjunction with mass-loss on the M/L ratios of GCs with MSPs equation (3.3). In order to examine whether a top-heavy IMF in conjunction with mass-loss can simultaneously explain the observed fraction of SG stars and also the M/L ratios of Galactic GCs we evolve the CMD of GCs with two stellar populations using DARTMOUTH (Dotter et al., 2008; Feiden et al., 2011) isochrones since these isochrones are capable of dealing with helium and alpha enhancement. This is important since GCs have typical [α/Fe] values of ~ 0.4 (Carretta et al., 2010). Figure 3.1 compares the M/L ratios of a sample of Galactic GCs with SSP models of GCs obtained from the synthetic PARSEC isochrones (Bressan et al., 2012; Marigo et al., 2013; Tang et al., 2014; Chen et al., 2014; Rosenfield et al., 2016) and DARTMOUTH isochrones as a function of metallicity. Here, we do not consider the evaporation of stars due to dynamical evolution. According to this figure one can see that the M/L ratios for the model with alpha-enhancement [α/Fe] $= +0.4$ are higher than those with [α/Fe] $= 0.0$. The M/L ratios of the Galactic GCs have been obtained by fitting the velocity dispersion and surface density profiles of N-body models of GCs to the observed profiles of GCs (Baumgardt et al., 2016, in preparation).

In our models, the metallicity and alpha-enhancement of GCs are [Fe/H] $= -1.5$ and [α/Fe] $= +0.4$ respectively. We assume that the mass function of SG and low-mass FG stars is a Chabrier (2003) IMF for disk and young clusters, i.e.

$$\xi(m) = \frac{\mathrm{d}N}{\mathrm{d}m} \propto \frac{1}{m} \exp\left(-\frac{1}{2}\left(\frac{\log\left(m\right) - \log\left(m_c\right)}{\sigma}\right)^2\right), \quad 0.1 \leq m/\,\mathrm{M}_\odot < 1.0$$

where $m_c = 0.079^{+0.021}_{-0.016}\,\mathrm{M}_\odot$ and $\sigma = 0.69^{+0.05}_{-0.01}$. For more massive FG stars we assume that the mass function is a power-law, i.e. $\xi(m) \propto m^{-\alpha_{\mathrm{high}}}$ $\quad(1.0 \leq m/\,\mathrm{M}_\odot < 120)$, where for a standard (Salpeter, 1955) IMF the index of the power-law is $\alpha_{\mathrm{high}} = 2.3$.

The IMF we assume here for our GCs is different from the mass function that we derived for Praesepe (Chapter 2) as an example of a young cluster ($T = 590\,\mathrm{Myr}$; Fossati et al. 2008) in the Milky Way. We found that the PDMF of Praesepe can be described by a two-stage power-law

which has a turnover at $0.65\,\mathrm{M_\odot}$ and its slopes for low and high-mass stars are $\alpha_{\mathrm{low}} = 0.85 \pm 0.10$ and $\alpha_{\mathrm{high}} = 2.88 \pm 0.20$ respectively. As a result, compared to the IMF of young clusters and disk stars (Salpeter, 1955; Kroupa, 2001; Chabrier, 2003), the PDMF of Praesepe for low-mass stars is flatter and for high-mass stars is steeper. This can be attributed to stellar and dynamical evolution. Due to stellar evolution, star clusters lose their high-mass stars which causes α_{high} to become larger (steeper). Moreover, dynamical evolution causes mass segregation in the cluster which consequently leads to the preferential loss of low-mass stars and makes the mass function flatter at the low-mass end. The amount by which the aforementioned effects change the mass function of a cluster depends on the age of the cluster. For example, a comparison between Praesepe and the Trapezium cluster ($T = 1.0\,\mathrm{Myr}$; Muench et al. 2002) reveals that the observed mass function of the Trapezium cluster is closer to the canonical IMF owing to its younger age. Moreover, there are studies which show that the IMF can be top-heavy, i.e. $\alpha_{\mathrm{high}} < 2.3$ (e.g. Dabringhausen et al. 2009; Marks & Kroupa 2010; Hasani Zonoozi et al. 2016). As a result the PDMF of Praesepe cannot be used as a reference for our models, since our models correspond to GCs with a top-heavy IMF.

For the mass of white dwarfs we adopt the initial-final mass relation from Kalirai et al. (2008)

$$m_{\mathrm{WD}} = (0.109 \pm 0.007)m_{\mathrm{initial}} + 0.394 \pm 0.025\,\mathrm{M_\odot} \tag{3.4}$$

and for the mass of neutron stars and black holes we use the relations given by Spera et al. (2015).

In order to calculate the mass of the ejecta which are produced by FG stars and then form SG stars, we consider two different cases, namely the AGB and the FRMS scenario. For the AGB scenario the mass of the ejecta is $m - m_{\mathrm{WD}}$ where m_{WD} is given by equation (3.4). For the FRMS scenario, we assume that the mass of the ejecta is given by models computed by Decressin et al. (2007a) for rotating stars. In addition, we assume that ejecta of FG stars are further diluted with pristine gas of the same quantity, i.e. a dilution factor of 100% (Decressin et al., 2007b).

In our models, we vary the high-mass slope α_{high} in the range $[0.7 - 2.3]$ and consider different stellar mass-loss levels, denoted by f_m, from 0 to 1.0 for FG stars. We then calculate the number ratio of SG to FG stars as well as the M/L ratios. For clusters with no mass-loss we assume that the white dwarf retention fraction is 100% and for dark remnants (neutron stars and black holes) it is much less, i.e. $f_{\mathrm{ret}}(\mathrm{WD}) = 100\%$ and $f_{\mathrm{ret}}(\mathrm{dark}) \lesssim 30\%$ when $f_m = 0$. This assumption is based on studies, e.g. from the proper motions of radio pulsars (Lyne & Lorimer, 1994) or the distribution of X-ray binaries containing stellar mass black holes (Repetto et al., 2012; Janka,

2013), which have shown that dark remnants kick velocities are of the order of $100 - 400 \, \mathrm{km \, s^{-1}}$. The escape velocities of Galactic GCs at their centre and at their half-mass radii are typically below $30 \, \mathrm{km \, s^{-1}}$ (Gnedin et al., 2002). This implies that many of the dark remnants leave. For clusters whose FG mass-loss is nonzero we assume that the retention fraction of remnants decreases linearly as a function of mass-loss, i.e.

$$f_{\mathrm{ret}} = f_{\mathrm{ret0}}(1 - \kappa f_m) \tag{3.5}$$

where f_{ret0} is the retention fraction when FG mass-loss is zero and κ is a coefficient which specifies how sensitive the retention fraction is to the FG mass-loss. We have $N = 10^7$ stars for each model and repeated each simulation 10 times with different random seed numbers to minimize the statistical fluctuations in our results.

We compare the SG fraction of our models with the observed value for the SG fraction in GCs with MSPs ($N_2 \sim 0.7 \pm 0.1$; Carretta et al. 2010). Moreover, we compare the M/L ratios of our models with the mean M/L ratio of the Galactic GCs ($\Upsilon_V = 1.8 \, \mathrm{M_\odot \, L_{\odot,V}^{-1}}$). Our results are illustrated in Figs. 3.2 to 3.5 which show the contour maps of M/L ratios and the number ratio of SG stars for our model clusters as a function of α_{high} and f_m for the AGB and FRMS scenario. According to these figures one can see that to explain the observed number ratio of SG stars, for GCs with a canonical IMF the mass-loss from FG stars needs to be ~ 0.85 in the AGB scenario, whereas for the FRMS scenario this value is ~ 0.9. However, assuming no mass-loss and a top-heavy IMF for GCs, the FRMS scenario needs a high-mass slope of $\alpha_{\mathrm{high}} = 1.75$, whereas for the AGB the IMF needs to be flatter, i.e $\alpha_{\mathrm{high}} = 1.4$. This is due to the fact that the AGB scenario only contains stars with $m < 9.0 \, \mathrm{M_\odot}$, but FG polluters in the FRMS scenario can be as massive as $120 \, \mathrm{M_\odot}$. As a result, initially FRMS provides less ejecta than AGB stars, but as we decrease the high-mass slope FRMS ejecta exceed that of AGB stars.

In addition, one can see that irrespective of the assumed retention fraction for remnants, a top-heavy IMF for the FRMS scenario is consistent with the observed M/L ratios of Galactic GCs (with a mean $\Upsilon_V = 1.8 \, \mathrm{M_\odot \, L_{\odot,V}^{-1}}$). However, this is not the case for the AGB scenario as a top-heavy IMF needs to be accompanied with some mass-loss to lead to M/L ratios consistent with Galactic GCs. Depending on the retention fraction of remnants the mass-loss level which is needed for the AGB scenario varies but it needs to be at least $\sim 40\%$. Note that this mass-loss is dynamical mass-loss and not the mass which is lost due to stellar evolution.

As a result one can conclude that in contrast to the FRMS scenario, a top-heavy IMF is a problem for the AGB scenario as it leads to high M/L ratios inconsistent with observations.
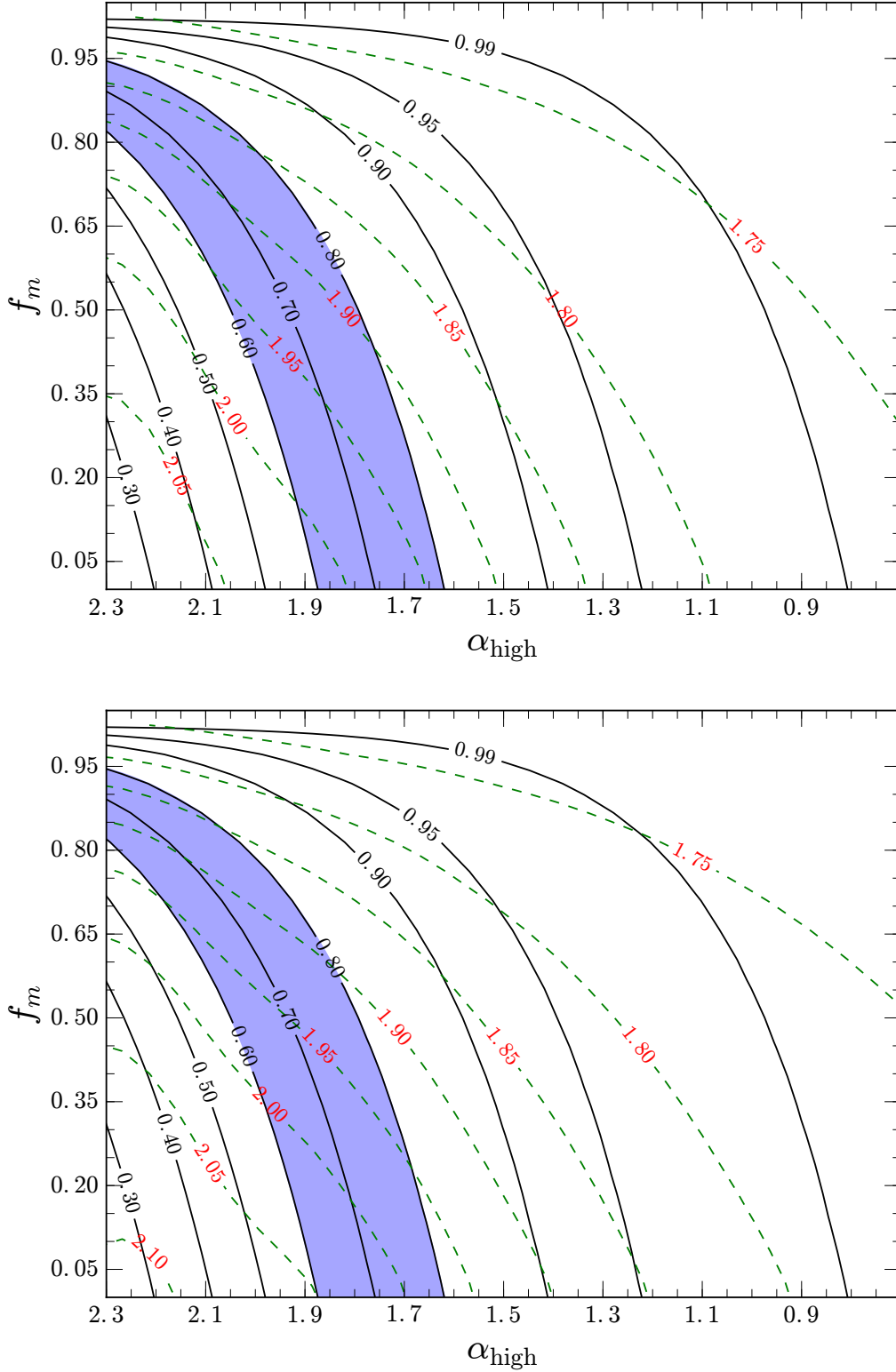
Figure 3.2: The contour maps of number ratio of SG stars (solid black lines) and M/L ratio (dashed green lines) of the cluster at $T = 12\,\mathrm{Gyr}$ for the FRMS scenario as a function of the high-mass slope α_{high} and FG mass-loss f_m. The blue shaded area shows an SG fraction of $70\% \pm 10\%$. The top and bottom corresponds to a dark remnant (black holes and neutron stars) retention fraction of $f_{\mathrm{ret0}} = 15\%$ and $f_{\mathrm{ret0}} = 30\%$ respectively, both with $\kappa = 1.0$.
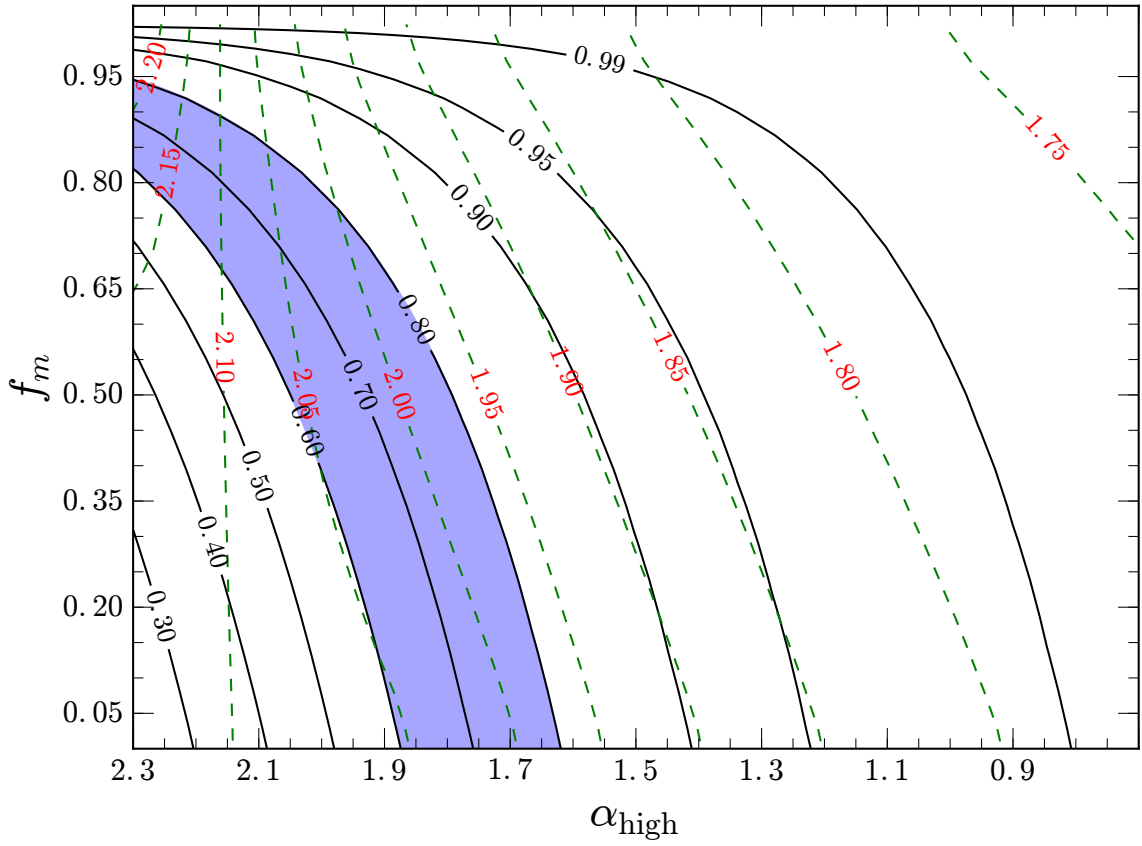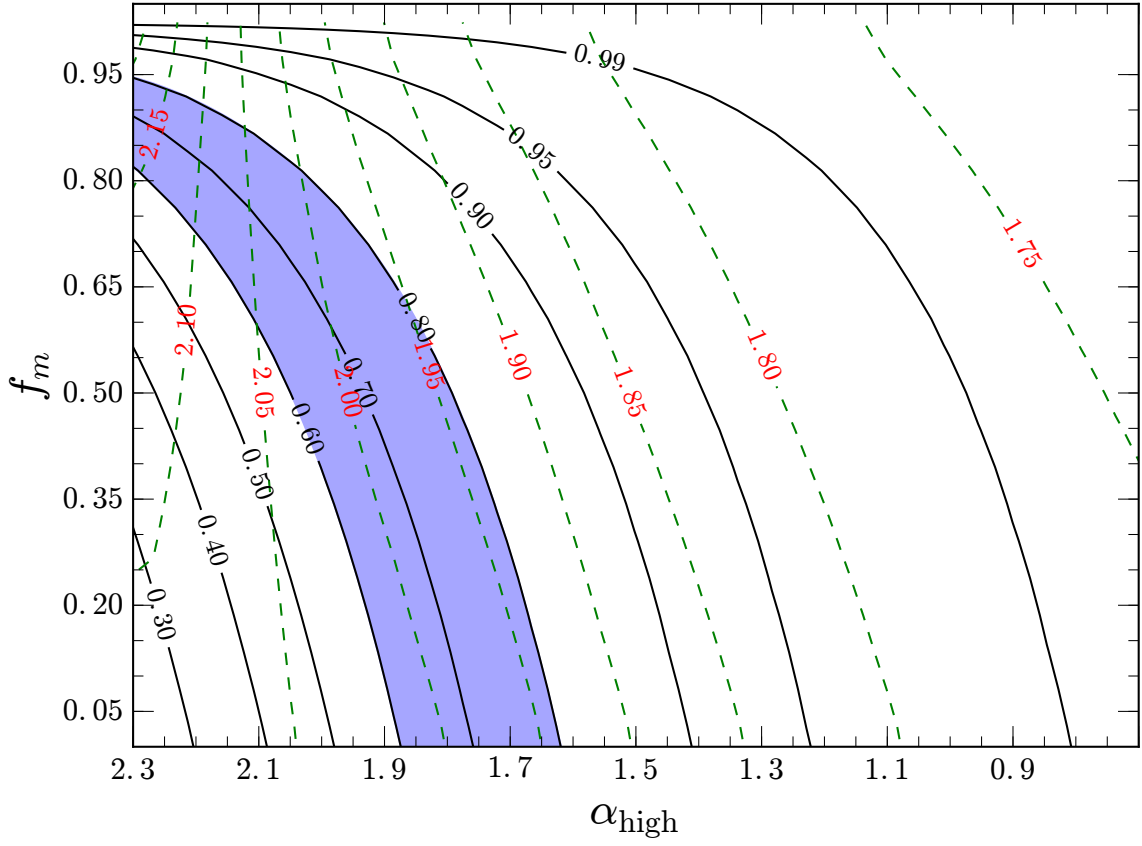
Figure 3.3: Same as Figure 3.2 but for $\kappa = 0.75$.
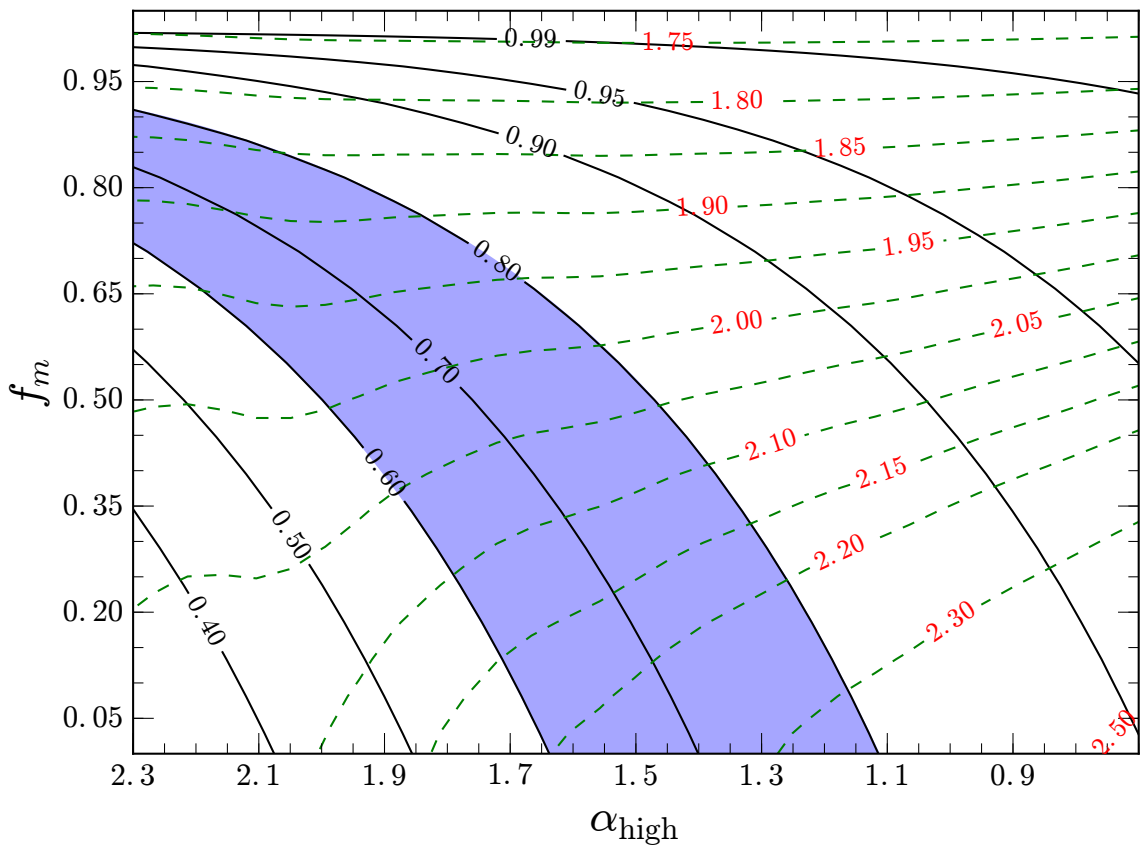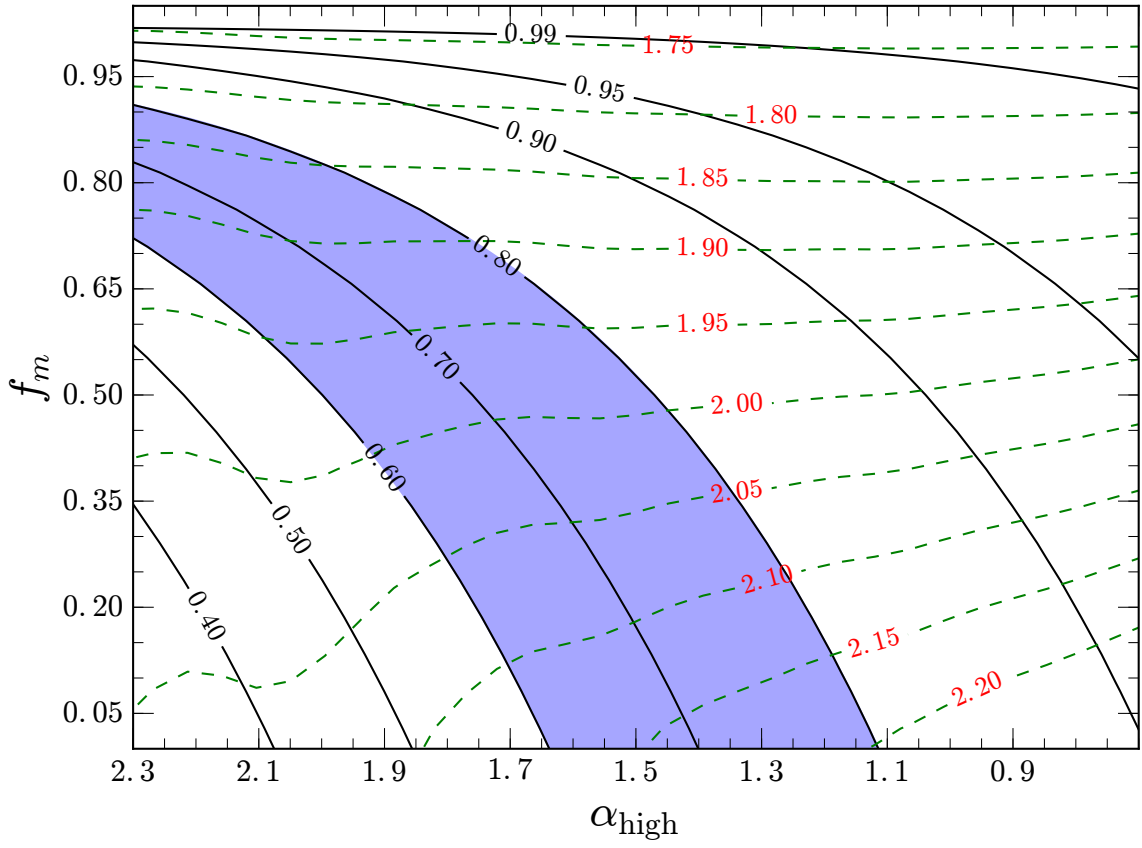
Figure 3.4: Same as Figure 3.2 but for the AGB scenario.
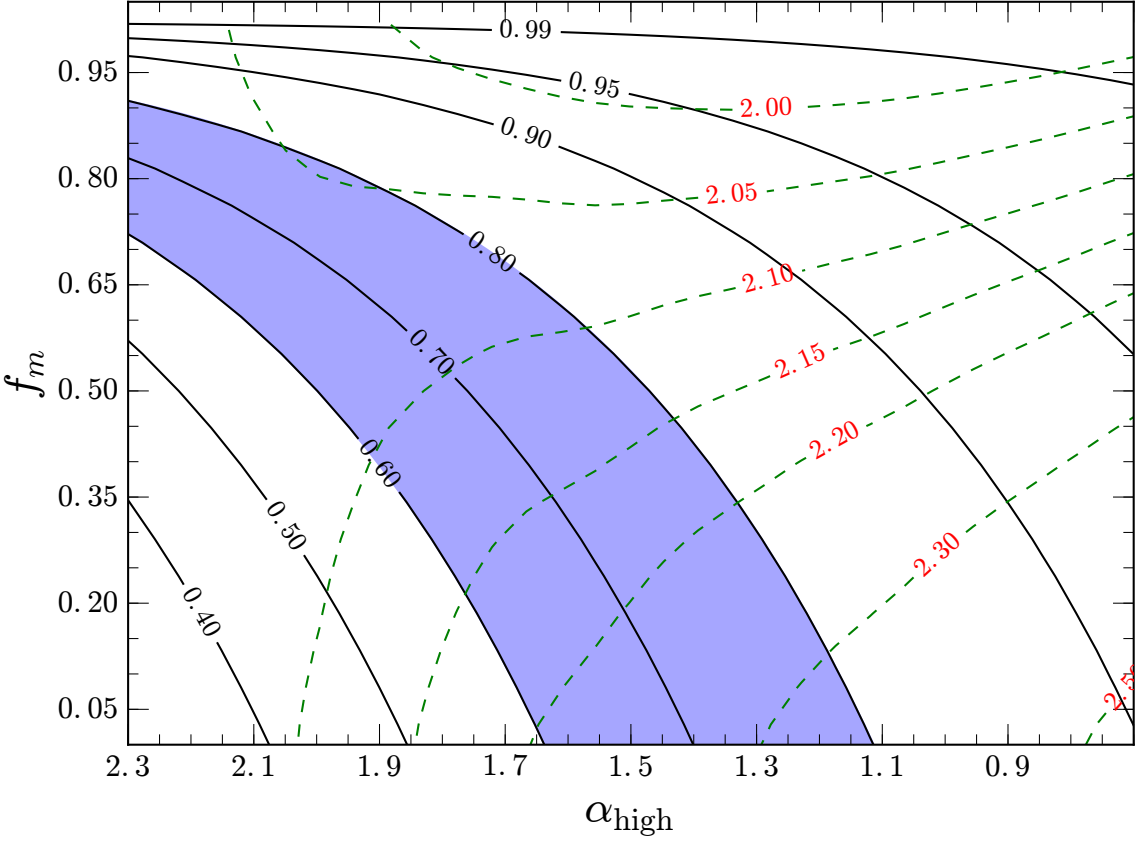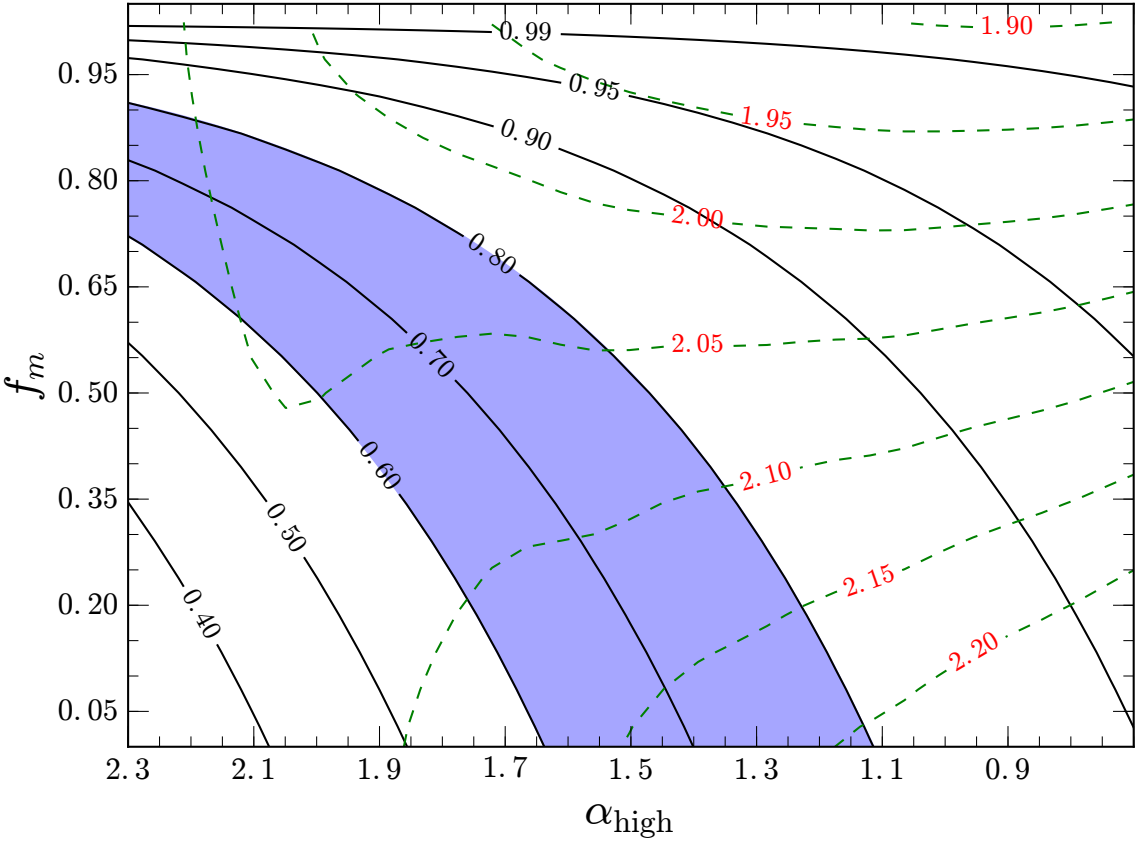
Figure 3.5: Same as Figure 3.3 but for the AGB scenario.

3.1.1 The role of dynamical evolution

In our simulations we have not considered the effect of dynamical evolution on the M/L ratios of GCs. In order to account for the effect of the dynamical evolution properly, one needs to make a grid of N-body simulations of GCs with MSPs assuming different α_{high} values for the IMF[2] and considering different helium abundances for SG stars, as well as alpha-enhancement in GCs. Such a grid is not available at the moment in the literature. Therefore, it is not possible to quantify the effect of dynamical evolution on the observed M/L ratios of GCs with MSPs. Nevertheless, one can use the grid of Baumgardt & Makino (2003) to estimate the effect of dynamical evolution qualitatively. Baumgardt & Makino (2003) performed a series of N-body simulations of multi-mass GCs in external tidal fields. They adopted a canonical IMF for their model clusters assuming that GCs are comprised of a SSP with normal abundances (no alpha-enhancement). They showed that M/L decreases as a result of dynamical evolution. This is due to the fact that the light (V-band) in a GC mainly comes from evolved stars which are the most massive stars in a GC and have a faster evolution rate, whereas much of the cluster mass comes from low-mass stars (Shanahan & Gieles, 2015). As the cluster ages, it goes toward equipartition and becomes mass segregated, i.e. more massive stars sink towards the core of the cluster and low-mass stars tend to move to the outskirt of the cluster[3] and leave the cluster. This will lead to a decrease in the cluster mass and consequently the M/L ratio of the cluster. According to Fig. 14 of Baumgardt & Makino (2003) the effect of dynamical evolution on M/L ratios becomes important only for clusters in strong tidal fields and in advanced evolutionary phases, i.e clusters which have lost 70 per cent or more of their mass have $|\Delta(M/L)| > 0.3$. As a result dynamical evolution only affects the upper part of figures 3.2 to 3.5 where the FG mass-loss is high ($f_m > 0.7$) and for other clusters the constraints that we obtained for α_{high} do not change significantly.

With the aid of dynamical evolution, the top-heavy IMF solution is completely compatible with the observed M/L ratios of Galactic GCs (*cf.* Hasani Zonoozi et al. 2016) for the FRMS scenario for any degree of mass-loss as long as the dark remnant retention fraction is low, and for the AGB scenario if the mass-loss is more than 40 per cent.

---

[2]considering its possible dependence on the metallicity (Marks et al., 2012)

[3]This kind of mass segregation is different from primordial mass segregation observed in young clusters (e.g. Hillenbrand & Hartmann 1998; de Grijs et al. 2002a,b; Gouliermis et al. 2004; Parker et al. 2016).

3.2 The effect of helium-enhancement on the observed number ratio of SG stars

Apart from a top-heavy IMF and significant mass-loss, there is also another factor which might loosen the constraints that we derived in the previous section or provide a solution to the mass budget problem. In all the scenarios of the formation of MSPs, SG stars have a higher helium abundance compared to FG stars which have $Y_{\text{initial}} \sim 0.25$ (Decressin et al., 2007a). This is due to the fact that helium is the direct product of hydrogen burning in FG stars and SG stars are formed out of their ejecta. Hence they are supposed to be enriched (enhanced) in helium. Stars with different helium abundances evolve differently. In particular, a star with higher helium abundance has a shorter main-sequence lifetime. Meaning that they enter the giant branch phase earlier than stars with the same mass but a lower helium abundance. In addition, assuming that the mass function increases towards the lower masses (which is the case for both Kroupa (2001) and Chabrier (2003) IMFs), this can result in a boost in the observed ratio of the evolved SG to FG stars (e.g. stars in the giant or horizontal branch). To justify this claim mathematically, let $\xi_1(m)$ and $\xi_2(m)$ represent the normalized IMF of the long-lived FG and SG stars respectively, i.e.

$$\int_{m_{\min}}^{m_{\max}} \xi_i(m)\, dm = N_i \quad , \quad i \in \{1, 2\}$$

where N_1 and N_2 is the number of the long-lived FG and SG stars, i.e. stars with $m \lesssim 0.8$ which are still alive today after $T \sim 10\,\text{Gyr}$. In addition, suppose that $\xi_1(m)$ and $\xi_2(m)$ have the same mathematical form and differ only by a normalization constant which is essentially the ratio of N_2/N_1, i.e.

$$\xi_1 \propto \xi_2 \rightarrow \frac{\xi_2(m)}{\xi_1(m)} = \frac{N_2}{N_1}, \quad n_0 \equiv \frac{N_2}{N_1} \tag{3.6}$$

which holds for every m. At some time $t > 0$ during the evolution of a GC with MSPs, FG stars with mass m_{TO_1} reach their turnoff point, whereas at the same time SG stars with $m_{\text{TO}_2} < m_{\text{TO}_1}$ are reaching the turnoff point, owing to their higher helium abundance. The ratio of all evolved SG to FG stars (denoted by n_{TO}) is

$$n_{\text{TO}} = \frac{\displaystyle\int_{m > m_{\text{TO}_2}} \xi_2(m)\, dm}{\displaystyle\int_{m > m_{\text{TO}_1}} \xi_1(m)\, dm} \tag{3.7}$$

Since the IMFs are monotonically increasing toward lower masses one can conclude that $\xi_1(m_{\mathrm{TO}_1}) < \xi_1(m_{\mathrm{TO}_2})$ and $\xi_2(m_{\mathrm{TO}_1}) < \xi_2(m_{\mathrm{TO}_2})$. Hence from equations 3.6 and 3.7 we have

$$n_{\mathrm{TO}} = \frac{\int_{m>m_{\mathrm{TO}_2}} \xi_2(m)\,dm}{\int_{m>m_{\mathrm{TO}_1}} \xi_1(m)\,dm} > \frac{\int_{m>m_{\mathrm{TO}_1}} \xi_2(m)\,dm}{\int_{m>m_{\mathrm{TO}_1}} \xi_1(m)\,dm} = n_0 \quad , \quad f_{\mathrm{boost}} = \frac{n_{\mathrm{TO}}}{n_0} > 1 \qquad (3.8)$$

where f_{boost} is what we refer to as the boosting factor. In reality there is a distribution of helium abundances for SG stars (Chantereau et al., 2016) which leads to a distribution for f_{boost} as a function of Y. As a result one needs to integrate over all the values of Y to calculate the value of f_{boost} which will still be larger than unity for all evolved stars. Note that we proved $f_{\mathrm{boost}} > 1$ for any IMF which is increasing toward lower masses, so it is not specific to Kroupa (2001) or Chabrier (2003) IMFs. However, we stress that in our derivation we have considered all evolved stars (i.e. no magnitude cut). In this case only the main-sequence lifetime matters. If we introduce a magnitude cut and calculate f_{boost} for only red-giant branch (RGB) or horizontal-branch (HB) stars, we might get different results as the lifetime of stars on these evolutionary phases also matter. In other words, stars with higher helium abundances have shorter lifetimes not only on the main-sequence but also on the RGB and HB which works against the boosting. This can cause f_{boost} to be even less than unity. The exact value of f_{boost} depends on the assumed mass function and helium distribution of stars.

Since in general f_{boost} is not equal to unity, the measured ratio of evolved SG to FG stars is different than the initial ratio of SG to FG stars. This is very important for the studies which deduce the initial number ratio of SG to FG stars based on the observations of evolved stars. If the boosting factor is significantly larger than unity (e.g. ~ 10) then it implies that we can initially start with a much lower number of SG stars in the GCs than what we observe today in the giant or horizontal branch and the mass-budget problem will be resolved this way.

To examine how large f_{boost} is we evolved models of GCs with two populations of stars both with a Kroupa (2001) IMF. We assumed that the lower and upper limit of the IMF are 0.1 and 1.0 respectively. For stellar evolution we used the grid of stellar models of Chantereau et al. (2015)[4]. Using the STAREVOL (Siess et al., 2000; Palacios et al., 2006; Lagarde et al., 2012) code they calculated a grid of helium-enhanced stellar models for stars with $[\alpha/\mathrm{Fe}] = +0.3$ and $[\mathrm{Fe}/\mathrm{H}] = -1.75$. In their models They varied the helium abundance from 0.248 to 0.8. Today's

---

[4]The data can be downloaded from http://obswww.unige.ch/Recherche/evol/starevol/Globular.php
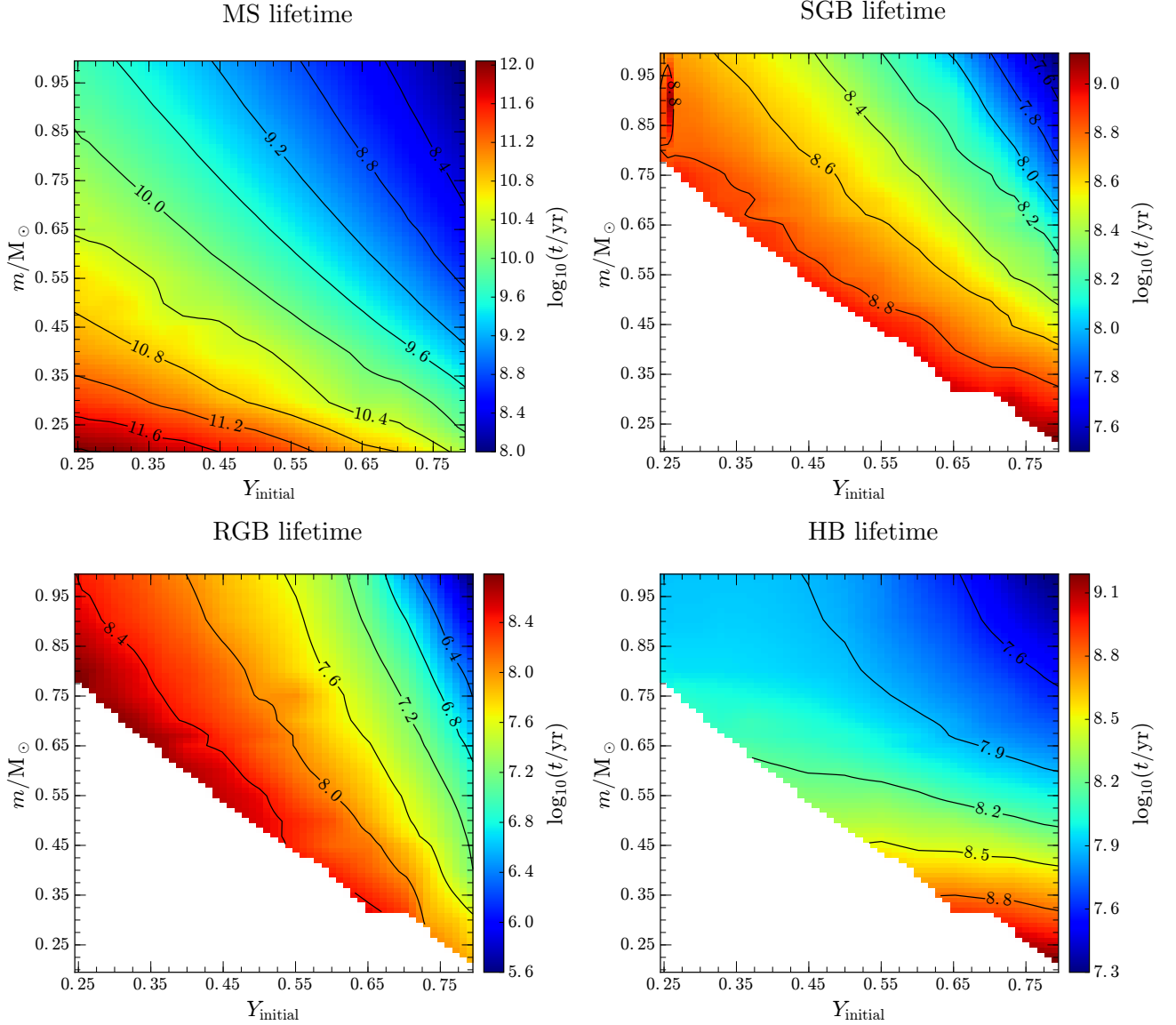
Figure 3.6: Lifetime of stars with different masses and helium abundances, in different phases of their evolution. The white filled area in the lower left corner of plots corresponds to stars with a main-sequence (MS) lifetime of more than a Hubble time. Hence they are excluded from the grid. Data taken from Chantereau et al. (2015).

helium abundance of MSPs are expected to be mainly below 0.4 (e.g. Charbonnel et al. 2013), however, there could be stars in GCs which formed with a higher helium abundance ~ 0.8 (FRMS scenario; Decressin et al. 2007b) but have already been turned into white dwarfs as their main-sequence lifetime is short, e.g. $T = 100\,\mathrm{Myr}$ for $1\,\mathrm{M_\odot}$ star. This justifies why such stars with high helium abundances also need to be considered in this study.

The lifetime of stars with different masses and helium abundances, in different phases of their evolution is shown in Figure 3.6. The general trend in the figure is that the lifetime of stars at

each evolutionary phase decreases as the mass or helium abundance increases. For example, a $0.5\,\mathrm{M_\odot}$ star with a normal helium abundance has a main-sequence lifetime of $\sim 63\,\mathrm{Gyr}$, whereas a similar star with a helium abundance of $Y = 0.55$ has a main-sequence lifetime which is 6 times less. The white filled area in the SGB, RGB and HB subplots of Figure 3.6 correspond to those stars which do not leave the main sequence after a Hubble time and therefore are not considered in our study.

In our models, we consider that all FG stars have a normal helium abundance and SG stars have a distribution of helium abundances which is Gaussian and characterized by a mean (μ_{He}) and a width (σ_{He}). We simulate 10^6 stars for every population of stars, evolve the cluster for $T = 10\,\mathrm{Gyr}$ and calculate the boosting factor f_{boost}. Note that the initial number ratio of SG to FG stars is not important as we are only interested in the boosting factor and not the actual ratios.

Figure 3.7 illustrates the boosting factor for different stages of stellar evolution. As one can see, the boosting is more pronounced on the HB, whereas the RGB shows almost no boosting in the observed ratio of SG stars. The reason that RGB and HB have the smallest and largest boosting factors can be explained by inspecting Figure 3.6 which shows that the HB lifetime has a minor dependency on the helium abundance compared to the RGB which has the highest dependency on the helium abundance. The stars with higher helium abundances evolve faster and enter the SGB and RGB phases faster than their FG counterparts but they also leave these phases faster. As a result they enter and leave these phases with roughly the same rates leaving the observed number ratio of SG stars almost unchanged on the SGB and RGB. However, SG stars enter the HB phase with a higher rate than they leave due to the lesser dependence of HB lifetime on helium abundance compared to the SGB or RGB.

According to these results, we can conclude that the overall effect of helium enhancement for all evolved stars in conjunction with an IMF that increases toward lower masses cannot boost the observed number ratio significantly. More specifically, at $T = 10\,\mathrm{Gyr}$, the value of f_{boost} for all evolved stars is close to unity for moderate values of helium abundance (i.e. $Y \sim 0.35$), implying that the observed number ratio of evolved SG to FG stars is close to their actual number ratio. Our results for all evolved stars are in agreement with Chantereau et al. (2016) who did a similar analysis and found that the fraction of main-sequence stars with $Y > 0.35$ drops from 33% at $T = 0\,\mathrm{Gyr}$ to 25% at $T = 9\,\mathrm{Gyr}$. Since the fraction of helium enhanced stars decreases on the main-sequence, this implies a larger than unity boosting for all evolved stars. On the RGB or HB,

SGB

RGB

HB

all evolved stars
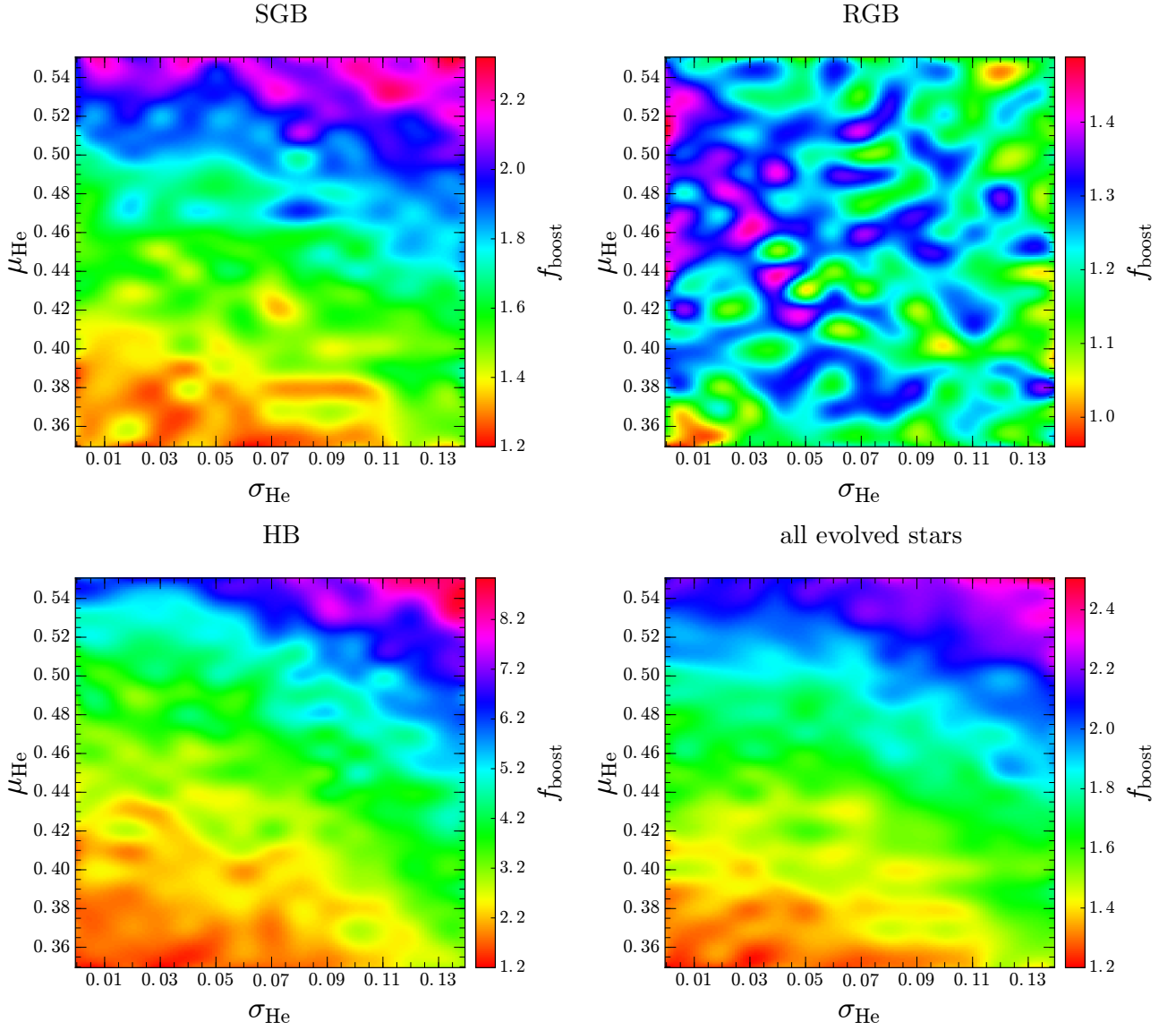
Figure 3.7: Boosting factor (f_{boost}) as a function of the mean and the width of the helium distribution of SG stars.

our results cannot be directly compared with those of Chantereau et al. (2016) as they assume a different IMF and a different helium distribution of SG stars compared to what we assumed in this study.

3.3 Summary

We studied two viable solutions to the mass-budget problem in GCs with MSPs, i.e. a top-heavy IMF and significant mass-loss from FG stars. Using synthetic models of GCs with two stellar populations, we derived the range of high-mass slopes and mass-loss levels for the AGB and the

FRMS scenario which lead to the observed fraction of SG stars and M/L ratios of Galactic GCs. We assumed different retention fractions for white dwarfs and dark remnants.

We showed that without any mass-loss the high-mass slope for the FRMS and AGB scenario needs to be $\alpha_{\mathrm{high}} = 1.75 \pm 0.15$ and $\alpha_{\mathrm{high}} = 1.40 \pm 0.30$ respectively to explain the observed fraction of SG stars. Moreover, if the IMF is canonical the FG mass-loss needs to be $f_m = 0.85 \pm 0.05$ and $f_m = 0.90 \pm 0.05$ for the AGB and the FRMS scenario respectively. The error bars have been determined by calculating the scatter (σ) which exists in the observed fraction of SG stars for Galactic GCs with MSPs, i.e. the shaded area in figures 3.2 to 3.5. If FG polluters are FRMS then the derived M/L ratio of MSPs for a top-heavy IMF are consistent with Galactic GCs. However for the AGB scenario, top-heavy IMF needs to be accompanied by some level of mass-loss ($f_m > 40\%$) of FG stars. In our models we neglected the effect of dynamical evolution on the observed M/L ratios of GCs. In spite of this, we showed that our results are valid as long as the mass-loss from the cluster is $f_m < 70\%$.

Finally, we studied the effect of helium enhancement on the observed number ratio of evolved SG to FG stars and how it is related to the actual number ratio of SG to FG stars. Overall, we found that helium enhancement cannot boost the observed number ratio significantly for all evolved stars. The actual amount by which the observed ratio of SG to FG stars can be boosted depends on their formation scenario. In the AGB scenario, it is expected that SG stars all have similar helium abundances of $Y < 0.4$, whereas for the FRMS scenario the helium abundance of SG stars can extend to $Y \sim 0.8$ (Decressin et al., 2007a; Chantereau et al., 2015). This translates into a maximum boosting factor of about $f_{\mathrm{boost}} = 1.4$ and $f_{\mathrm{boost}} = 2.5$ for all evolved stars in the AGB and the FRMS scenarios respectively. In either case, these boosting factors are not sufficient to fully resolve the mass-budget problem, however they need to be taken into account when one wants to constrain the formation mechanism of MSPs based on their observed number ratio. In particular, one needs to correct the observed ratio of SG stars using the obtained values for f_{boost} to infer the actual number ratio of SG stars.

4

N-body simulations and dynamical constraints on significant mass-loss in GCs with MSPs

In this chapter[1] we study the effect of significant mass-loss on the dynamical evolution of star clusters with MSPs. Using N-body simulations we determine the required initial conditions under which the final number of SG to FG stars match the observations. We then perform an MC analysis to compare the outcome of our simulations with observations and determine whether the significant mass-loss scenario is able to explain the observed mass and half-mass radius distributions of GCs and ultimately be the reason for the observed abundance anomalies.

The chapter is structured as follows. In the next section we briefly review the mass-loss mechanisms which can affect the dynamical evolution of GCs. We discuss the details of our N-body simulations and the procedures we have followed to create our grid of runs in Section 4.2. In Section 4.3 we present our results and then compare the outcome of simulations with observations using an MC analysis in Section 4.4. We finally summarize the main results in Section 4.5.

4.1   Mass-loss mechanisms

There are several mechanisms through which a star cluster can lose mass: stellar evolution induced mass-loss, two-body relaxation, external tidal shocks and primordial gas loss. These mechanisms are discussed further below.

---

[1]This chapter is based on Khalaj & Baumgardt (2015) and the published version is available at `http://dx.doi.org/10.1093/mnras/stv1356`

4.1.1   Stellar evolution induced mass-loss

In the early phases of the formation and evolution of a cluster, clusters lose mass via stellar evolution, i.e. high-mass stars which have a faster evolution rate lose mass via stellar ejecta/winds which can leave the cluster. However, mass-loss as a result of stellar evolution is not limited to this and stellar evolution has a dynamical effect on the cluster as well. In particular, stellar evolution leads to the loss of gravitational potential in the cluster to which the cluster responds by expansion, i.e. stars go to further distances from the cluster centre where they can be stripped by external tidal field and become unbound. Moreover, the resulting compact remnants such as neutron stars and black holes can get a natal kick which can be larger than the escape speed of the cluster. These effects, which contribute to the overall mass-loss of the cluster and can be attributed to stellar evolution, are known as the stellar evolution induced mass-loss which is different from relaxation-driven mass-loss (see Section 4.1.2). The amount of stellar evolution induced mass-loss depends on the initial conditions of the cluster, e.g. IMF, metallicity and the compactness of the cluster (Lamers et al., 2010) as well as the environment (e.g. the orbit of the cluster around its host galaxy). Vesperini et al. (2009) studied the effect of stellar evolution induced mass-loss on clusters with initial mass segregation. They showed that for initially mass-segregated GCs which are filling their Roche lobes (i.e tidally truncated), stellar evolution causes a strong expansion in the cluster which consequently leads to higher mass-loss rates and shorter dissolution times compared to unsegregated clusters. In contrast, mass-segregated GCs which are initially underfilling their Roche lobes, have dissolution times comparable to unsegregated clusters. Lamers et al. (2010) studied the effect of stellar evolution on the mass-loss of GCs using *N*-body simulations. They considered different King (1966) models for their clusters and placed them in elliptical orbits with different eccentricities in the Galaxy. They assumed a Kroupa (2001) IMF for their model clusters without initial mass segregation or primordial binaries, but binaries could form later on in the simulation. They showed for a cluster whose lifetime is larger than $20\,\mathrm{Gyr}$ (initial mass of $\sim 10^6\,\mathrm{M_\odot}$), stellar evolution induced mass-loss can account for only $15\,\mathrm{per\,cent}$ of the total mass-loss, whereas for clusters with shorter lifetimes ($< 5\,\mathrm{Gyr}$) this amount is about $\sim 10\,\mathrm{per\,cent}$. Both of these values are well below the required limit (of $\sim 90\,\mathrm{per\,cent}$ or more) for the significant mass-loss scenario. For the rest of the thesis our focus will be on stellar evolution induced mass-loss in the context of MSPs. For an estimation of expected mass-loss due to stellar evolution for FG and SG stars and their mass ranges refer to Section 4.4.

To lose a large amount of mass via stellar evolution, clusters need to be very extended and in

a strong tidal field where the ratio of the tidal radius to the half-mass radius, r_t/r_h, is small. The effect of stellar evolution induced mass-loss in the AGB scenario has been studied by D'Ercole et al. (2008) using a series of N-body simulations. In their models, they use King (1966) models with $M_{FG} = 10^7\,M_\odot$, $r_t = 200\,pc$ and $W_0 = 7.0$, $c = \log(r_t/r_c) = 1.50$, where SG stars are highly concentrated in the innermost regions of the clusters with a half-mass radius one-tenth of that of the initial FG stars. Such initial parameters correspond to very extended clusters ($r_t/r_h = 8.75$ and $r_h = 23\,pc$) in which SG and FG stars are dynamically decoupled from each other. As a result FG stars can readily expand their orbits and be stripped by the Galactic tidal field in response to a small amount of mass-loss, leaving a sub-cluster of SG stars in the center of the initial cluster. D'Ercole et al. (2008) also study other models with different initial truncation radii and concentrations which underfill their Roche lobes, but the only models that match the observed number ratio of SG to FG stars, i.e. $N_2/N_1 \sim 1.0$, are the very extended and tidally filling clusters. This is not in agreement with the observation of young massive star clusters and today's properties of GCs as they have typical half-mass radii of around $1.0\,pc$ (Portegies Zwart et al., 2010) and $5.0\,pc$ respectively (Harris, 1996). Unless the condition under which GCs have formed were significantly different, the stellar evolution induced mass-loss cannot lead to significant mass-loss. In addition, it is unclear if a sample of clusters with these initial conditions can explain the observed distribution of SG number ratios in GCs.

4.1.2 Two-body relaxation

Baumgardt & Makino (2003) studied the effect of two-body relaxation as well as stellar evolution on the dynamical evolution of star clusters in external tidal fields through N-body simulations. They assumed different Galactic orbits, stellar density profiles and particle numbers for star clusters and derive the following formula for the lifetime of a star cluster

$$\frac{T_{diss}}{Myr} = \beta \left[\frac{N}{\ln(0.02N)} \right]^x \frac{R_G}{kpc} \left(\frac{V_G}{220\,km\,s^{-1}} \right)^{-1} (1 - e) \qquad (4.1)$$

where N is the number of particles, V_G and R_G are the Galactic circular velocity and distance of the cluster and e is the eccentricity of the cluster orbit. x and β are two parameters whose values depend on the initial concentration of the cluster and for King $W_0 = 7.0$ they are equal to 0.82 and 1.03 respectively.

For $N = 10^6$, $e = 0.5$, $V_G = 220\,km\,s^{-1}$ and $R_G = 8.5\,kpc$, T_{diss} will be about $55\,Gyr$ which

shows that two-body relaxation is a slow process for massive GCs and is not efficient in reducing the mass of GCs by 90 per cent over one Hubble time. As a result this process cannot be the origin of significant mass-loss in star clusters and we will omit this process in our N-body simulations.

For a cluster whose initial number ratio of SG to FG stars is ~ 10 per cent and SG stars are more concentrated than FG stars, two-body relaxation causes different stellar populations to fully mix in about 2 elapsed half-mass relaxation times (Decressin et al., 2008). Using equation 1 of their paper, a cluster with $M = 10^6\,\mathrm{M_\odot}$ and $r_\mathrm{h} = 3\,\mathrm{pc}$, has a mixing time of approximately $2\,\mathrm{Gyr}$. This implies that any significant mass-loss scenario proposed to explain the origin of MSPs must have a shorter time-scale, since after the mixing has occurred the number ratio of SG to FG stars will not change due to further mass loss. However, If the average masses of FG and SG populations are markedly different, their relative ratio can still change.

4.1.3   External tidal shocks

External tidal shocks such as encounters with giant molecular cloud (GMC) are able to disrupt open cluster (OC) $M \leq 10^4\,\mathrm{M_\odot}$ via a single encounter on time-scales of about $\sim 2.0\,\mathrm{Gyr}$ (Wielen, 1985; Gieles et al., 2006). Gieles et al. (2006) derived the following formula for the disruption time of star clusters

$$\mathrm{T_{dis}} = 2.0 \left(\frac{5.1\,\mathrm{M_\odot^2\,pc^{-5}}}{\Sigma_n \rho_n} \right) \left(\frac{M_\mathrm{c}}{10^4\,\mathrm{M_\odot}} \right)^{0.61} \mathrm{Gyr}$$

where Σ_n and ρ_n are the individual surface and global density of the GMCs, equal to $170\,\mathrm{M_\odot\,pc^{-2}}$ and $0.03\,\mathrm{M_\odot\,pc^{-3}}$ in the solar neighbourhood (Solomon et al., 1987). For a globular cluster (GC) with $M_\mathrm{c} = 10^6\,\mathrm{M_\odot}$, this formula gives a disruption time of almost $\sim 33\,\mathrm{Gyr}$. In denser environments such as the center of M51, ρ_n is 10 times higher (Gieles et al., 2006) which shortens the disruption time by an order of magnitude, but this is still larger than the mixing time of MSPs ($\sim 2\,\mathrm{Gyr}$), as discussed in Section 4.1.2. In addition encounters with GMCs are stochastic by nature. Hence they cannot be responsible for significant mass-loss in all clusters and their effect is insignificant over short time-scales.

In addition to GMCs, external tidal shocks can also happen due to the effect of bulge, the Galactic disc and the Galactic bar (Gnedin & Ostriker, 1997; Gnedin et al., 1999; Moreno et al., 2014). In general, they increase the mass-loss rate of GCs. This depends on the cluster half-mass radius which implies that the dissolution time of the cluster scales with its density (Lamers et al., 2010). The effect of bulge shocks on the lifetime of clusters is included in equation (4.1) via the

eccentricity e. Vesperini & Heggie (1997) studied the effect of disc shocks on the mass-loss and the mass function of GCs. They found that the difference in the mass-loss of GCs affected by disc shocks and those which are not (i.e. $\Delta M_{ds}/M_i$) is not significant for most GCs. More precisely, according to Vesperini & Heggie (1997) (table 2 therein), $\Delta M_{ds}/M_i$ is about $\sim 10\%$ for GCs with Galactocentric radii (R_G) between $1-5\,\mathrm{kpc}$ and it is less than 5% for $R_G \gtrsim 8\,\mathrm{kpc}$ (Solar distance). The Galactic bar also plays a role in the destruction of GCs, especially for those GCs which cross the inner radii of the Galaxy. However, Moreno et al. (2014) showed that the destruction rates of clusters in a barred galaxy like the Milky Way (nonaxisymmetric potential) are less than in an unbarred galaxy (axisymmetric potential). This is due to the fact that mass distributed in a bar has a less central concentration compared to a bulge.

4.1.4   Primordial gas loss

If the star formation efficiency is less than $100\,\mathrm{per\,cent}$, this process will happen to every cluster of any size or mass since it has an intrinsic origin. Any gas loss in GCs will be accompanied by loss of stars, especially when the gas loss is impulsive (Baumgardt & Kroupa, 2007). There are a number of different sources which can inject enough energy into the intra-cluster medium to entirely unbind the primordial gas. Examples are stellar winds, SN explosions (Decressin et al., 2010) and black holes (Krause et al., 2012, 2013).

With all other mass-loss scenarios excluded or shown to be ineffective on short time-scales, primordial gas loss remains as the only plausible and universal mechanism via which GCs can lose a significant amount of mass over a few Myrs and in our *N*-body simulations we only deal with such primordial gas loss as discussed in the next section. As mentioned above accretion onto dark remnants is one candidate for a mechanism which can cause such a primordial gas loss. The setup of our model clusters and our analysis, though consistent with the dark remnant scenario (Section 4.4), is not limited to this scenario and in principle can be applied to any other physical process that has a similar effect on GCs.

4.2   *N*-body simulations

We set up clusters consisting of 3 components: FG stars ($\sim 90\,\mathrm{per\,cent}$ of total stellar mass), SG stars ($\sim 10\,\mathrm{per\,cent}$) and a gas cloud whose mass is a free parameter in the simulations. The initial number ratio of SG to FG stars N_2/N_1 is fixed at 0.1. We do not directly simulate the gas particles

Table 4.1: Initial conditions of the simulations.

Parameter	Symbol	Value
Fixed parameters		
Total number of stars	N	20480
Initial number of SG to FG stars	N_2/N_1	0.1
Ratio of the Plummer scale radius of the gas cloud to SG stars	a_g/a_2	1.0
Variable parameters		
Ratio of the Plummer scale radius of SG stars to FG stars	$\lambda = a_2/a_1$	$\{0.1, 0.2\}$
Ratio of the Initial mass of the gas cloud to the mass of FG stars	$\eta = M_{\mathrm{g}}/M_1$	$0.0 \leq \eta \leq 2.0$
Ratio of the gas expulsion time-scale to the initial crossing time	$\tau = T_{\mathrm{exp}}/T_{\mathrm{cr}}$	$10^{-2} \leq \tau \leq 10^4$
Ratio of the initial tidal radius to the Plummer radius of FG stars	r_{t}/a_1	$\{5, 10, 15, 20, 25, 30, 35, 40, \infty\}$

but only calculate the force that the gas cloud exerts on each star. The initial density profiles of the different components are given by Plummer (1911) models with different masses and Plummer radii. We have used Plummer models since they are easy to work with and it is also possible to validate the outcome of the simulations using analytical methods. We do not expect that other initial density distributions such as King (1966) models will affect the final results significantly, as the exact details of any initial density distribution will be quickly wiped out by violent relaxation as a result of significant mass-loss in the simulated star clusters.

The central gas cloud and SG stars have the same degree of concentration with respect to FG stars in our simulations, i.e. $a_2/a_1 = a_g/a_1 \in \{0.1, 0.2\}$ where a_1, a_2 and a_g are the Plummer scale radii of FG stars, SG stars and the gas cloud respectively. Table 4.1 summarizes the initial conditions of our simulations.

The time-scale of our simulations is short compared to the clusters relaxation times so the effect of stellar evolution, mass segregation, two-body relaxation, etc. can be neglected. This is due to fact that we start the simulations when SG stars have already formed and are in place, i.e. the most massive stars from the FG population have already evolved and lost mass as a result of stellar evolution. Stellar evolution for the rest of stars which are less massive happen on a time-scale (Myr to Gyr) which is much longer than the time-scale of our simulations which are of the order of one crossing time or less ($10^4 - 10^5$ yr). Later in the chapter (Section 4.4) we consider the effect of stellar evolution induced mass-loss when converting the results of our simulations to physical units and find the best match with observations using MC analysis. As a result all particles in our simulations have equal masses which are constant throughout the whole

simulation. All time-scales in our simulations are expressed in terms of the initial crossing time of the cluster which is defined to be:

$$T_{\mathrm{cr}} \equiv \frac{2r_{\mathrm{h}}}{\sigma_v} \tag{4.2}$$

Where r_{h} is the initial half-mass radius of all stars (which is approximately equal to 1.20 times the Plummer radius of FG stars for the values adopted in Table 4.1, i.e. $r_{\mathrm{h}} \approx 1.20a_1$) and σ_v is the initial velocity dispersion of stars calculated from the virial theorem in the presence of gas.

We start with clusters which are initially in virial equilibrium and then remove the gas according to the following equation

$$M_{\mathrm{g}}(t) = \begin{cases} M_{\mathrm{g}}(0) \exp\left(-\dfrac{t-t_0}{\tau}\right) & t > t_0 \\ M_{\mathrm{g}}(0) & t \leq t_0 \end{cases} \tag{4.3}$$

where t is the simulation time, t_0 is the amount of time that we wait before removing the gas[2] and is set to be equal to 5 crossing times in all simulations and $\tau = T_{\mathrm{exp}}/T_{\mathrm{cr}}$ is the ratio of gas expulsion time-scale to the initial crossing time. We change τ in the range 10^{-2} to 10^4 on a logarithmic scale, corresponding to instantaneous and adiabatic gas expulsion respectively.

The initial mass of gas $M_{\mathrm{gas}}(0)$ is parameterized by a parameter η which is the ratio of the initial mass of gas divided by the initial mass of FG stars, i.e.

$$\eta = \frac{M_{\mathrm{g}}(0)}{M_1(0)} \tag{4.4}$$

where η varies from 0 to 2.00 in steps of 0.02 in our simulations.

All simulated clusters are in a Galactic tidal field which is modelled using the near-field approximation (Aarseth et al., 1993) and implemented by writing the equations of motions of stars in a right-handed rotating coordinate system whose origin is initially centered on the cluster and x and y axes point toward the Galactic anti-center and the direction of orbital motion of the star cluster respectively, assuming that the star cluster is moving in the $x-y$ plane. The equation of motion for a star in such a coordinate system is given by

$$\ddot{\mathbf{r}}_i(\text{total}) = \ddot{\mathbf{r}}_i(\text{stars}) + \ddot{\mathbf{r}}_i(\text{gas}) - 2\mathbf{\Omega} \times \dot{\mathbf{r}}_i + \Omega^2(3x_i\mathbf{e}_x - z_i\mathbf{e}_z) \tag{4.5}$$

---

[2]The reason that we don't remove gas at $t = 0$ is that we want to measure the dynamical properties of the simulated clusters in the first few crossing times when the cluster is still in equilibrium.

Where $\ddot{\mathbf{r}}_i(\text{stars}) + \ddot{\mathbf{r}}_i(\text{gas})$ is the acceleration of each star due to the total gravitational force of other stars and the gas cloud which are calculated using the following equations

$$\ddot{\mathbf{r}}_i(\text{stars}) = \sum_{j=1, j\neq i}^{j=N} \frac{Gm_j}{\left(|\mathbf{r}_j - \mathbf{r}_i|^2 + \epsilon^2\right)^{3/2}} (\mathbf{r}_j - \mathbf{r}_i) \tag{4.6}$$

$$\ddot{\mathbf{r}}_i(\text{gas}) = -\frac{GM_\text{g}(t)}{\left(r_i^2 + a_g^2\right)^{3/2}} \mathbf{r}_i \tag{4.7}$$

where ϵ is the softening parameter that we have introduced in our simulations and it is equal to the minimum distance between stars in the central region of the cluster. The motivation for the softening parameter ϵ in our N-body simulations is to avoid complications arising from binary formation and the singularity at $r = 0$ in the Newtonian $1/r$ potential for a point-mass. A comparison between equation (4.6) and equation (4.7) shows that by introducing ϵ into our simulations we actually approximate the gravitational potential of each particle with a Plummer profile whose scale radius is ϵ and asymptotically approximates the Newtonian potential for a point-mass. Moreover, since ϵ is nonzero, there will be no singularity at $r = 0$ for particles, i.e. it is guaranteed that the potential will be finite and its magnitude is less than a maximum value ($|U_\text{max}| = Gm_i/\epsilon$) at all times in our simulations which is beneficial to keep the integration and round-off errors minimal. The third and forth terms on the right-hand side of equation (4.5) are the Coriolis and centrifugal force combined with the tidal forces respectively and $\boldsymbol{\Omega} = \Omega\mathbf{e}_z$ is the angular velocity of the cluster around the Galactic center.

In our simulations the strength of tidal field is parameterized by the ratio of the tidal radius of each cluster to the Plummer radius of FG stars r_t/a_1. We vary r_t/a_1 from 5 to 40 in steps of 5, where a large value of r_t/a_1 means a weak tidal field. We also did one set of simulations for $r_\text{t}/a_1 = \infty$ ($\Omega = 0$) which corresponds to isolated clusters. r_t is related to the total cluster mass $M_\star(t) + M_\text{gas}(t)$ and Ω via the following equation (Giersz & Heggie, 1997):

$$r_\text{t}(t) = \left(G\frac{M_\star(t) + M_\text{g}(t)}{3\Omega^2}\right)^{1/3} \tag{4.8}$$

As a result, all clusters in our grid can be modelled by only 4 parameters η, r_t/a_1, τ and $\lambda = a_2/a_1$ (see Table 4.1). Our simulations can be thought of as a generalized version of the Baumgardt & Kroupa (2007) models who considered the effect of gas expulsion on a single stellar

population.

All simulations in our grid are run for 555 initial crossing times which was found to be enough for clusters with $\tau < 10^3$ to end up in a quasi-equilibrium state after which we determined the mass, half-mass radius and number ratio of SG stars. For $\tau > 10^3$ the gas expulsion is adiabatic which only affects the cluster in long term and is dealt with in Section 4.4.

We have used own developed code to perform the N-body simulations. To integrate the equations of motions for stars we have used the so-called Leapfrog integration scheme (see e.g. Hut et al. 1995) which is a second-order scheme, i.e. the global errors in the position and velocity are $\mathcal{O}(\Delta t^2)$. We use a constant time step in our simulations and we have ~ 700 steps per crossing-time. An important feature of Leapfrog is that it is a symplectic integrator meaning that the errors in the total energy are bounded and (a slightly modified) Hamiltonian for the system is conserved. As a result, the conservation of energy, which is highly important in our simulations, makes the Leapfrog scheme more favourable over non-symplectic integrators such as the 4th order Runge-Kutta in which the system has a tendency to drift from its initial energy state. In our simulations the total energy E is conserved to an accuracy of $\Delta E/E \sim 10^{-5}$. The details of how we determine the unbound stars in our simulations are given in the next section. We ran all the simulations on the Green II GPU supercomputer at Swinburne University of Technology.

4.3   Results

We record the properties of our model clusters throughout the simulation. In particular, we find unbound stars using an iterative algorithm as described below:

1. Find the coordinate of the cluster density center using the von Hoerner (1963) method and the unbiased density estimator of Casertano & Hut (1985) for the 10th nearest neighbours of each star, i.e. $j = 10$ in equation II.2 of Casertano & Hut (1985). We use the location of the density centre as the cluster centre which is widely used in N-body simulations (Heggie et al., 1994; Portegies Zwart et al., 2010). In addition, one can also use alternative methods to find the cluster center such as using the position of the minimum smoothed potential, known as the potential centre (Heggie & Ramamani, 1989) or fitting ellipses to the density distribution of the cluster, and averaging the centres of these ellipses (Goldsbury et al., 2010).
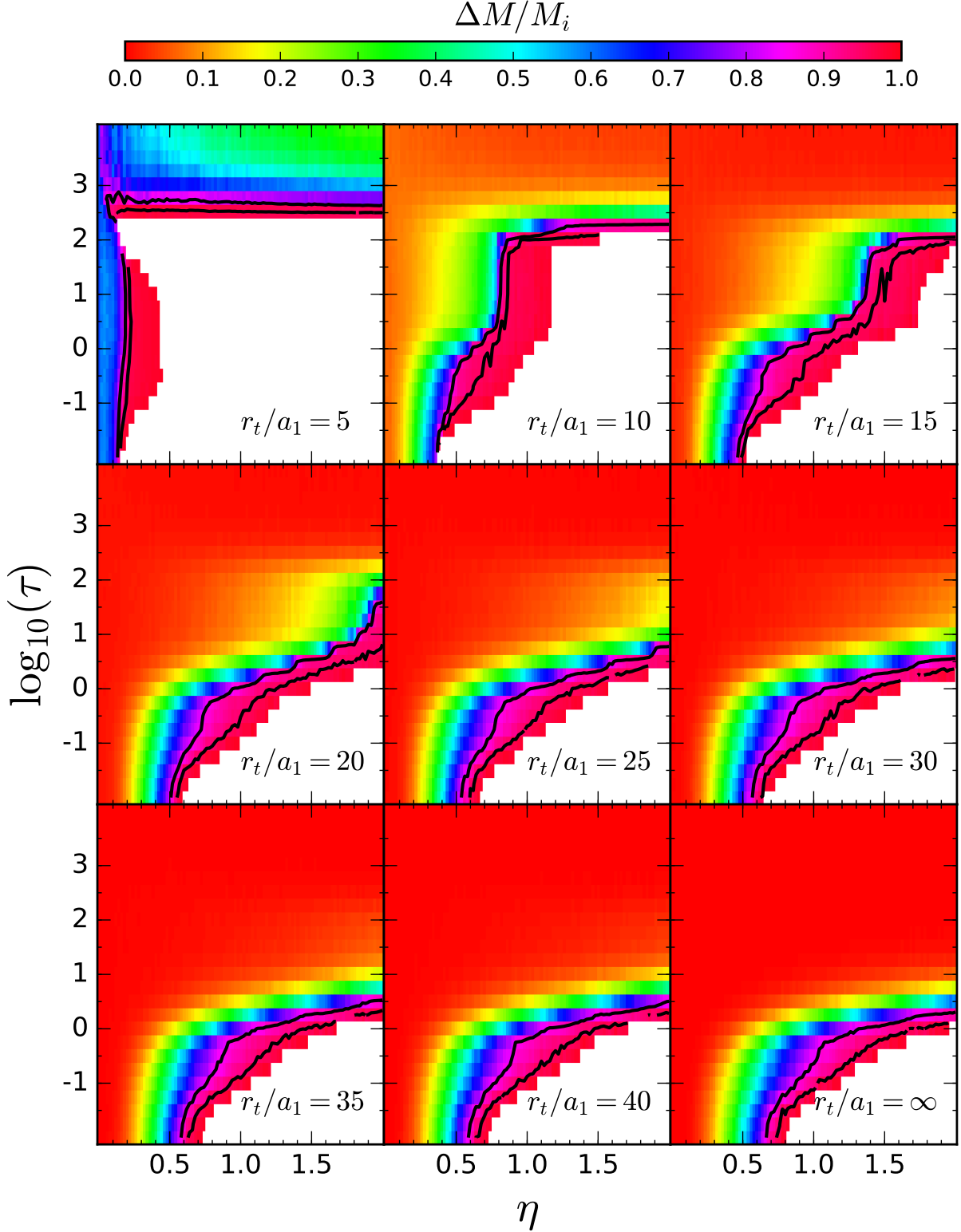
Figure 4.1a: Mass-loss $\Delta M/M_i$ as a function of gas fraction η and gas expulsion time-scale τ for different strengths of the tidal field ($r_t/a_1 = 5, 10, 15, 20, 25, 30, 35, 40, \infty$). This plot corresponds to $\lambda = 0.1$. The region enclosed by solid black lines corresponds to 90 ± 5 per cent mass-loss. The white filled area in the lower right corner of each plot shows the region where all clusters are totally destroyed.
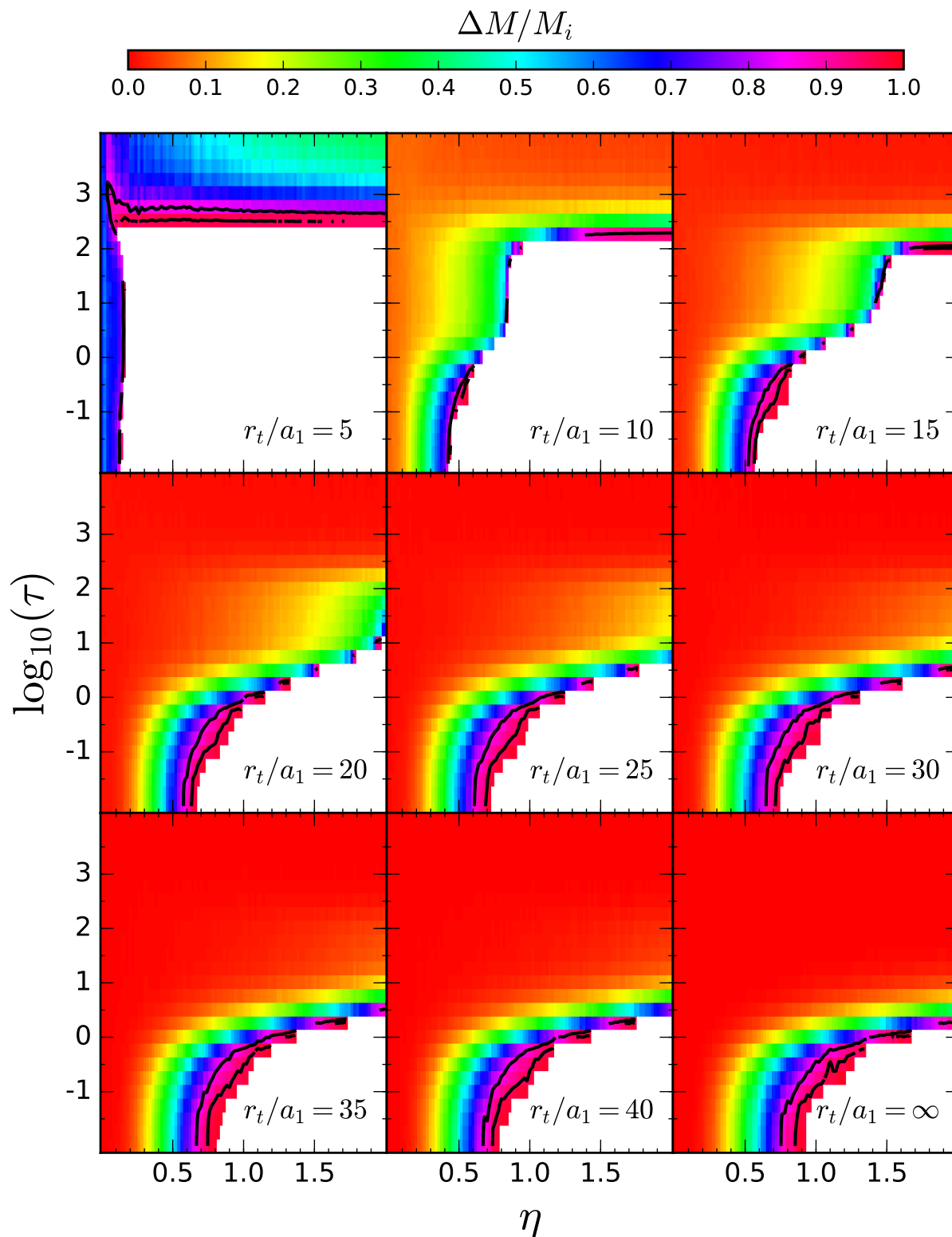
Figure 4.1b: Same as Figure 4.1a but for $\lambda = 0.2$.
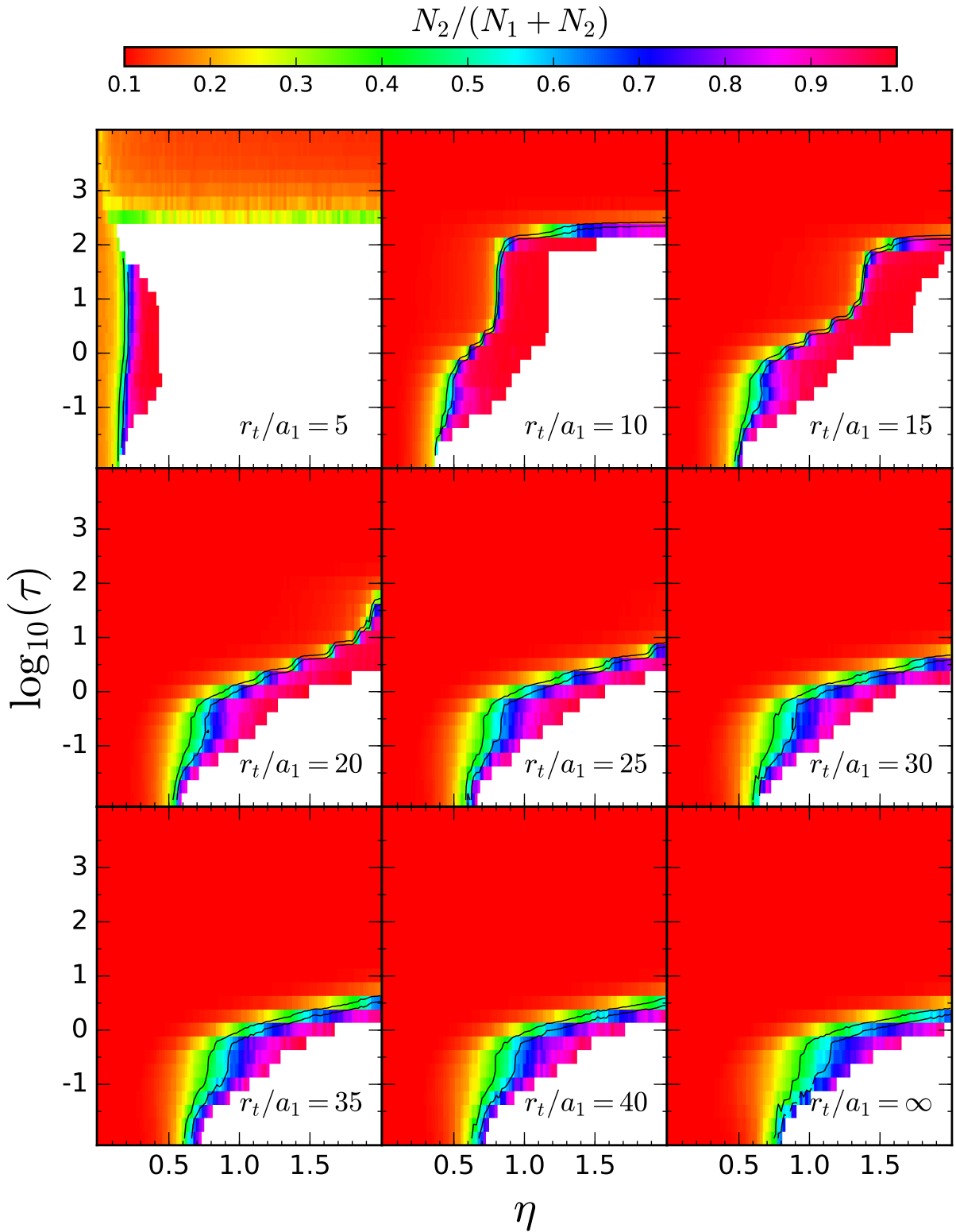
Figure 4.2a: Same as Figure 4.1 but for the number ratio of SG stars $N_2/(N_1 + N_2)$. The region enclosed by solid black lines corresponds to a number ratio of 50 ± 10 per cent for SG stars. This plot corresponds to $\lambda = 0.1$.
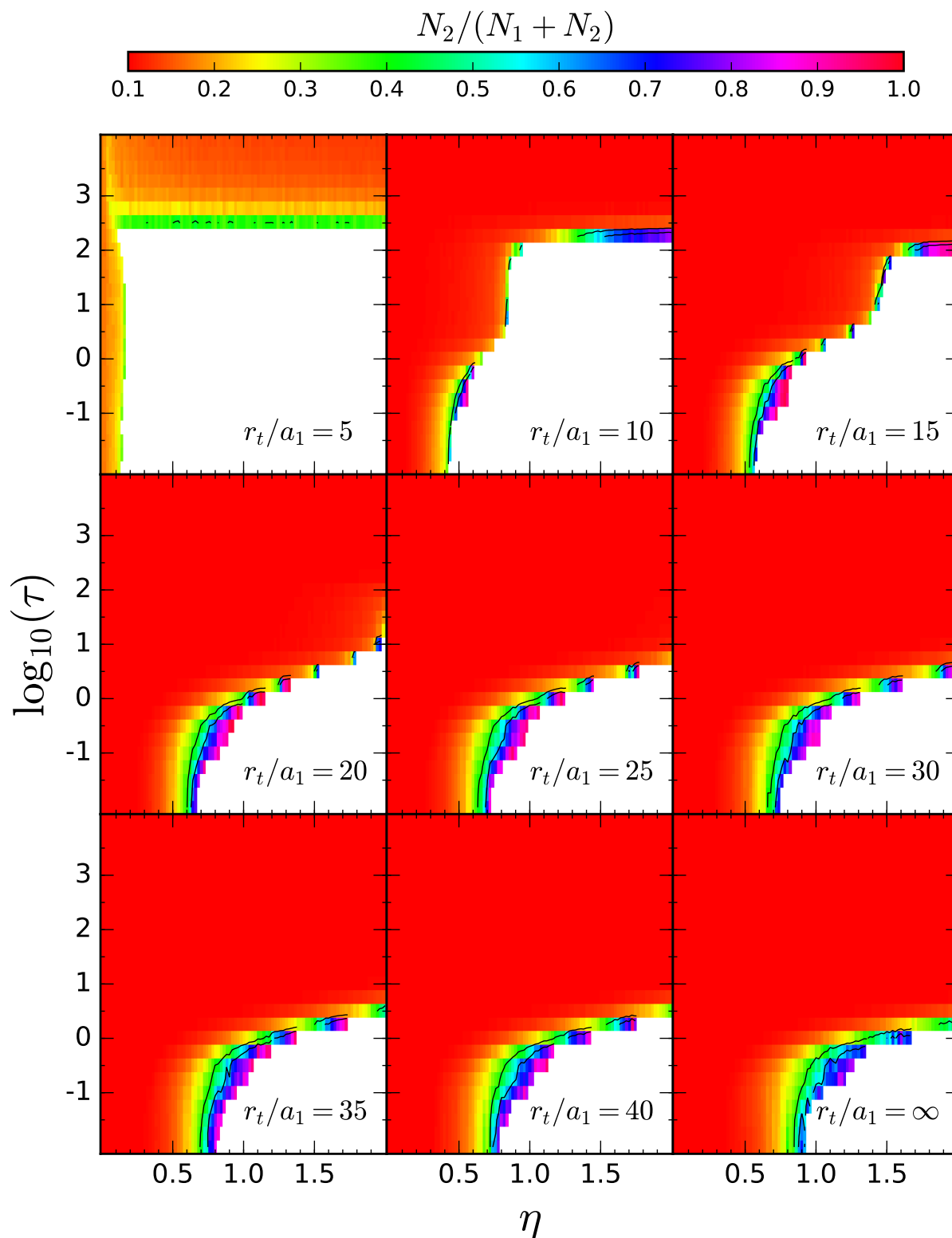
Figure 4.2b: Same as Figure 4.2a but for $\lambda = 0.2$.
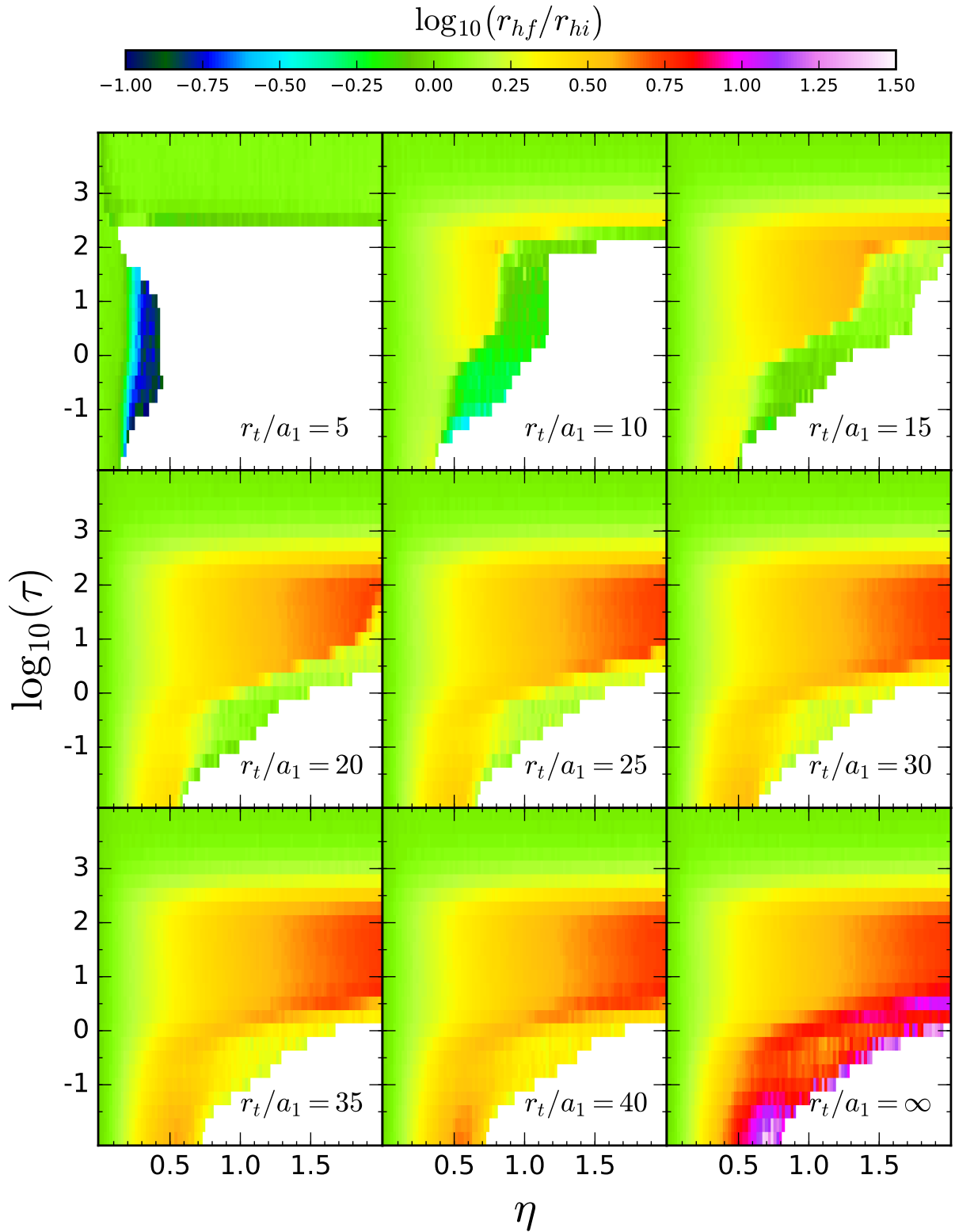
Figure 4.3a: Same as Figure 4.1 but for the logarithm of the expansion factor of the cluster $\log_{10}\left(r_{hf}/r_{hi}\right)$. This plot corresponds to $\lambda = 0.1$.
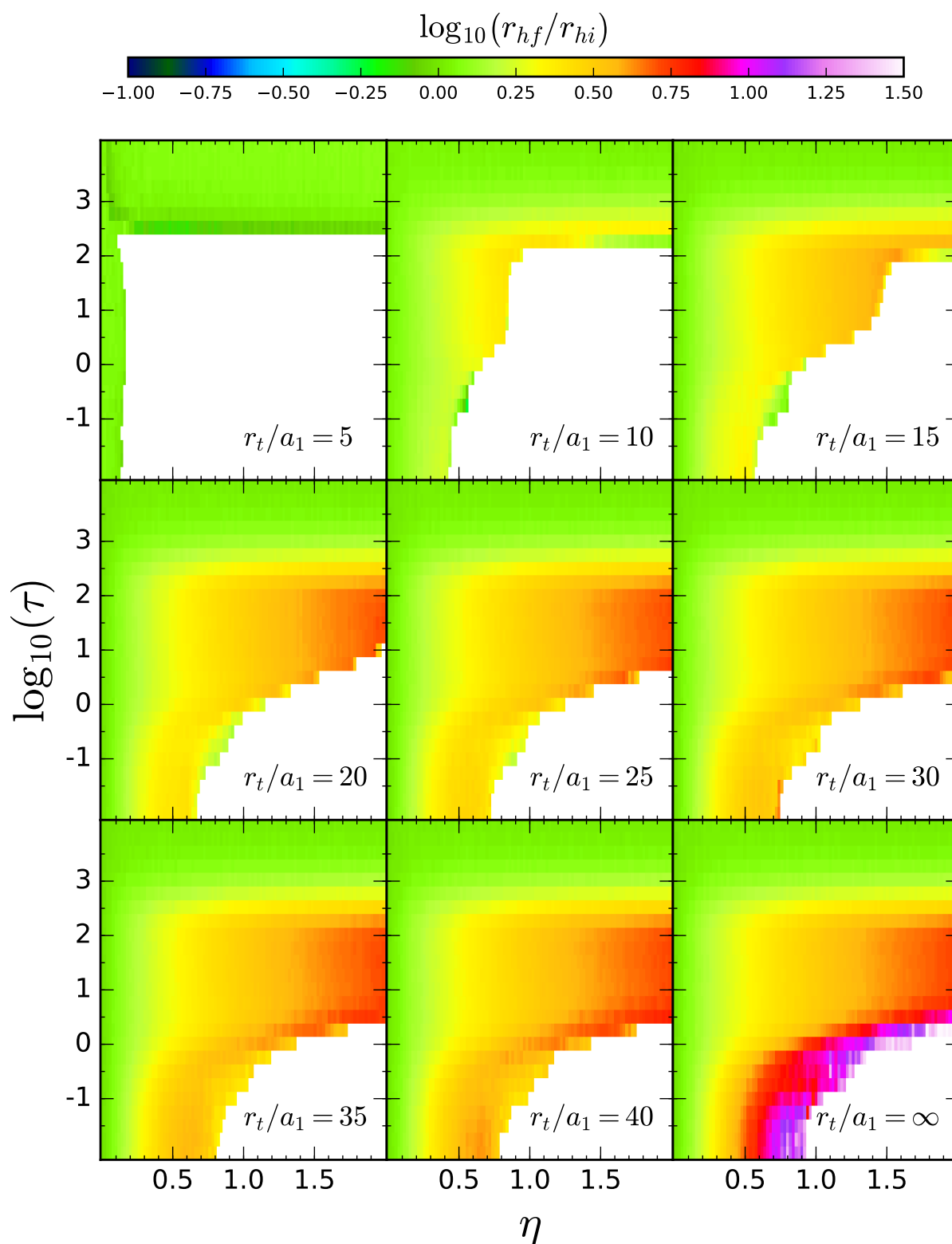
Figure 4.3b: Same as Figure 4.3a but for $\lambda = 0.2$.

2. Using equation (4.8), calculate the instantaneous tidal radius of the cluster $r_{\mathrm{t}}(t)$ as a function of the remaining cluster mass.

3. Find the stars whose distances are larger than the tidal radius calculated in the previous step and mark them as unbound stars. For isolated clusters ($r_{\mathrm{t}}/a_1 = \infty$), use the total energy of each star as the selection criterion.

4. Subtract the mass of unbound stars from the total mass of the cluster.

5. Repeat the previous steps until all bound stars reside within the tidal radius or all stars are designated as unbound stars (i.e. total disruption).

Using the above algorithm we calculate the mass-loss, number ratio of SG stars and expansion factor for the model clusters at each instant of the simulation. The outcome of our simulations is shown in figures 4.1 to 4.3 which depict the mass-loss $\Delta M/M_i$, number ratio of SG stars $N_2/(N_1 + N_2)$ and logarithm of expansion factors $\log_{10}(r_{hf}/r_{hi})$ as a function of gas fraction η and the ratio of the gas expulsion time-scale to the initial crossing time τ for different tidal radii ratios ($r_{\mathrm{t}}/a_1 = 5, 10, 15, 20, 25, 30, 35, 40, \infty$) and $\lambda = (0.1, 0.2)$. The mass-loss shown here is for stars only and does not include the gas. In these figures, the region enclosed in solid lines corresponds to 90 ± 5 per cent mass-loss and a value of 50 ± 10 per cent for the fraction of SG stars. The white filled area in the lower right corner of each plot is the total disruption zone in which all clusters will be totally destroyed as a result of significant mass-loss. The region between the black solid lines represents the set of initial conditions which match the observations. One can see that the width of this region increases in stronger tidal fields and for higher concentrations of SG stars (e.g. $\lambda = 0.1$).

The trend that we see in these figures can be explained as follows: First, the loss of gravitational potential is greater for clusters with a higher gas fraction. Second, very short gas expulsion times-scales do not allow loosely-bound stars (mainly FG stars) to compensate for the loss of gravitational potential energy and go into an equilibrium so they leave the cluster after a few crossing times, whereas in models with longer gas expulsion time-scales stars have enough time to gradually expand their orbits and remain in a quasi-equilibrium state without crossing the tidal radius and escaping from the cluster. Third, FG stars have a lower concentration than SG stars and when the gas expulsion is instantaneous, the cluster preferentially loses more FG stars, while in the adiabatic case, many of FG stars will be retained in the cluster. Fourth, clusters that lose a

Table 4.2: Range of the initial parameters used in the MC simulations.

Parameter	Range	Steps
$\overline{\log\left(\frac{M_\star}{M_\odot}\right)}$	[5.4, 6.5]	0.05
$\overline{\eta}$	[0.7, 1.5]	0.05
$\overline{\log\left(\frac{T_{\exp}}{yr}\right)}$	[3.2, 5.2]	0.05
$\overline{\log\left(\frac{r_h}{pc}\right)}^a$	[-0.25, 0.5]	0.05
$\sigma_{\log(T_{\exp}/\,yr)} = \sigma_{\log(M_\star/\,M_\odot)} = \sigma_{(\eta)}$	[0.25, 0.75]	0.25
$\sigma_{\log(r_h/\,pc)}$	[0.15, 0.45]	0.15

Note. ^aThis parameter is only relevant in models with mass-independent radii.

substantial number of stars have smaller tidal radii and have shrunk in size, hence their expansion factor is less than 1.0 and decreases with mass-loss. As a result, the mass-loss is expected to be much more extreme for clusters with higher gas fractions and shorter time-scales and such clusters must show a higher number ratio of SG stars and relatively lower expansion factors. In addition, there should be a region in the parameter space in which all clusters will be totally disrupted. The outcome of our N-body simulations are consistent with Decressin et al. (2010) who analysed the N-body models of Baumgardt & Kroupa (2007).

As it is inferred from figures 4.1 to 4.3, the initial conditions which meet the observational criteria occupy a very narrow strip in the parameter space. In addition, this region is very close to the total disruption zone, meaning that if we slightly change the initial conditions, we will either end up in the total disruption zone (SG fraction ~ 100 per cent) or the region which is far from the observed clusters (SG fraction ~ 10 per cent). We did an MC analysis as explained in Section 4.4 in order to find the physical initial conditions of GCs in terms of cluster mass, half-mass radius and gas expulsion time-scale.

4.4 MC analysis and comparison with observations

In this section we describe the details of our MC analysis on the initial conditions of star clusters. We make different sets of initial conditions for star clusters and we feed these initial conditions

Table 4.3: Outcome of the MC simulations. We have simulated 1000 clusters for each set of the initial parameters. Each row shows the best-fitting model in terms of the D parameter which is a measure of the goodness of fit and defined by equation (4.11). All models in this table have sample mean values of 50 ± 5 per cent for the fraction of SG stars. r refers to the value of the anti-correlation between the cluster mass and the fraction of SG stars. The values reported in this table are the means of 20 samples with different random seed numbers. The best-fitting models show statistical fluctuations within ± 0.1 for $\overline{\log\left(M_\star/\mathrm{M}_\odot\right)}$, $\overline{\eta}$ and $\overline{\log\left(T_\mathrm{exp}/\mathrm{yr}\right)}$ which can be inferred as an error-bar on the best-fitting parameters.

Tidal Field	λ	$\overline{\log\left(\frac{M_\star}{\mathrm{M}_\odot}\right)} \pm \sigma$	$\overline{\eta} \pm \sigma$	$\overline{\log\left(\frac{T_\mathrm{exp}}{\mathrm{yr}}\right)} \pm \sigma$	$\overline{\log\left(\frac{r_h}{\mathrm{pc}}\right)} \pm \sigma$	r	$D\,(\times 10^{-2})$
Mass-dependent radii							
MD-RG2.0	0.1	5.95 ± 0.75	1.25 ± 0.50	4.45 ± 0.50	–	-0.50	1.34
MD-RG2.0	0.2	6.05 ± 0.50	1.30 ± 0.25	3.95 ± 0.75	–	-0.72	1.86
MD-RG4.0	0.1	5.60 ± 0.50	1.30 ± 0.50	4.30 ± 0.50	–	-0.70	1.33
MD-RG4.0	0.2	5.65 ± 0.50	1.15 ± 0.25	3.60 ± 0.75	–	-0.72	1.61
MD-RG8.5	0.1	5.65 ± 0.50	1.10 ± 0.50	4.20 ± 0.25	–	-0.72	1.34
MD-RG8.5	0.2	5.60 ± 0.50	1.20 ± 0.25	4.15 ± 0.50	–	-0.70	1.58
Mass-independent radii							
MI-RG2.0	0.1	6.10 ± 0.25	0.95 ± 0.25	3.90 ± 0.25	0.10 ± 0.30	-0.85	0.87
MI-RG2.0	0.2	6.15 ± 0.25	1.00 ± 0.25	3.40 ± 0.25	0.05 ± 0.30	-0.86	0.99
MI-RG4.0	0.1	6.15 ± 0.25	0.95 ± 0.25	3.55 ± 0.25	0.10 ± 0.30	-0.83	0.90
MI-RG4.0	0.2	6.20 ± 0.25	1.05 ± 0.25	3.40 ± 0.25	-0.05 ± 0.30	-0.87	0.99
MI-RG8.5	0.1	6.05 ± 0.25	0.95 ± 0.25	3.65 ± 0.25	0.05 ± 0.30	-0.84	0.87
MI-RG8.5	0.2	6.10 ± 0.25	1.05 ± 0.25	3.40 ± 0.25	-0.05 ± 0.30	-0.86	0.97

into our grid to find the final conditions and compare them with observations of Galactic GCs. We change the initial distribution until the best match with observations is found. We have performed our MC analysis for $\lambda = 0.1$ and 0.2 separately. We adopt a log-normal distribution for the initial distribution of the cluster stellar mass (Parmentier & Gilmore, 2007, 2008) parameterized by a mean value and standard deviation of $\overline{\log\left(M_\star/\mathrm{M}_\odot\right)}$ and $\sigma_{\log(M_\star/\mathrm{M}_\odot)}$ respectively. We assume similar normal and log-normal distributions for the gas fraction and gas expulsion time-scale with mean values of $\overline{\eta}$ and $\overline{\log\left(T_\mathrm{exp}/\mathrm{yr}\right)}$ and standard deviations equal to $\sigma_{(\eta)}$ and $\sigma_{\log(T_\mathrm{exp}/\mathrm{yr})}$. We assume that the initial half-mass radii and the initial masses of GCs are related via the following

initial mass-radius relation derived by Gieles et al. (2010)

$$\log\left(\frac{r_h}{\mathrm{pc}}\right) = -3.5650 + 0.615\log\left(\frac{M}{\mathrm{M_\odot}}\right) \tag{4.9}$$

For comparison, we have also done one set of MC simulations by relaxing the mass-dependent constraint on radii and replacing it with a log-normal distribution to see how it affects the final results (*cf.* Baumgardt et al. 2008)

Tidal radii of GCs depend on the environment in which they form which is unknown. Possible choices are (1) GCs have formed in an environment similar to the present-day Milky Way, when most of its mass was already in place or (2) they formed in satellite galaxies of the Milky Way with many of them being disrupted and merged with the Milky Way (Prieto & Gnedin, 2008) and some survived like the Large Magellanic Cloud (LMC) and Fornax dwarf galaxy. For the first case we assume that our clusters are in a Galactic field with a constant circular velocity of $V_G = 220\,\mathrm{km\,s^{-1}}$ at a distance R_G from the Galactic center. The tidal radius can then be determined using the following equation (equation 1 of Baumgardt & Makino 2003)

$$r_t = \left(\frac{GM}{2V_G^2}\right)^{1/3} R_G^{2/3} \tag{4.10}$$

In our MC analysis we have considered three cases of $R_G = 2$, 4 and 8.5 kpc (solar neighbourhood) corresponding to strong, moderate and weak tidal fields in the present-day Milky Way. We will refer to these cases as MD-RG2.0, MD-RG4.0 and MD-RG8.5 for mass-dependent radii, as given by equation (4.9), and MI-RG2.0, MI-RG4.0 and MI-RG8.5 for mass-independent radii.

If GCs formed in dwarf galaxies, they would have tidal radii which are comparable to the $R_G = 8.5$ kpc case. One can take LMC with $R_G = 4$ kpc, $V_G = 70\,\mathrm{km\,s^{-1}}$ (Alves & Nelson, 2000) or Fornax with $R_G = 0.5$ kpc, $V_G = 10\,\mathrm{km\,s^{-1}}$ (Strigari et al., 2006) as an example, where R_G refers to the radius of the galaxy and V_G is the circular velocity at R_G. Using equation (4.10), the tidal radius of a cluster with a mass of $M = 10^6\,\mathrm{M_\odot}$ in such galaxies is about 190 and 175 pc respectively, close to the value of 150 pc for $R_G = 8.5$ kpc, $V_G = 220\,\mathrm{km\,s^{-1}}$. As a result our three choices of the tidal strength are sufficient to represent different environments in which GCs might have formed.

Given the tidal radius and the initial half-mass radius of each cluster, the ratio of r_t/r_h and consequently r_t/a_1 can be calculated. As a result all the required initial conditions $(\eta, \tau, r_t/a_1)$ to identify our model clusters in the N-body grid will be uniquely determined and we can find

the final properties of the clusters by interpolation between the values of the grid. In order to interpolate in our grid we need to assume that mass-loss, fraction of SG stars and expansion factor in the total disruption zone (white area in figures 4.1 to 4.3) are equal to 1.0, 1.0 and 0.0 respectively. These assumptions are based on the fact that the clusters with a mass-loss of about 99 per cent are mainly composed of SG stars and have expansion factors less than 1.0, as explained in Section 4.2. We would like to stress that we interpolate in a 3D parameter space $(\eta, \tau, r_\mathrm{t}/a_1)$, so although all clusters are in the same tidal field they don't have the same r_t/a_1.

In our analysis, we also consider the late-time adiabatic expansion of clusters as a result of the remnant gas expulsion (for clusters with $\tau > 10^3$) and also stellar evolution induced mass-loss by scaling the radii of all clusters according to the mass-radius relation of Hills ([1980]) which states that the radius of a cluster inversely scales with its mass, i.e. $r_h \propto M^{-1}$, assuming that the cluster remains in virial equilibrium after the initial significant mass-loss. We have used the AMUSE[3] (Portegies Zwart et al., [2009]; Pelupessy et al., [2013]; Portegies Zwart et al., [2013]) and analytic stellar evolution models from Hurley et al. ([2000]) to find the stellar evolution induced mass-loss for each cluster, which is on average equal to ~ 30 per cent of the initial mass of the cluster, calculated for interval $t_\mathrm{end} < t < 13.8\,\mathrm{Gyr}$, where t_end is the age of the cluster in physical units at the end of N-body simulation. The IMF of FG and SG stars is a Kroupa ([2001]) IMF which extends to $100\,\mathrm{M}_\odot$ and $8\,\mathrm{M}_\odot$ respectively. SG stars cannot be more massive than $8\,\mathrm{M}_\odot$, otherwise they will explode as SN and in the AGB scenario this will change the iron abundance of SG stars which is not consistent with observations (D'Ercole et al., [2008]). The mass-loss due to stellar evolution for SG stars depends on the upper mass limit of their IMF. They can lose as much as $\sim 25\%$ of their initial mass due to stellar evolution if their IMF extends to $8.0\,\mathrm{M}_\odot$. For FG stars whose IMF is expected to extend to $100\,\mathrm{M}_\odot$, this value is $\sim 40\%$.

We use a least-squares method, to find the model which best matches the observations. We consider the distribution of Galactic GCs from the latest version of Harris ([1996]) catalogue in a 2D plane of mass vs radius and split this 2D plane into bins and calculate the normalized frequency of GCs in each bin, i.e. the number of GCs that are in each bin divided by the total number of GCs, so that we have a 2D matrix of these normalized frequencies (hereafter O). We make a similar matrix for our simulated clusters (hereafter S). We then calculate the sum of the squared

---

[3]AMUSE (Astrophysical Multipurpose Software Environment) is available at http://amusecode.orgcode
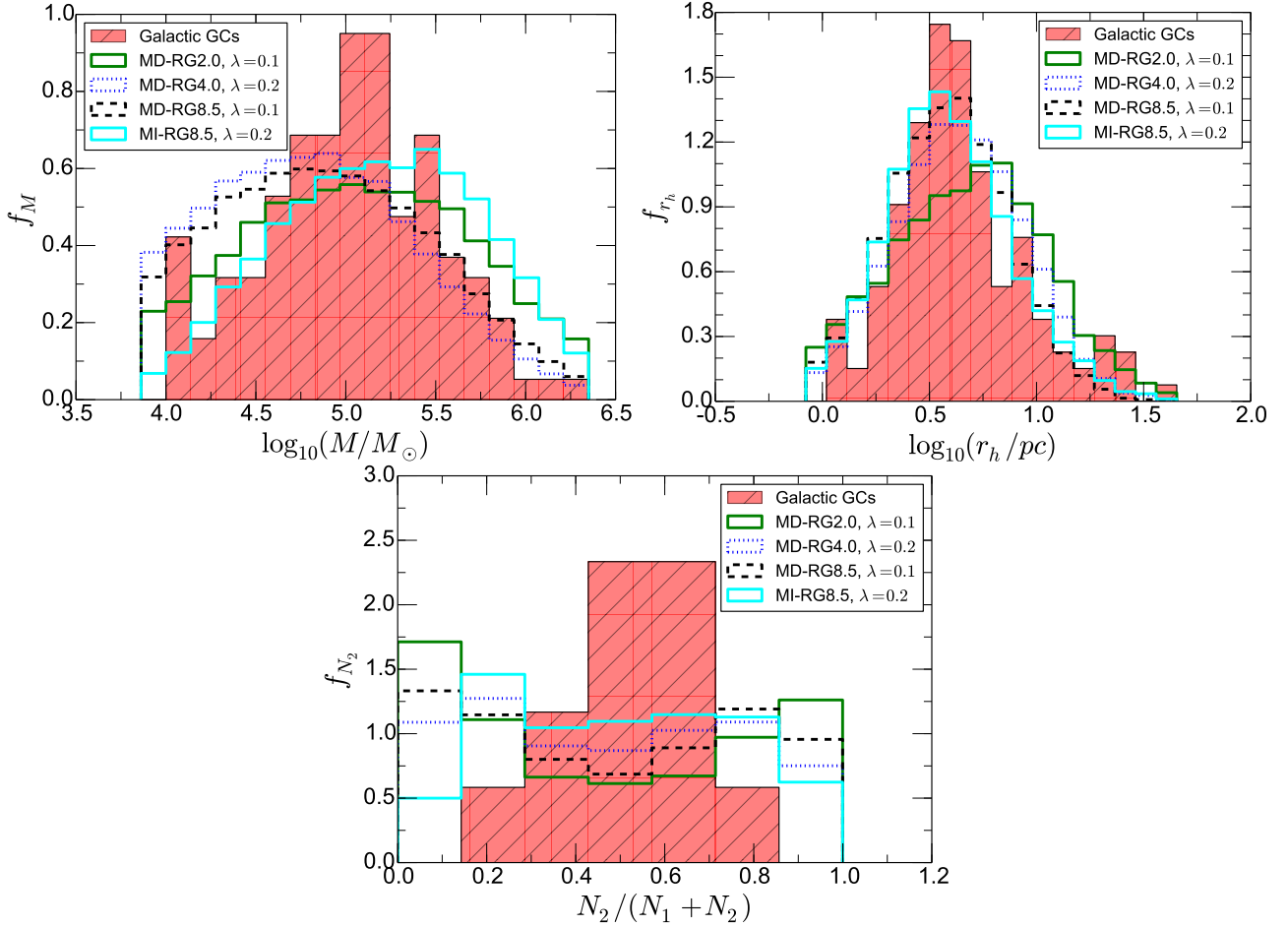
Figure 4.4: Comparison of the distribution of cluster masses (left), half-mass radii (middle) and the fraction of SG stars (right) for observed clusters (hatch-filled) and four of our best-fitting models listed in Table 4.3. Cluster masses and radii are taken from the most recent version of Harris (1996) and fraction of SG stars are taken from D'Antona & Caloi (2008). One can see that for the mass and radius histograms, the peak of the models are consistent with the peak of the observations (within $\pm 0.2\,\mathrm{dex}$). Note that we do not fit the shape of the distribution for the fraction of SG stars. Rather we only consider the sample mean value which is $50 \pm 5\,\mathrm{per\,cent}$.

residuals between matrices O and S

$$D = \sum_{ij} (O_{ij} - S_{ij})^2 \tag{4.11}$$

By minimizing D, we can find the set of initial parameters, given in Table 4.2, which best match the observational distribution. As an additional criterion, we only consider those set of initial parameters for which the distribution of the fraction of SG stars has a sample mean value of $50 \pm 5\,\mathrm{per\,cent}$. This way we can make sure that the fraction of SG stars in our simulated clusters are consistent with what we see in the observed clusters (D'Antona & Caloi, 2008). In
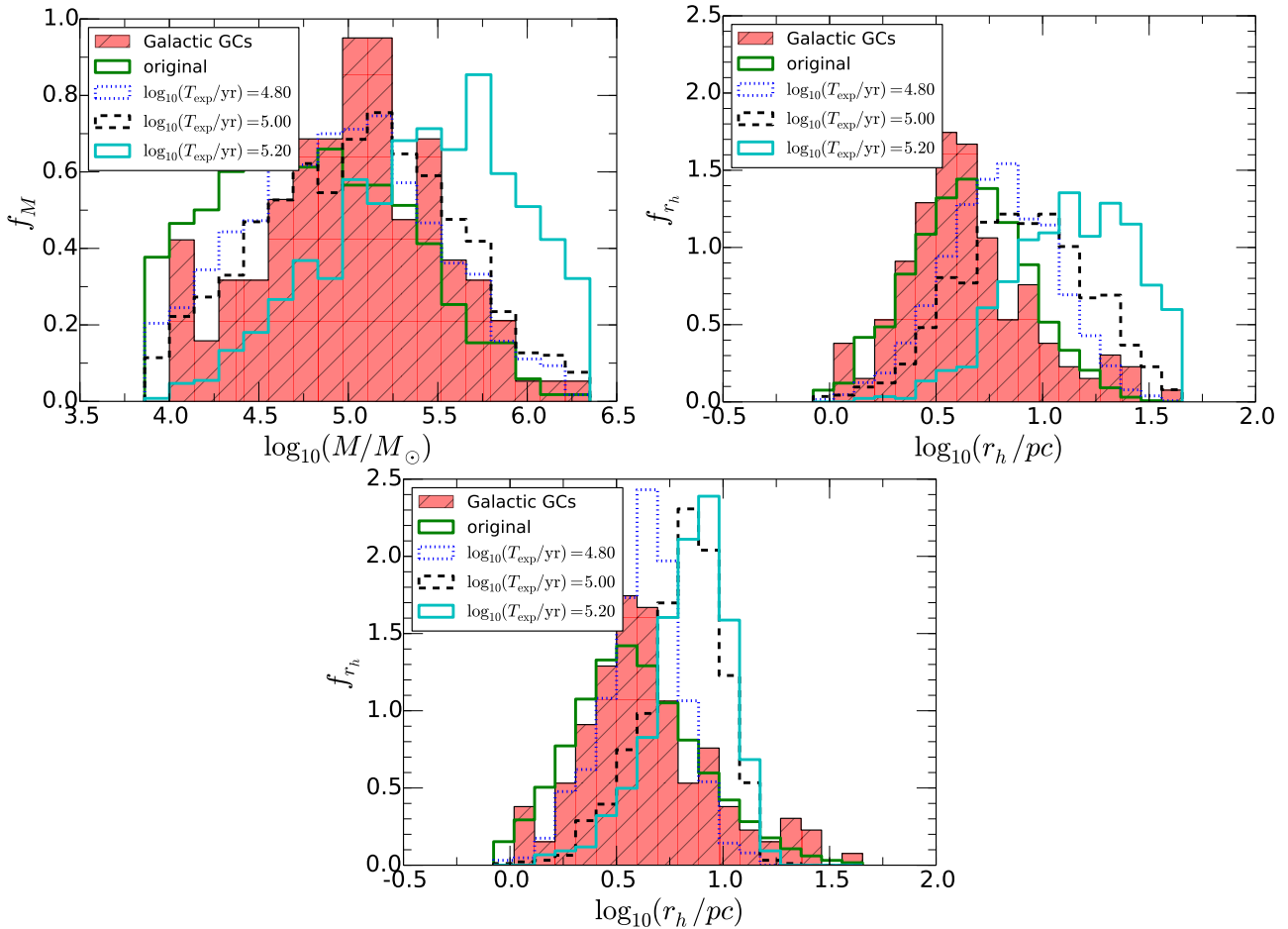
Figure 4.5: Distribution of mass and half-mass radii of MD-RG8.5 (left and middle) and MI-RG8.5 (right) both with $\lambda = 0.2$. We have plotted the best-fitting models when $\log(T_{exp}/yr)$ is fixed and equal to 4.80 (dashed-blue line), 5.00 (dashed-black line) and 5.20 (solid-cyan line). The solid-green line shows the original best-fitting model when the gas expulsion time-scale is also a free parameter. The original values for $\log(T_{exp}/yr)$ is 4.15 and 3.40 for MD-RG8.5 and MI-RG8.5 respectively. One can see that models with gas expulsion time-scales larger than 10^5 yr fail to explain the observed mass and radius distribution of Galactic GCs.

order to reduce the statistical errors, we do our MC simulations in the neighbourhood of each best-fitting model in the parameter space for 20 different random seed numbers. We then take the mean values of D and the fraction of SG stars as the selection criteria.

Table 4.3 lists our best-fitting models for different tidal fields, concentration of SG stars and dependence of cluster initial radii on the cluster masses. Figure 4.4 illustrates the outcome of our MC simulations for the following models: (MD-RG2.0, $\lambda = 0.1$), (MD-RG4.0, $\lambda = 0.2$), (MD-RG8.5, $\lambda = 0.1$) and (MI-RG8.5, $\lambda = 0.2$) and compares them with the distribution of the observed clusters. As one can see, our best-fitting models match the distribution of the observed clusters very well. The mass and half-mass radius distributions of our best-fitting models have

roughly preserved their initial log-normal distributions and the mean of the distributions have shifted towards lower masses and higher radii respectively which is a direct consequence of gas expulsion. Due to the low number of observed GCs with measured MSPs ratios, in our analysis we only fit the mean of the distribution of SG fraction and not the actual shape of the distribution. Figure 4.4 shows that our best-fitting models have sample means of 50 ± 5 per cent for the fraction of SG stars, which is consistent with observations.

According to Table 4.3, the initial stellar masses of the GCs need to be of order $5 - 15 \times 10^5 \, \mathrm{M_\odot}$ with a gas fraction of at least $\eta = 1.0$, meaning that for the significant mass-loss scenario to work we need as much mass in gas as in FG stars. In addition, GCs in stronger tidal fields need to be initially more massive compared to GCs in weaker tidal fields since mass-loss is stronger in stronger tidal fields. Equation (4.9) gives an initial half-mass radius of $\sim 1.0 \, \mathrm{pc}$ for our best mass-dependent models roughly equal to that of mass-independent models. The required gas expulsion time-scales are all extremely short, $T_{\mathrm{exp}} \sim 10^4 \, \mathrm{yr}$ ($T_{\mathrm{cross}} \sim 10^5 \, \mathrm{yr}, \tau = 0.1$). To see if higher gas expulsion time-scales also lead to acceptable fits, we fixed the value of $\log(T_{\mathrm{exp}}/\,\mathrm{yr})$ to three different values of 4.80, 5.00 and 5.20 respectively and determine the best-fitting models for the MD-RG8.5 and MI-RG8.5 models with $\lambda = 0.20$. Figure 4.5 shows that for gas expulsion time-scales larger than $T \geq 10^5 \, \mathrm{yr}$, the final properties of clusters are in strong disagreement with the observed clusters, especially for mass-dependent models, implying that the gas expulsion time-scale must have been less than $T = 10^5 \, \mathrm{yr}$.

4.4.1 Gas expulsion mechanism

According to Decressin et al. (2010) for a gas cloud with an initial mass of $\sim 10^6 \, \mathrm{M_\odot}$ and an initial half-mass radius of $0.5 \, \mathrm{pc}$, around 50 SNe are needed to unbind the gas cloud. In our case the gas clouds, which are more concentrated than the first generation stars, have initial half-mass radii of 0.1 and 0.2 pc. Since the gravitational potential energy scales with $\propto R^{-1}$, our gas clouds will need at least of order $125 - 250$ SN explosions to be dispersed. According to Fig. 5 of Decressin et al. (2010) in a cluster with $M = 10^6 \, \mathrm{M_\odot}$, at most 400 SNe/Myr will explode within 1 Myr implying that only 40 SNe will go off in $10^5 \, \mathrm{yr}$ which is a factor 3 to 6 below the required limit. As a result SN explosions seem not to able to generate enough energy to expel the gas over the short time-scales we need in our scenario.

In addition, Krause et al. (2012) have shown that the Rayleigh-Taylor (Sharp, 1984) instability destroys the huge gas shells (superbubbles) made by SN explosions before they build up enough

speed to leave the cluster, thus such superbubbles are ineffective in expelling the gas even if they have enough energy. Instead Krause et al. (2012) propose accretion onto dark remnants, such as neutron stars and black holes, as a promising mechanism which is capable to overcome the Rayleigh-Taylor instability and lead to rapid gas expulsion. According to their model, the dark remnants become active after the SN phase ($t > 35\,\mathrm{Myr}$) (Krause et al., 2013) and are able to unbind the intra-cluster medium in $0.03\,\mathrm{Myr}$ to $0.06\,\mathrm{Myr}$ depending on if neutron stars also contribute to the gas expulsion (Krause et al., 2012, 2013). According to Krause et al. (2012, 2013), This model works for protoclusters whose masses are less than $2 \times 10^7\,\mathrm{M_\odot}$ above which the gas cannot be ejected and will be retained in the cluster. This is intriguing, because firstly such a mass limit encompasses the majority of GCs except for very massive ones such as ω Cen, which is 10 times more massive, and secondly MSPs in such massive GCs have different iron abundances which could be a result of gas retention (Krause et al., 2012). The gas expulsion time-scales and the initial mass of the gas clouds that we obtained in this work, match results by Krause et al. (2012, 2013) very well. However, it is not clear whether GCs can retain gas clouds with masses of order $\sim 10^6\,\mathrm{M_\odot}$ for $\sim 35\,\mathrm{Myr}$ (see Section 4.4.2).

Moreover, our results are consistent with Krause et al. (2016) who computed a grid of numerical models for the expansion of a spherically symmetric thin shell of gas in clusters driven off by different agents (e.g. SNe or hypernovae) to see if the Rayleigh-Taylor instability is able to destroy the shell before it reaches the escape speed. They classified clusters with different masses and half-mass radii based on a compactness parameter defined as $C_5 \equiv (M_\star/10^5\,\mathrm{M_\odot})/(r_\mathrm{h}/\,\mathrm{pc})$. They found that if gas expulsion is successful it happens on a crossing time-scale. In addition, they showed common stellar feedback cannot lead to significant mass-loss for GCs with $C_5 \gtrsim 1$ and $C_5 \gtrsim 30$ if pulsar winds and hypernovae are also considered. Our clusters with $M_\star = 10^6\,\mathrm{M_\odot}$ and $r_\mathrm{h} = 1\,\mathrm{pc}$ have $C_5 \sim 10$ and expel gas within $10^5\,\mathrm{yr}$ (crossing time-scale), implying that common stellar feedback mechanisms such as SN explosions cannot lead to the desired significant mass-loss and more powerful agents such as hypernovae with energies $E > 10^{52}\,\mathrm{erg}$ are needed for gas removal.

4.4.2 Observational constraints on significant mass-loss

Fraction of SG stars and the mass of GCs

Our MC simulations predict an anti-correlation between the fraction of SG stars and the final mass of GCs. This is due to fact that to increase the fraction of SG stars, GCs need to lose many of their FG stars and since FG stars constitute ~ 90 per cent of the cluster initial mass, such GCs will have a lower final mass on average. The analysis of Decressin et al. (2010) on the Baumgardt & Kroupa (2007) models show a similar relation between the fraction of SG stars and the number of bound stars. Since the number of bound stars is proportional to the total mass of the cluster, the result of their work matches the anti-correlation that we have found for our model clusters. We have used the Pearson correlation coefficient to quantify this anti-correlation

$$r_{x,y} = \frac{\left\langle (x - \langle x \rangle)(y - \langle y \rangle) \right\rangle}{\sigma_x \sigma_y}$$

where x and y corresponds to $\log_{10}(M_\star / \mathrm{M}_\odot)$ and $N_2/(N_1 + N_2)$ respectively. The penultimate column of Table 4.3 shows the value of the anti-correlation for different models. As one can see this anti-correlation exists in all models, regardless of the tidal field strength or concentration of SG stars. The anti-correlation is more pronounced for mass-independent models with an average r value of ~ -0.85 compared to mass-dependent models with $r \sim -0.68$. We derived the same correlation coefficient for a sample of 13 Galactic GCs from D'Antona & Caloi (2008). We found that they exhibit a much weaker anti-correlation with $r = -0.07$ as the fraction of SG stars is almost independent of the cluster mass.

Bastian & Lardo (2015) studied a larger sample of GCs with multiple stellar populations (compiled from the studies of Sneden et al. 2004; Carretta et al. 2009, 2010, 2011; Carretta 2013; Kacharov et al. 2013; Carretta et al. 2014, 2015). They found that regardless of the Galactocentric distance, mass or metallicity of the GCs with MSPs, SG stars have a uniform fraction of 0.68 ± 0.07 consistent with what we deduced earlier. The uniform fraction of SG stars is at odds with the outcome of our N-body simulations which predict a statistically significant anti-correlation between the fraction of SG stars and the final mass of GCs. As a result, this can be considered as the most compelling evidence against significant mass-loss.

Metallicity distribution of stars in dwarf galaxies

Larsen et al. (2012) and Larsen et al. (2014a) found a large ratio of GCs to metal poor field stars in dwarf galaxies. Since any mass-loss from GCs will contribute to the overall metallicity distribution of field stars, this discovery imposes an upper limit for the maximum mass that can be lost by a GC in a dwarf galaxy such as Fornax. This upper limit which is about $4-5$ times the current cluster mass (Larsen et al., 2012; de Boer & Fraser, 2016) is below the required limit of the significant mass-loss scenario (~ 90 per cent). In other words, if the GCs of the Fornax dSph which are metal poor were much more massive (10-20 times more massive) initially and underwent significant mass-loss one should observe a large number of field stars in the low-metallicity end which is not the case for the metallicity distribution of Fornax. In addition, Fornax GCs are very similar to Galactic GCs in terms of abundance anomalies, mass and luminosities (D'Antona et al., 2013; Larsen et al., 2012, 2014b; de Boer & Fraser, 2016). This raises the question if significant mass-loss could have happened in Fornax GCs or not. We discuss this problem in detail in Chapter 5.

Young massive clusters

Observations of young massive clusters by Bastian et al. (2014) and Hollyhead et al. (2015) show that they have cleared out their natal gas within a few Myrs. If it was the case for GCs as well, then it poses a serious challenge for the scenario proposed by Krause et al. (2012, 2013) and would imply that either stellar winds and SN explosions do have to expel the gas or that the gas is completely consumed into stars after a few Myrs in which case the scenario suggested here would not work.

4.5   Summary

Using a large grid of *N*-body and MC simulations we have studied the consequences of primordial mass-loss for GCs with MSPs to put constraints on their initial conditions and find the best match with observations. We have demonstrated that primordial mass-loss is able to simultaneously reproduce the present-day distribution of GCs in the mass-radius plane (Fig. 4.4) and explain the large fraction of second generation stars in the cluster. However, this is only possible if: (1) the total mass of the gas remaining in the cluster is equal to that of first generation stars $M \sim 10^6 \, \mathrm{M_\odot}$ and (2) very short gas expulsion time-scales of less than 10^5 yr which is equal to about one initial

crossing time. In this case, typical initial masses of GCs are around $M = 2 \times 10^6 \, \mathrm{M_\odot}$ and their initial half-mass radii are around $r_h = 1 \, \mathrm{pc}$ (Table 4.3). Our results show that if the gas expulsion scenario studied in this chapter is true, then out of all the GCs which have survived until today about 25% will have roughly an equal number of SG and FG stars, and the rest will have either a lower or a higher SG fraction.

All of our simulations initially had $N \sim 20000$ particles. To check the effect of the number of particles on our results and the applicability of our result to real GCs which typically have $10^5 - 10^6$ stars, we did a few simulations with $N = 10^5$ with initial parameters corresponding to our best-fitting models (i.e. $\tau \leq 0$, $\eta \sim 1.0$). We did not observe any notable difference between the outcome of simulations having $N = 20000$ with that of $N = 100000$ in terms of the final mass, half-mass radius and the SG fraction. This is due to the fact that the time-scale of our simulations are much less than the relaxation time of the clusters. Moreover, any problems arising from the low N are far smaller than the other uncertainties of the model. As a result, although in our N-body simulations we have fewer particles compared to real GCs, we can safely scale our results to real GC conditions.

The outcome of our simulations shows that fraction of second generation stars is inversely proportional to the final cluster mass. This anti-correlation, which is in agreement with Decressin et al. (2010), is one of the implications of the primordial mass-loss and can be used to test the feasibility of this scenario. For our simulated clusters the anti-correlation coefficient ranges from -0.50 to -0.87. Galactic GCs do not show any anti-correlation at all (Bastian & Lardo, 2015) which poses a serious problem for the significant mass-loss scenario.

Our MC analysis includes the adiabatic expansion and mass-loss of clusters as a result of stellar evolution. However, we did not consider the effect of further change in the fraction of SG stars as a result of long-term dynamical evolution (driven by two-body relaxation) of the clusters in the galactic tidal field (Decressin et al., 2008). Nor did we consider the effect of binaries which can serve as a source of energy and cause further mass-loss and expansion (Goodman & Hut, 1989) in GCs and consequently change the fraction of SG stars after a Hubble time. These effects can in principle push the clusters out of the desired region in the parameter space (area enclosed by contour lines in Figure 4.1 and 4.2) and affect the values that we derived for the initial conditions of the clusters. As a result of binary heating or relaxation driven dynamical evolution, which increase the SG fraction, the gas expulsion time-scales of clusters could be larger than what we found here, i.e. our desired region in the parameter space can shift upward towards larger τ values.

However, since the lifetimes of most GCs are significantly longer than a Hubble time (Baumgardt & Makino, 2003), we do not expect the fraction of SG stars to change significantly over a Hubble time due to dynamical evolution, and therefore our upper limit of 10^5 yr for the gas expulsion time-scale is unlikely to change significantly.

Moreover, in our MC analysis, we have assumed a log-normal distribution for the initial cluster mass function. Instead of a log-normal relation, one can also assume a power-law distribution $dN \propto M^{-\alpha}$ for the cluster mass function, with $\alpha \approx 2$, as seen for young massive star clusters in interacting and merging galaxies (Whitmore & Schweizer, 1995; Whitmore et al., 1999). Baumgardt et al. (2008) for example studied the effect of residual gas expulsion on gas embedded star clusters and found that it is possible to turn a log-normal mass function into a power-law over a Hubble time due to gas expulsion. They found that this effect is almost independent of the strength of the external tidal field or the assumed model for gas expulsion. As a result, our model could also work for an initial power-law distribution. A potential problem for such a mass function could be the overproduction of the field halo stars due to the large number of disrupted clusters.

<div style="text-align: right; font-size: 3em;">5</div>

Limits on the significant mass-loss scenario based on the GCs of the Fornax dSph

As explained in Chapter 4, the metallicity distribution of field stars and GCs in dwarf galaxies such as Fornax dSph is considered as evidence against significant mass-loss in GCs.

In this chapter[1] we propose a solution to reconcile the observed metallicity distribution of dwarf galaxies with the significant mass-loss scenario. If the speeds by which the unbound stars leave the Fornax GCs is large enough then these stars can be stripped off by the Milky Way and leave the gravitational field of Fornax, hence do not contribute to the metallicity distribution of field stars. In this case the upper limit of mass-loss ($\sim 80\%$) for Fornax GCs given by Larsen et al. (2012) does not apply any more and the metallicity distribution of GCs and field stars cannot be interpreted as an issue for significant mass-loss in GCs. We study the viability of our proposed solution by numerically integrating the orbit of stars which initially belong to Fornax GCs and then become unbound (hereafter runaway stars). We follow their trajectory over a Hubble time in the combined potential field of Fornax and the Milky Way to see whether they leave the Fornax dSph or not.

The chapter is structured as follows. In the next section we explain the setup and the details of our numerical orbit integration. In Section 5.2 we bring the results of the simulations. In Section 5.3 we discuss the implications of our results for the formation scenarios of chemically peculiar stars in dwarf galaxies and summarize the main results in Section 5.4.

---

[1]This chapter is based on Khalaj & Baumgardt (2016) and the published version is available at http://dx.doi.org/10.1093/mnras/stv2944

Table 5.1: Adopted models in this study for the density profile of the Fornax dSph given by equation (5.2). γ_0, γ_∞, η, r_s and the total mass are directly taken from Table 2 of Cole et al. (2012). V_c is the circular velocity derived by numerical integration (Figure 5.1) and tidal radii are derived from equation (5.6).

Model	Total Mass	γ_0	γ_∞	η	r_s	Tidal Radius	V_c (500 pc)	V_c (1000 pc)	V_c (3000 pc)
-	$10^8\,\mathrm{M_\odot}$	-	-	-	kpc	kpc	$\mathrm{km\,s^{-1}}$	$\mathrm{km\,s^{-1}}$	$\mathrm{km\,s^{-1}}$
large core (LC)	8.00	0.07	4.65	3.70	1.40	6.7	13.3	24.2	30.3
weak cusp (WC)	1.23	0.08	4.65	2.77	0.62	3.6	15.2	17.9	12.8
intermediate cusp (IC)	1.51	0.13	4.24	1.37	0.55	3.8	16.0	17.3	13.6
steep cusp (SC)	1.98	0.52	4.27	0.93	0.80	4.2	16.0	17.2	14.6

5.1   Numerical simulations

5.1.1   Milky Way and Fornax models

We use a logarithmic potential field to model the Milky Way halo

$$\Phi(R) = \frac{1}{2}V_\infty^2 \ln\left(R_c^2 + R^2\right) \tag{5.1}$$

where R_c is the core-radius and V_∞ is the asymptotic velocity. We assume $R_c = R_\odot = 8300\,\mathrm{pc}$ and $V_\infty = V(R_\odot) = 239\,\mathrm{km\,s^{-1}}$ (McMillan, 2011; Irrgang et al., 2013). In a right-handed Galactocentric coordinate system whose $x-$, $y-$ and z axes point towards the Sun, the direction of the orbital motion of the Sun and the North Galactic pole respectively, the current position and velocity vectors of Fornax are $\vec{R} = (-41.3\,\mathrm{kpc}, -51.0\,\mathrm{kpc}, -134.1\,\mathrm{kpc})$ and $\vec{V} = (-38\,\mathrm{km\,s^{-1}}, -158\,\mathrm{km\,s^{-1}}, 114\,\mathrm{km\,s^{-1}})$ respectively (Pawlowski & Kroupa, 2013). By numerical integration of the Fornax orbit in the Milky Way potential field, given by equation (5.1), we find that the current distance, perigalactic distance, apogalactic distance, eccentricity, orbital inclination and radial and azimuthal periods of Fornax are $R = 149.3\,\mathrm{kpc}$, $R_p = 99.4\,\mathrm{kpc}$, $R_a = 154.7\,\mathrm{kpc}$, $e \equiv (R_a - R_p)/(R_a + R_p) = 0.22$, $i = 81°$, $T_r = 2.4\,\mathrm{Gyr}$ and $T_\psi = 3.3\,\mathrm{Gyr}$.

For the density profile of Fornax, we use the recent models of Cole et al. (2012) which are derived by applying Markov Chain MC analysis to the kinematic data of more than 2000 stars in Fornax. These models have the benefit of including both the stellar and dark matter content of Fornax and that they cover a wide-range of inner density slopes (Cole et al., 2012). The models
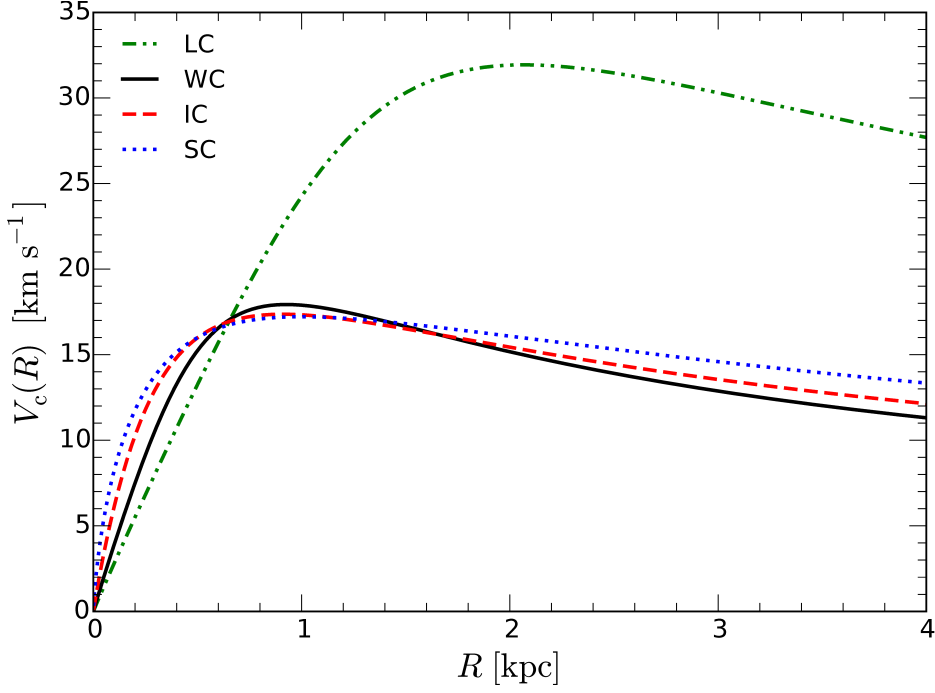
Figure 5.1: The Fornax velocity curves as a function of radius according to different models given by equation (5.2). Compared to cuspy models, the LC model predicts a larger circular velocity for $R > 0.8$ kpc due to its larger enclosed mass.

are designated by LC, WC, IC and SC, all of which have the following form for the density profile

$$\rho(r) \propto \left(\frac{r}{r_{\mathrm{s}}}\right)^{-\gamma_0} \left(1 + \left(\frac{r}{r_{\mathrm{s}}}\right)^{\eta}\right)^{\frac{\gamma_0 - \gamma_\infty}{\eta}} \mathrm{sech}(r/10\,\mathrm{kpc}) \tag{5.2}$$

where r_{s} is a scale radius, $\gamma \equiv -\mathrm{d}\ln\rho/\mathrm{d}r$ is the logarithmic density slope and η is a constant. The best-fitting parameters are found using Markov Chain MC. Table 5.1 summarizes the characteristics of these models.

The models describe the observed velocity dispersion profile of Fornax very well, however they do not lead to analytical relations for other dynamical parameters such as the enclosed mass at each radius $M(R)$. As a result we used numerical integration to find $M(R)$ (needed for force calculations) and the circular orbital velocity $V_{\mathrm{c}}(R)$ (needed for initial conditions) and verified our results by comparing with Fig. 2 of Cole et al. (2012). Figure 5.1 illustrates $V_{\mathrm{c}}(R)$ for different models adopted in this study. The effect that the choice of the density profile of Fornax has on our results is discussed in Section 5.2.

5.1.2 Tidal radius of Fornax and escape criterion

For each of the density profiles introduced in Section 5.1.1, we need to calculate the tidal radius R_t of Fornax. The tidal radii are needed later as they specify the ejection criteria from Fornax.

First we derive an equation to calculate the tidal radius of Fornax in the gravitational field of the Milky Way given by equation (5.1). Following the approach and the notation of Renaud et al. (2011), the tidal radius of a stellar system with mass M, on a circular orbit with radius R_G around a host galaxy with an arbitrary potential field ϕ_G, can be written as follows (equations 10 and 17 therein)

$$R_t = \left(\frac{GM}{\lambda_{e,1}} \right)^{\frac{1}{3}} \tag{5.3}$$

where tidal radius R_t is defined as the distance of the first Lagrangian point (L_1) from the center of the system and $\lambda_{e,1}$ is the largest eigenvalue of the effective tidal tensor (i.e. the sum of the tidal and centrifugal potentials) and is given by

$$\lambda_{e,1} = \left(-\frac{\partial^2 \phi_G}{\partial x^2} \right)_{R_G} - \left(-\frac{\partial^2 \phi_G}{\partial z^2} \right)_{R_G} \tag{5.4}$$

In the derivation of this equation, it has been assumed that the potential of the stellar system is simply $-GM_c/r$ which is a reasonable assumption at the tidal radius (Renaud et al., 2011).

The substitution of the equation (5.1) into equation (5.4) yields

$$\lambda_{e,1} = \frac{2R_G^2 V_\infty^2}{(R_c^2 + R_G^2)^2} \tag{5.5}$$

hence the tidal radius is

$$R_t = \left(\frac{GM}{2V_\infty^2} \right)^{\frac{1}{3}} R_G^{\frac{2}{3}} \left(\left(\frac{R_c}{R_G} \right)^2 + 1 \right)^{\frac{2}{3}} \tag{5.6}$$

One can also use equation 10 of Bertin & Varri (2008) and derive the same formula for the tidal radius.

Note that for $R_G \gg R_c$, the last term on the right-hand side of the equation (5.6) goes to zero and one can approximate the above equation for the logarithmic potential by the following form which is essentially the tidal radius of a system in an isothermal sphere[2] (Baumgardt & Makino, 2003)

$$R_t \approx \left(\frac{GM}{2V_\infty^2} \right)^{\frac{1}{3}} R_G^{\frac{2}{3}}, \quad \frac{R_G}{R_c} \gg 1 \tag{5.7}$$

---

[2] $\rho(r) \propto r^{-2}$

We have derived equation (5.6) assuming a circular orbit for Fornax around Milky Way. Baumgardt & Makino (2003) and Webb et al. (2013, 2014) showed that stellar systems with eccentric orbits around a host galaxy have a different tidal radius and mass-loss rate compared to circular orbits. However, by extrapolation of the results presented in Webb et al. (2013), when the eccentricity is small ($e \leq 0.25$), as is the case for Fornax with $e = 0.22$, the tidal radius of a stellar system can be approximated by that of a circular orbit with a radius equal to the perigalactic distance of the elliptic orbit. As a result, we approximate the Fornax effective tidal radius by replacing R_{G} in equation (5.6) with the perigalactic distance of Fornax orbit ($R_{\mathrm{p}} = 99.4\,\mathrm{kpc}$). Depending on the model that we have adopted for the density profile of Fornax, we obtain different total masses and different tidal radii which are listed in Table 5.1. Cuspy models have an average tidal radius of $R_{\mathrm{t}} \approx 3.9\,\mathrm{kpc}$ (comparable with $R_{\mathrm{t}} = 3.6\,\mathrm{kpc}$ from Walcher et al. 2003), whereas the tidal radius of the LC model is $R_{\mathrm{t}} = 6.7\,\mathrm{kpc}$ owing to its larger total mass. For comparison, by fitting King (1966) truncated models to the density profile of Fornax, Irwin & Hatzidimitriou (1995) derived a tidal radius of $71\overset{\prime}{.}1 \pm 4\overset{\prime}{.}0$ for Fornax, which corresponds to a tidal radius of $3.1 \pm 0.16\,\mathrm{kpc}$ at the current distance of $149.3\,\mathrm{kpc}$ (derived in Section 5.1.1) for Fornax .

5.1.3 Initial conditions of runaways stars

Our assumption is that runaway stars initially belong to one of the Fornax GCs and become unbound by some unknown mechanism. As a result, they all have the same initial distance from the centre of Fornax. In our simulations, the initial speed of each runaway star corresponds to its excess speed, i.e. its speed when it is infinitely far from the cluster and is no longer effected by its gravitational pull. As a result, we don't consider the gravitational effect of the GCs on these runaway stars. Nor do we consider the gravitational interaction between stars. The runaway stars only feel the gravitational force of Fornax and the Milky Way.

We have $N = 20000$ stars in each simulation and give all of them the same initial speed and the same initial distance from the centre of Fornax. The orientation of the velocity vector of each runaway star is determined from its speed and a uniform spherical distribution. For the whole grid of runs we vary the speed of runaway stars from 0.0 to $50.0\,\mathrm{km\,s^{-1}}$ spaced by $0.5\,\mathrm{km\,s^{-1}}$. The initial distance of the stars varies from 0.5 to $3.0\,\mathrm{kpc}$ for cuspy models and 3.0 to $6.0\,\mathrm{kpc}$ for the LC model, spaced by $0.5\,\mathrm{kpc}$. These values are below the tidal radius of Fornax for each density profile. The initial position of Fornax is set to its apogalacticon in each simulation.

We let the simulations run for $T = 13.8\,\mathrm{Gyr}$ and determine the fraction of stars lost from
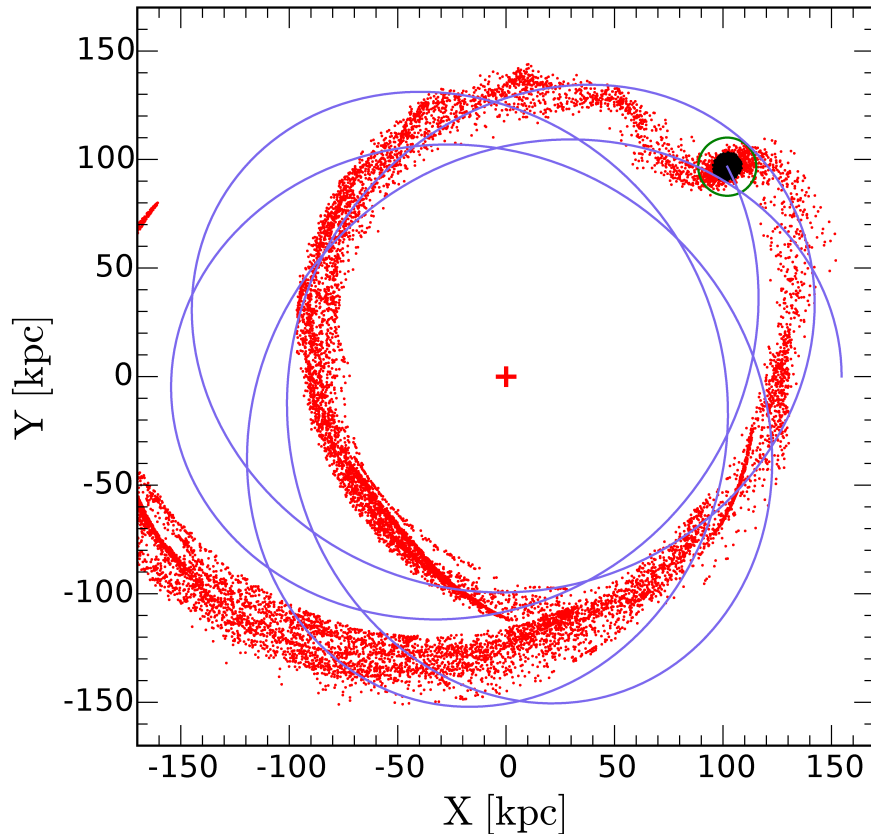
Figure 5.2: Spatial distribution of stars in the halo of the Milky Way for the LC model after one Hubble time. The Milky Way is denoted by the central cross at the origin. In this simulation, the initial distance of the stars from the centre of Fornax is $R = 3.0\,\mathrm{kpc}$ and their initial speed is $v = 35\,\mathrm{km\,s^{-1}}$. Red points represent stars which have left Fornax (about 70 per cent mass-loss). The clump of black points enclosed by the green circle shows stars which still reside within the tidal radius of Fornax. The radius of the green circle is equal to 2 times the tidal radius of Fornax at perigalacticon. The Rosette like orbit of Fornax is shown by the blue solid line. In this figure, X and Y correspond to the coordinate of stars in the orbital plane of Fornax and not the Galactocentric rest frame defined in Section 5.1.1.

Fornax using the tidal radii found in Section 5.1.2. We consider all the stars with $R > 2R_{\mathrm{t}}$ to find the total mass-loss at each snapshot where R_{t} is the tidal radius of Fornax.

We integrate the orbit of stars using the Leapfrog integration scheme with a constant time step ($\Delta t = \mathrm{const}$). For each star, we have on average ~ 300 time steps per orbital period of the star around the Fornax dSph. The accuracy of the Leapfrog scheme for the position and the velocity is $\mathcal{O}(\Delta t^2)$. Refer to Section 4.2 for further details about the Leapfrog scheme.
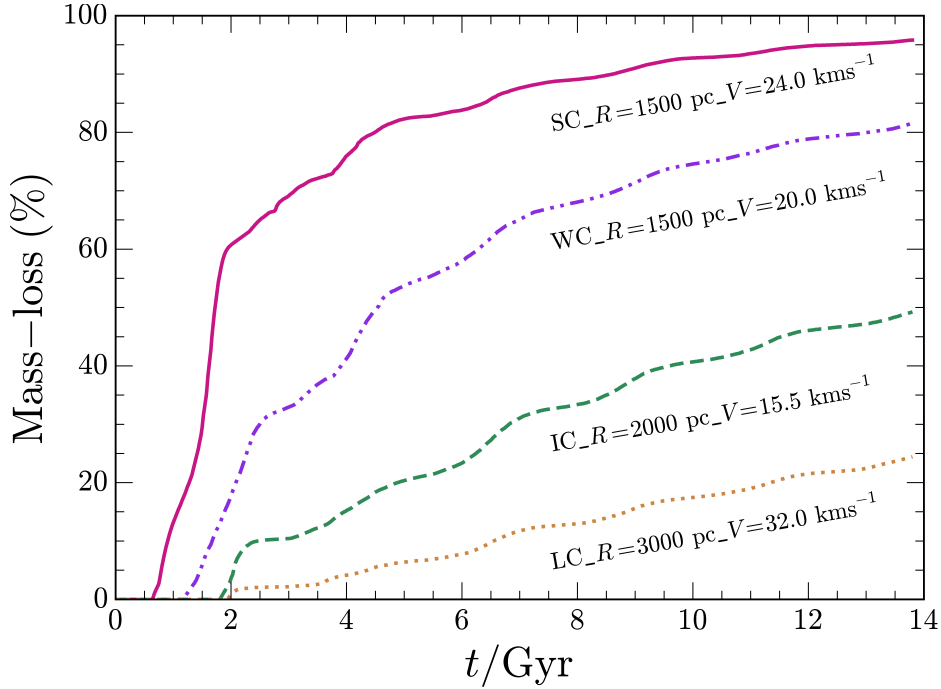
Figure 5.3: Mass-loss as a function of time for 4 different simulations. The first entry in the label of each simulation is the adopted model for the density profile of Fornax, the second entry is the initial distance of the stars from the centre of Fornax (equal to the orbital radius of GCs) and the last entry is the initial speed of the stars. Note how the LC model has a lower mass-loss compared to other models for $R < 3.0\,\mathrm{kpc}$. For models with significant mass-loss, the major mass-loss happens in the first $5\,\mathrm{Gyr}$, followed by a slow rise afterwards.

5.2   Results

Figure 5.2 shows the distribution of runaway stars with respect to the Milky Way after a Hubble time for one of the LC simulations, with $R_{\mathrm{GC}} = 3.0\,\mathrm{kpc}$ and $v = 35\,\mathrm{km\,s^{-1}}$. According to this figure, a fraction of stars (~ 30 per cent) will remain in Fornax and the rest leaves Fornax due to their large velocities. The evolution of mass-loss over a Hubble time is depicted in Figure 5.3. For the runs with a large mass-loss (> 70 per cent), the majority of runaway stars escape Fornax after only $5\,\mathrm{Gyr}$ after which the mass-loss increases only slowly.

Figure 5.4 shows the projected number density of stars calculated using the infinite projections method of Mashchenko & Sills (2005) which reduces the random fluctuations caused by low number statistics. The densities are almost constant inside Fornax ($R < R_{\mathrm{t}}$) and then rapidly decrease outside the tidal radius. Beyond $R > 2R_{\mathrm{t}}$ the density curves tend to a constant value which is equal to the background density.

The whole grid of our numerical simulations is given in Figure 5.5 which illustrates the mass-
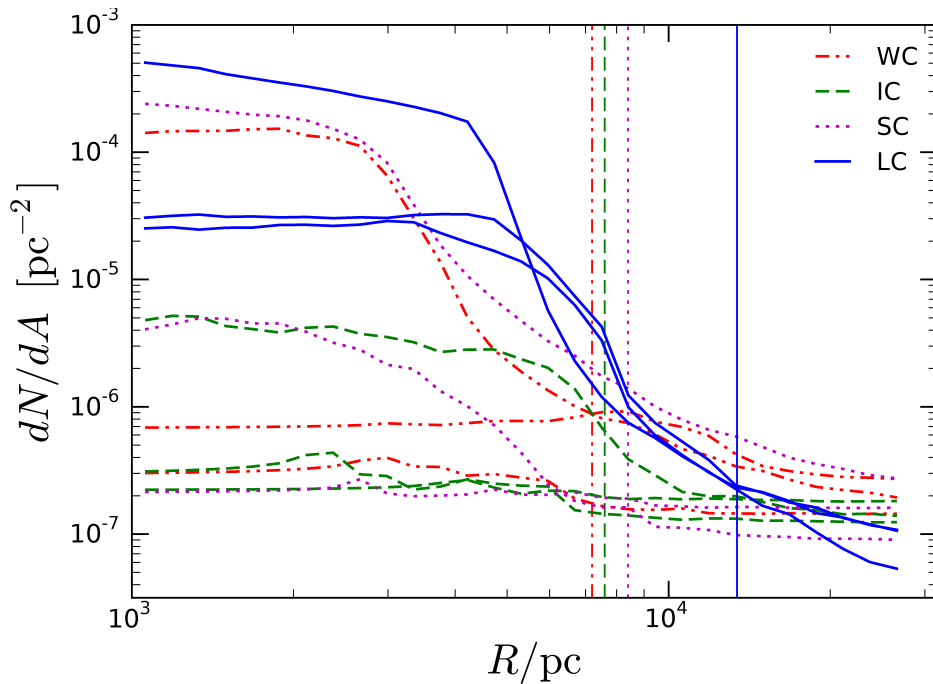
Figure 5.4: Surface density of stars as a function of projected radius for different models after a Hubble time calculated using infinite projections method (Mashchenko & Sills, 2005). The vertical lines mark $2R_t$ where R_t is the tidal radius of Fornax at perigalacticon according to different models. The densities are almost constant inside Fornax and they drop beyond R_t and start to level off beyond $2R_t$ as they reach the background density. Curves with the same color and line style correspond to the same density profile for Fornax but differ in model parameters, i.e. different initial orbital radii and initial speed for stars. The parameters for the models shown in this figure are (from the top to the bottom for each density profile) WC: $(2.5\,\mathrm{kpc}, 15\,\mathrm{km\,s^{-1}})$, $(1.5\,\mathrm{kpc}, 35\,\mathrm{km\,s^{-1}})$, $(1.0\,\mathrm{kpc}, 30\,\mathrm{km\,s^{-1}})$; IC: $(2.5\,\mathrm{kpc}, 20\,\mathrm{km\,s^{-1}})$, $(1.5\,\mathrm{kpc}, 27\,\mathrm{km\,s^{-1}})$, $(1.0\,\mathrm{kpc}, 35\,\mathrm{km\,s^{-1}})$; SC $(1.5\,\mathrm{kpc}, 35\,\mathrm{km\,s^{-1}})$, $(2.5\,\mathrm{kpc}, 15\,\mathrm{km\,s^{-1}})$, $(1.5\,\mathrm{kpc}, 25\,\mathrm{km\,s^{-1}})$; LC: $(4.5\,\mathrm{kpc}, 15\,\mathrm{km\,s^{-1}})$, $(5.5\,\mathrm{kpc}, 25\,\mathrm{km\,s^{-1}})$, $(3.5\,\mathrm{kpc}, 35\,\mathrm{km\,s^{-1}})$.

loss from the Fornax dSph as a function of initial speed and the initial distance of the stars from the centre of Fornax. Mass-loss increases for larger radii and larger speeds, which is the direct consequence of Fornax potential field to become weaker at larger radii. Using this grid, one can estimate the mass-loss which could have happened in Fornax, provided that the initial orbital radii of Fornax GCs are known.

The current projected distances of Fornax GCs from the centre of the dSph are $1.60\,\mathrm{kpc}$, $1.05\,\mathrm{kpc}$, $0.43\,\mathrm{kpc}$, $0.24\,\mathrm{kpc}$ and $1.43\,\mathrm{kpc}$ (Mackey & Gilmore, 2003) and they are all old, with ages ranging from 7 to 14 Gyr (Strader et al., 2003; Mackey & Gilmore, 2003). This is puzzling since the GCs are moving in a dark matter halo which can cause dynamical friction and shrink the orbital radius of Fornax GCs within a Hubble time. Yet we don't see any cluster merging in the centre of
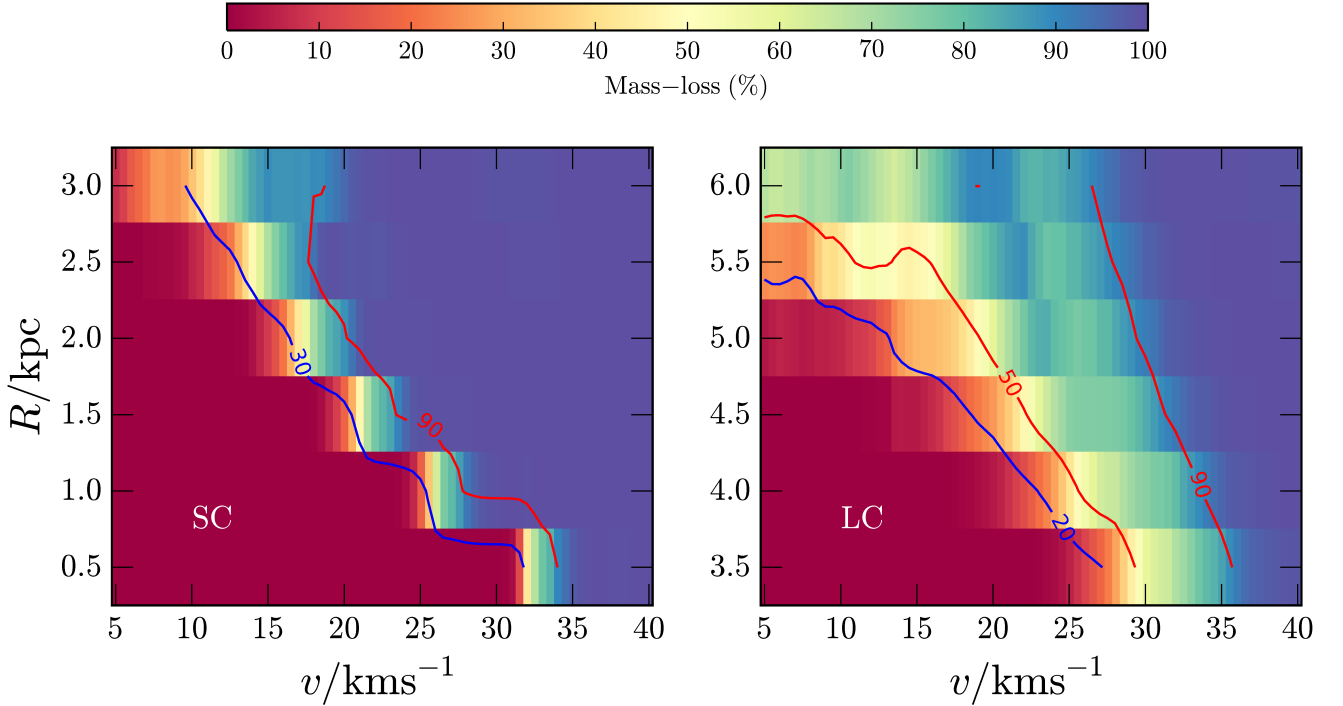
Figure 5.5: Mass-loss from Fornax as a function of the initial velocity and the initial distance of stars from the centre of Fornax for SC and LC models. WC and IC models have a very similar pattern to the SC model. The LC model predicts a lower mass-loss compared to cuspy models for $R < 3.0\,\mathrm{kpc}$.

Fornax and there is no evidence of a bright stellar nucleus in the dSph. This is commonly referred to as the timing problem of Fornax GCs. Cole et al. (2012) studied this problem and generated a wide range of initial conditions for the orbit of Fornax GCs. They showed that, in case of a cuspy density profile for Fornax (i.e. WC, IC and SC models), when the initial orbital radii of Fornax GCs are less than $2 - 3\,\mathrm{kpc}$, the orbital radii of Fornax GCs significantly decrease as a result of dynamical friction after only $2\,\mathrm{Gyr}$. In addition, all clusters except for Fornax 1 will fall into the centre of Fornax over a Hubble time. Since Fornax GCs are located at radii far from the central region of the dSph (i.e. $r > 200\,\mathrm{pc}$), this implies that the initial orbital radii of clusters must have been larger than their current orbital radii, i.e. they all have initial orbital radii of $\geq 2\,\mathrm{kpc}$. Otherwise, they must have fallen into the centre of the dSph and merge by now. This can be seen from figure 4 of Cole et al. (2012) which shows the evolution of the orbital radii of Fornax GCs for different density profiles. In contrast, the infall of the clusters does not happen in case of the LC model. GCs in this model show a dynamical buoyancy instead of dynamical friction as shown by Cole et al. (2012). It can be inferred from figure 4 of Cole et al. (2012) that Fornax GCs formed more or less at the same radii as they are seen today ($R < 1.5\,\mathrm{kpc}$) in this case.

Knowing that the initial orbital radii of GCs must be either $2-3\,\mathrm{kpc}$ or $\sim 1.5\,\mathrm{kpc}$ depending on the density profile, what remains is to see at what radius the runaway stars are released. The significant mass-loss of the GCs occurs over a time-scale of the order of megayears (see Section 5.3). This is much smaller than the dynamical evolution time-scale of the orbits due to dynamical friction/buoyancy which is of the order of gigayears (Cole et al., 2012). As a result one can assume that when the significant mass-loss happened in Fornax GCs, the runaway stars were released with an initial orbital radius equal to that of the cluster, i.e. $2-3\,\mathrm{kpc}$ for cuspy models and $\sim 1.5\,\mathrm{kpc}$ for the LC model.

Combining these facts with Figure 5.5, one can see that for all of the cuspy models, mass-loss can be as high as 90 per cent for $R = 2-3\,\mathrm{kpc}$ and $v > 20\,\mathrm{km\,s^{-1}}$, whereas for the LC model this value is less than 10 per cent. This indicates that the LC model systematically predicts a lower mass-loss at the same radii compared to cuspy models (also evident in Figure 5.3). To achieve the same mass-loss from Fornax in case of the LC model, the speed of stars need to be $v > 35\,\mathrm{km\,s^{-1}}$ at $R = 2-3\,\mathrm{kpc}$. The reason that the LC model has a lower mass-loss is due to its larger enclosed mass at each radius which leads to a larger gravitational force compared to cuspy models. This can also be inferred from Figure 5.1 which shows that the LC model has a larger circular velocity for $R > 0.8\,\mathrm{kpc}$.

5.3   Implications for formation scenarios of chemically peculiar stars

So far, two mechanisms have been suggested to produce a significant mass-loss from GCs: stellar evolution induced mass-loss in extended clusters (D'Ercole et al., 2008) and primordial gas expulsion (Khalaj & Baumgardt 2015; Chapter 4). In this section, we estimate the mass-loss which can be achieved by both of these mechanisms based on our results given in Section 5.2.

5.3.1   Gas expulsion

In this section we test whether we can achieve a high mass-loss from Fornax if runaway stars are a result of gas expulsion in GCs.

In Chapter 4, we did N-body simulations of GCs with two stellar populations to study the role of primordial gas expulsion on the mass-loss. Using a series of MC simulations, we then compared the simulated GCs with Galactic clusters and found that gas expulsion induced mass-loss can
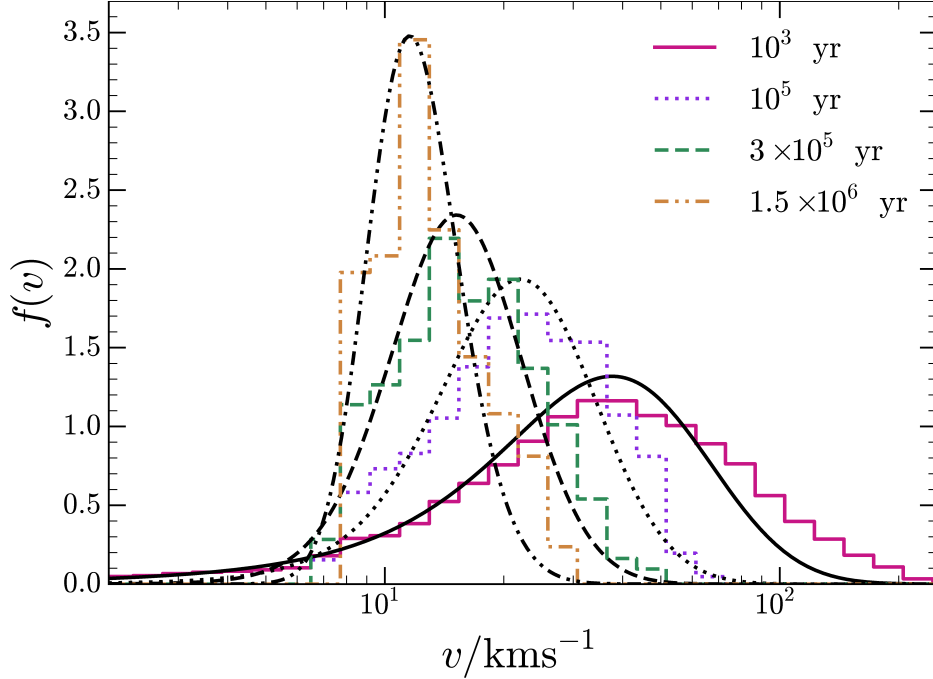
Figure 5.6: The normalized distribution of excess speeds of runaway stars for an isolated cluster with an initial stellar mass of $M_\star = 10^6 \, \mathrm{M_\odot}$ and an initial half-mass radius of $R_\mathrm{h} = 1.0 \, \mathrm{pc}$ for different gas expulsion time-scales. Data is taken from our N-body grid of Chapter 4 shown in figures 4.1 to 4.3. The black lines show the best Gumbel fit to the data whose probability density function is given by $f(v) = \frac{1}{\sigma} \exp\left(-\frac{v-\mu}{\sigma} - \exp\left(-\frac{v-\mu}{\sigma}\right)\right)$, where μ and σ are location (mode) and scale parameters of the distribution.

explain the large fraction of chemically peculiar stars in GCs, as well the observed distribution for the current mass and the half-mass radius of the Galactic GCs. Assuming that all Galactic GCs have undergone gas expulsion induced mass-loss, we found an upper limit of $10^5 \, \mathrm{yr}$ for the gas expulsion time scale. In addition, we found that the typical initial stellar masses, half-mass radii and the initial mass of the primordial gas left in the Galactic GCs need to be around $10^6 \, \mathrm{M_\odot}$, $1.0 \, \mathrm{pc}$ and $10^6 \, \mathrm{M_\odot}$ respectively, so the total mass of each cluster is $\sim 2 \times 10^6 \, \mathrm{M_\odot}$.

To estimate the mass-loss from Fornax as a result of gas expulsion in Fornax GCs, we use the grid of N-body simulations from Chapter 4 illustrated in figures 4.1 to 4.3. Our assumption is that the initial mass and half mass radii of Fornax GCs are similar to those of Galactic GCs, i.e. $R_\mathrm{h} = 1.0 \, \mathrm{pc}$ and $M_\mathrm{c} = 2 \times 10^6 \, \mathrm{M_\odot}$. We then need the ratio of tidal radii of the GCs to their half-mass radii to completely identify the location of Fornax GCs in the N-body grid of Chapter 4. To calculate the tidal radii of Fornax GCs on can repeat the same procedure as Section 5.1.2. However, for Fornax only the matter distribution $\rho(r)$ is given in an analytical form. As a result equations (5.3) and (5.4) are not suitable in this case as they require the potential to be known.

To derive the potential from $\rho(r)$, one needs numerical integration followed by a numerical second order differentiation to find tidal radii which can be a cumbersome and error-prone process. As a result, we simplify equation (5.3) for the case that only $\rho(r)$. We start from Poisson's equation, assuming spherical symmetry for the density

$$\nabla^2\phi(r) = 4\pi G\rho(r) \rightarrow \frac{1}{r^2}\frac{d}{dr}\left(r^2\frac{d\phi(r)}{dr}\right) = 4\pi G\rho(r) \tag{5.8}$$

Expanding this equation yields

$$\frac{d^2\phi(r)}{dr^2} + \frac{2}{r}\frac{d\phi(r)}{dr} = 4\pi G\rho(r) \tag{5.9}$$

where $d\phi(r)/dr$ is simply the magnitude of acceleration at radius r and can be written in terms of the enclosed mass $M(r)$

$$\frac{d\phi(r)}{dr} = G\frac{M(r)}{r^2} \tag{5.10}$$

The first derivative of potential with respect to x_i is

$$\frac{\partial\phi(r)}{\partial x_i} = \frac{d\phi(r)}{dr}\frac{\partial r}{\partial x_i} \tag{5.11}$$

knowing that $\partial r/\partial x_i = x_i/r$, then the second derivative of ϕ will be

$$\frac{\partial^2\phi(r)}{\partial x_i^2} = \frac{d^2\phi(r)}{dr^2}\left(\frac{x_i}{r}\right)^2 + \left(\frac{1}{r} - \frac{x_i^2}{r^3}\right)\frac{d\phi(r)}{dr} \tag{5.12}$$

Substituting equation (5.12) into equation (5.4) yields

$$\lambda_{e,1} = \frac{1}{r}\frac{d\phi(r)}{dr} - \frac{d^2\phi(r)}{dr^2} \tag{5.13}$$

which can be simplified by replacing the first and second derivatives of potential with respect to r using equations (5.9) and (5.10)

$$\lambda_{e,1} = 3G\frac{M(r)}{r^3} - 4\pi G\rho(r) \tag{5.14}$$

Hence the tidal radius of a stellar system with mass $M_{\rm c}$, located at distance $R_{\rm G}$ from the centre

of the host galaxy will be

$$R_\mathrm{t} = M_\mathrm{c}^{\frac{1}{3}} \left(3\frac{M(R_\mathrm{G})}{R_\mathrm{G}^3} - 4\pi\rho(R_\mathrm{G}) \right)^{-\frac{1}{3}} = M_\mathrm{c}^{\frac{1}{3}} \left(3\frac{\Omega(R_\mathrm{G})^2}{G} - 4\pi\rho(R_\mathrm{G}) \right)^{-\frac{1}{3}} \tag{5.15}$$

where $\Omega(R_\mathrm{G})$ is the orbital angular velocity at R_G

$$\Omega(R_\mathrm{G}) = \sqrt{G\frac{M(R_\mathrm{G})}{R_\mathrm{G}^3}}$$

Note that, when $\rho(r)$ is known, equation (5.15) only needs one integration, for the enclosed mass of the host galaxy within R_G, to calculate the tidal radius.

In equation (5.15) $M_\mathrm{c} = 2\times 10^6\,\mathrm{M_\odot}$ is the total mass of each cluster and $M(R_\mathrm{G})$ is the enclosed mass of Fornax within R_G and needs to be found by numerical integration. Using equation (5.15), we found that the tidal radii of our clusters in the tidal field of Fornax are larger than $100\,\mathrm{pc}$ for orbital radii $R > 0.5\,\mathrm{kpc}$ for all density profiles of Fornax. Such a large tidal radius corresponds to an almost isolated cluster as can be seen from figures 4.1 to 4.3. As a result we take the data of isolated clusters from the N-body grid of Chapter 4 and find the distribution of excess speeds for runaway stars. Figure 5.6 shows the normalized distribution of excess speeds for different gas expulsion time-scales. As it can been seen from this figure, lower gas expulsion time-scales lead to faster excess speeds. In addition, for $T_\mathrm{exp} \leq 10^5\,\mathrm{yr}$, they have a mean excess speed larger than $20\,\mathrm{km\,s^{-1}}$, indicating that it is possible to achieve a significant mass-loss with gas expulsion.

To determine the extent of mass-loss as a function of the gas expulsion time-scale and the orbital radii of GCs, we did an analysis as follows: For each runaway star we randomly draw a value from the excess speed distribution assuming a particular gas expulsion time-scale (Figure 5.6). We then find the velocity vector of the runaway star using its excess speed and a uniform spherical distribution for its orientation in space. We then add the velocity of the star to the velocity of the GC around Fornax at each radius (circular velocity) and the velocity of Fornax around the Milky Way. Finally, we derive the speed distribution of the runaway stars from their velocity vectors and convolve this distribution with our grid in Figure 5.5.

Figure 5.7 shows the mass-loss as a function of the GCs orbital radii and gas expulsion time-scales. As it can be seen from this figure, depending on the density profile of Fornax, the gas expulsion time-scale and the initial orbital radius of the cluster, mass-loss from Fornax varies from 30 to more than 90 per cent. As a result, with gas expulsion, it is possible that the majority of
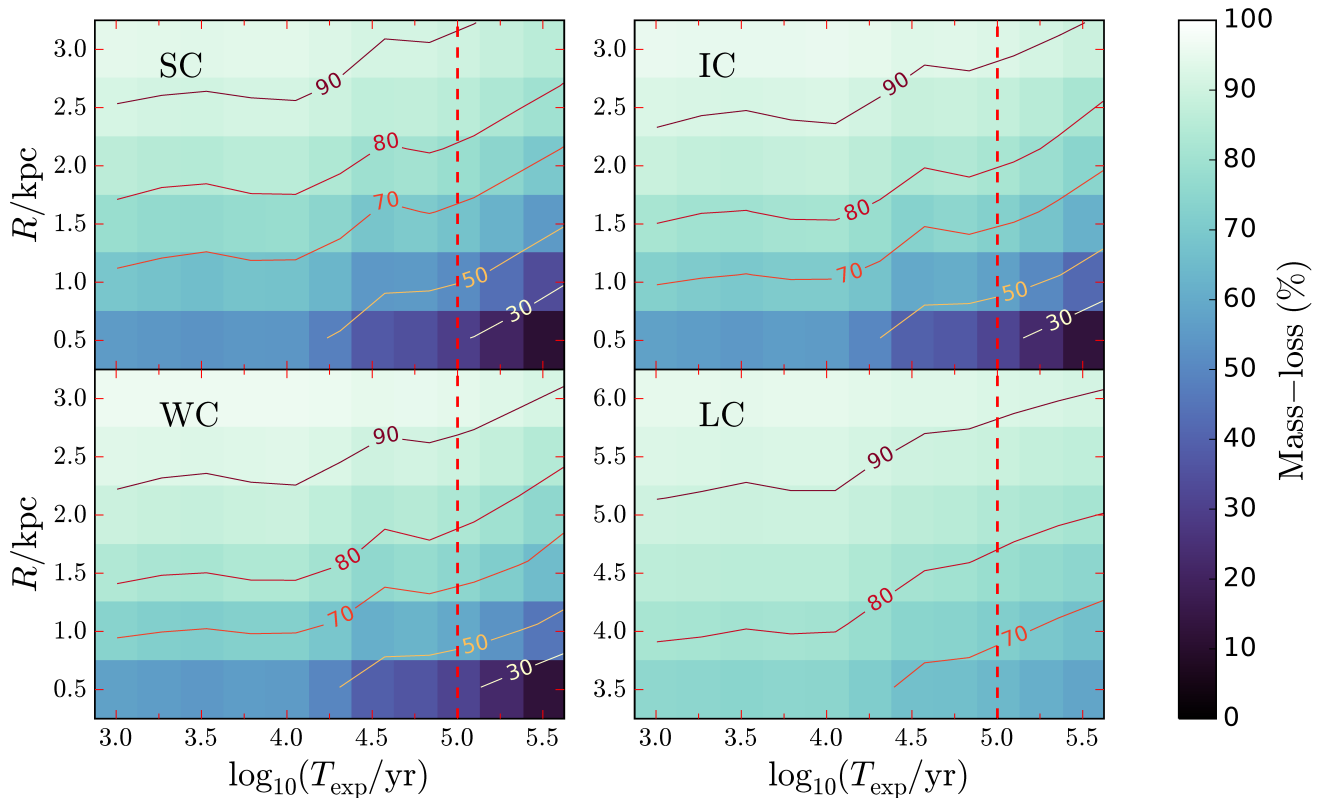
Figure 5.7: Mass-loss from Fornax as a function of cluster orbital radius and gas expulsion time-scale for different models. The LC model predicts a lower mass-loss compared to cuspy models for $R < 3.0\,\mathrm{kpc}$. The vertical dashed line marks the upper limit on gas expulsion time-scale found in Chapter 4.

the runaway stars leave the Fornax galaxy without contributing to the metallicity distribution of field stars. The implication of these results is further discussed in section 5.4.

5.3.2 Stellar evolution induced mass-loss

We compare the results obtained in Section 5.3.1 with the D'Ercole et al. (2008) models for clusters with $M_c = 10^6\,\mathrm{M_\odot}$ to find the typical excess speed of runaway stars which become unbound as a result of stellar evolution. D'Ercole et al. (2008) used hydrodynamical and N-body simulations, to model the formation and dynamical evolution of MSPs in GCs, based on the AGB scenario and the stellar evolution induced mass-loss caused by the SNe ejecta of primordial stars. In their models, GCs have King (1966) density profiles with core, half-mass and tidal radii of $R_c = 2.85$, $R_h \sim 10.3\,\mathrm{pc}$ and $R_t = 90\,\mathrm{pc}$ respectively and they lose a substantial amount of their mass during a period of $10 - 100$ dynamical times. These models can explain the large fraction of chemically peculiar stars in GCs. However, one needs very extended clusters ($R_h \sim 10.3\,\mathrm{pc}$) to

lose a substantial amount of mass.

To estimate the typical excess speed of runaway stars in D'Ercole et al. (2008) models, we take the typical excess speeds found in Section 5.3.1 and then scale them to the models of D'Ercole et al. (2008), using the mass and the radius of the clusters. The dynamical time-scale of a cluster and the velocity dispersion of its stars is proportional to $T_{\mathrm{dyn}} \propto M^{-1/2}R^{3/2}$ and $\sigma_v \propto (M/R)^{1/2}$ respectively. The models that we studied in Section 5.3.1 have $M_{\mathrm{c}} = 2 \times 10^6\,\mathrm{M_\odot}$, $R_{\mathrm{h}} = 1.0\,\mathrm{pc}$ and $T_{\mathrm{dyn}} = 3 \times 10^4\,\mathrm{yr}$. This corresponds to a mass and radius ratio of $M_{\mathrm{c}}(\mathrm{DE08})/M_{\mathrm{c}}(\mathrm{KB15}) = (10^6\,\mathrm{M_\odot})/(2 \times 10^6\,\mathrm{M_\odot}) = 0.5$ and $R_{\mathrm{h}}(\mathrm{DE08})/R_{\mathrm{h}}(\mathrm{KB15}) = (10.3\,\mathrm{pc})/(1.0\,\mathrm{pc}) = 10.3$ respectively, where DE08 and KB15 correspond to D'Ercole et al. (2008) models and our models from Chapter 4 (Khalaj & Baumgardt, 2015). As a result, the velocity dispersion of stars in D'Ercole et al. (2008) models is smaller than that of our model GCs from Chapter 4 by a factor of $(0.5/10.3)^{-1/2} \sim 4.5$, and the dynamical time-scale of the clusters is larger by a factor of $0.5^{-1/2} \times 10.3^{3/2} \sim 47$. In case of impulsive mass-loss, these values correspond to a mass-loss time-scale of at least $47 \times 3 \times 10^4\,\mathrm{yr} = 1.5\,\mathrm{Myr}$. In Figure 5.6, the dash-dotted curve corresponds to a gas expulsion time-scale of $T = 1.5\,\mathrm{Myr}$. According to this curve the typical excess speed of stars is $\sim 12\,\mathrm{km\,s^{-1}}$ for our model GCs from Chapter 4. We found that the velocity dispersion of stars in the models of D'Ercole et al. (2008) is smaller by a factor of ~ 4.5, this translates into a typical excess speed of $12/4.5 = 2.6\,\mathrm{km\,s^{-1}}$ for D'Ercole et al. (2008) models. Assuming that the unbound stars have a speed distribution similar to Figure 5.6 and applying the same procedure explained in Section 5.3.1, we obtain a mass-loss of less than $\sim 30\,\mathrm{per\,cent}$ from Fornax for $R = 3.0\,\mathrm{kpc}$ and cuspy models. This upper limit on mass-loss which is smaller for clusters with $R < 3.0\,\mathrm{kpc}$, is significantly lower than what we obtained for gas expulsion, indicating that the mechanism proposed by D'Ercole et al. (2008) is not efficient in expelling unbound stars from the Fornax dSph.

Here we have approximated the effect of stellar evolution induced mass-loss. Instead of this approximation, it is also possible to perform direct simulations of induced mass-loss, using e.g. NBODY6 (Aarseth, 2000), and obtain the speed distribution for runaway stars. However, the main conclusion, which is that the stellar evolution induced mass-loss is not effective to cause a significant mass-loss from Fornax, will not change. This is due to fact that the amount of mass-loss mainly depends on the mean of the speed distribution of runaway stars which simply scales as $\propto (M/R)^{1/2}$ and not the actual shape of the distribution. In fact, the mean of the speed distribution for stellar evolution induced mass-loss is so low ($\sim 2\,\mathrm{km\,s^{-1}}$) compared to gas expulsion ($\sim 30\,\mathrm{km\,s^{-1}}$), that the maximum mass-loss from Fornax achieved by stellar evolution

is still much lower than what is required for the significant mass-loss scenario to work and our aim has been to show this fact. As a result, obtaining the actual shape of the speed distribution for the stellar evolution induced mass-loss using direct N-body simulations is unnecessary as we have already shown by numerical approximation that this model does not work.

5.4   Summary

Using numerical orbit integration we determined the mass-loss from the Fornax dSph as a function of the initial speed and the initial distance of stars from the Fornax centre. We assumed a set of cuspy and cored models and tracked the trajectory of stars over a Hubble time. We then combined our results with those of D'Ercole et al. (2008) and Khalaj & Baumgardt (2015) to test whether significant mass-loss could have happened in Fornax GCs. Our results show that gas expulsion induced mass-loss in contrast to stellar evolution induced mass-loss can lead to large excess speeds for runaway stars and larger mass-loss from Fornax.

In particular, in case of gas expulsion induced mass-loss in GCs and for cuspy models when the orbital radii of GCs are between $2-3\,\text{kpc}$, a mass-loss of $\sim 90\,\text{per cent}$ can be achieved from Fornax. Comparing this result with the fact that Fornax GCs could have been 4-5 times more massive initially (Larsen et al., 2012), means that Fornax GCs could have lost a significant fraction ($> 90\,\text{per cent}$) of their initial mass and still yield a metallicity distribution of field stars which is consistent with observations. This result is especially important for Fornax 3 which is the most massive cluster in Fornax and imposes the tightest limit on the mass-loss from GCs in this galaxy.

In contrast, this is not the case for the LC model. GCs in this model, as shown by Cole et al. (2012) formed at the same radii as they are seen today ($R < 1.5\,\text{kpc}$) in which case the maximum mass-loss attained for LC model will be less than $50\,\text{per cent}$. A LC with $R_\text{c} \sim 1.5\,\text{kpc}$, overestimates the overall mass of the Fornax which is found to be $\sim 1-3 \times 10^8\,\text{M}_\odot$ by several studies (e.g. Irwin & Hatzidimitriou 1995; Walcher et al. 2003; Łokas 2009). In addition, Strigari et al. (2006) showed that such a LC for Fornax will be inconsistent with standard warm and dark matter models and predicts an unreasonably massive dark matter halo and a large asymptotic velocity of $200\,\text{km s}^{-1}$. However there are studies which prefer a cored model of $R_\text{c} \sim 1.0\,\text{kpc}$ (e.g. Amorisco et al. 2013) and it seems that different cored-cuspy models are possible to describe the dark matter profile of Fornax.

We showed that, if Fornax has a cuspy density profile or a small core, then it is possible to

reconcile the predictions of significant mass-loss scenario (Khalaj & Baumgardt, 2015) with the observed metallicity distribution of field stars in Fornax (Larsen et al., 2012).

We have done our simulations based on the assumption that the potential field of the Milky Way and Fornax are constant in time. This might not be true, especially for Fornax which has been suggested to be the remnant of a recent merging event (Coleman et al., 2004; Yozin & Bekki, 2012; del Pino et al., 2015). In such a case, the present-day metallicity distribution of field stars does not directly reflect the mass-loss history of GCs in Fornax and the upper limit for the initial mass of Fornax GCs estimated by Larsen et al. (2012) does not apply.

Finally, we would like to emphasize that despite being able to explain the observed metallicity distribution of field stars in Fornax, significant mass-loss due to gas expulsion still has some other problems as raised in Section 4.4.2. The most compelling of which is the strong anti-correlation between the fraction of SG stars and the current mass of GCs which is not supported by the observations. As a result, until one finds a solution to the anti-correlation problem, the feasibility of significant mass-loss due to gas expulsion is debated.

<div style="text-align: right; font-size: 4em;">6</div>

Conclusion

In this thesis I studied the formation and evolution of OCs and GCs using N-body simulations. The principal aims of the thesis were

- Devise a method to robustly identify the candidate members of OCs using astrometric and photometric data (from e.g. *Gaia*) and determine the mass function considering the effect of binaries

- Constrain the scenarios which have been proposed to explain the origin of MSPs and derive the initial conditions of GCs with MSPs according to different scenarios

In the following sections, I will explain how in each chapter of the thesis I attempted to reach the aims above.

6.1   Mass function and binary fraction of Praesepe

In Chapter 2 I devised a novel method to find the mass function and binary fraction of OCs. My method was based on a maximum likelihood method (to find the slope of the mass-function and its error) in combination with a K-S test to evaluate the goodness of fit. The devised method gives unbiased values for the power-law index (even when the number of data points is low), in contrast to the often used least squares methods. I tested my method on Praesepe as an example of a young Galactic OC. To find the candidate members of this cluster, I used the astrometric (positions and proper motions) and photometric data (J, K_s bands) of the PPMXL catalogue combined with the z photometry from the SDSS DR9. To find the true binary fraction and correct the observed

mass function for the effect of unresolved binaries, I ran a series of MC simulations. We generated synthetic isochrones of star clusters assuming a multi-stage power-law IMF with different indices for low and high mass stars, non-random pairing of the binary components as well as taking into account the photometric errors of stars in the PPMXL. I then compared the observed CMD of Praesepe with synthetic isochrones and changed the IMF power-law indices until the best match in terms of the K-S statistic with the observed mass function and the observed binary fraction was found. My method is ideally suited to be used together with data from *GAIA* and has been also used for Alpha Per using PPMXL and WISE data.

Using my method, I derived a true binary fraction of $\sim 35 \pm 5$ per cent in the mass range $0.6 < m/\mathrm{M}_\odot < 2.20$ which is consistent with the value obtained from direct observations of binaries in Praesepe (30 ± 5 per cent; Bouvier et al. 2001). The advantage of our method over direct observation of binaries is that we derive the binary fraction using the already available photometric data, without requiring any follow-up observations with special optics to resolve the binaries visually or spectroscopically.

6.2 Solutions to the mass-budget problem

I studied the so-called mass-budget problem for GCs with MSPs in Chapter 3. I examined the top-heavy IMF and significant mass-loss as two possible solutions to the mass-budget problem. In particular, using synthetic isochrones I evolved models of GCs with two stellar populations and calculated M/L ratios of GCs as well as the fraction of chemically peculiar (SG) stars. In my models, I varied the high-mass slope (α_{high}) of the IMF as well as the mass-loss level from stars with normal abundances. I assumed different retention fractions for white dwarfs and dark remnants and derived the following constraints on the solutions to the mass-budget problem

- Assuming that the IMF is canonical, to explain the large fraction of SG stars the cluster needs to lose 0.85 ± 0.05 and 0.90 ± 0.05 of its FG stars in the AGB and the FRMS scenarios respectively.

- Assuming that there is no mass-loss, in the AGB and the FRMS scenario one needs a high-mass slope of $\alpha_{\mathrm{high}} = 1.40 \pm 0.30$ and $\alpha_{\mathrm{high}} = 1.75 \pm 0.15$ respectively to explain the observed fraction of SG stars.

- Regardless of the assumed retention fraction for dark remnants, the M/L ratios obtained

from the FRMS scenario are consistent with those of Galactic GCs. For the AGB scenario, however, a top-heavy IMF is not enough and GCs need to lose at least $\sim 40\%$ of their stellar mass.

I also studied the effect of helium-enhancement on the observed number ratio of chemically peculiar stars for evolved stars. I found that helium-enhancement in conjunction with the fact that the mass function increases towards lower masses causes the number ratio of evolved SG stars to be higher than their actual number ratio (when they formed). For example, the boosting factor is approximately 1.3 for helium abundances of $Y \leq 0.35$ and increases for larger values of Y. As a result, for moderate values of Y this effect is negligible but for higher helium abundances one needs to consider this effect to infer the actual number of SG stars.

6.3   Constraints on MSPs based on the Galactic GCs

In Chapter 4, I showed that among all the possible mechanisms for significant mass-loss in GCs, namely stellar evolution, two-body relaxation, encounters with GMCs and primordial gas expulsion, only the last one can be a plausible and universal mechanism which can cause significant mass-loss in GCs. To see if primordial gas expulsion can really explain the large fraction of chemically peculiar stars in GCs with MSPs, I performed N-body simulations of GCs with two stellar populations evolving under the influence of primordial gas expulsion and an external tidal field. Using a series of MC simulations, I then compared the outcome of my N-body simulations with Galactic GCs and derived the initial conditions of GCs with MSPs which have undergone (rapid) gas expulsion induced mass-loss as well as (adiabatic) mass-loss induced by stellar evolution. My main results can be summarized as follows

- Primordial gas expulsion in conjunction with stellar evolution can explain the large fraction of chemically peculiar stars and today's masses and half-mass radii of Galactic GCs if (1) the initial mass of GCs were $\sim 10^6\,\mathrm{M_\odot}$, (2) the initial masses of the gas in GCs were of the same order, (3) the initial half-mass radii of the GCs were $\sim 1\,\mathrm{pc}$ and (4) the gas expulsion time-scale was less than $10^5\,\mathrm{yr}$ (about one initial crossing time).

- Such short gas expulsion time-scales cannot be reached by SN explosions, hence more energetic explosions such as hypernovae (Krause et al., 2016) are required to expel the gas. Accretion onto dark remnants such as black holes and neutron stars (Krause et al., 2012,

2013) can also provide enough energy to expel the gas over such a short time-scale, however, dark remnants are thought to become active after $\sim 30\,\mathrm{Myr}$ which is not consistent with the observations of young clusters, as they are shown to be gas free in less than $\sim 5\,\mathrm{Myr}$.

- Primordial gas expulsion leads to a pronounced anti-correlation between the fraction of chemically peculiar stars and the final mass of GCs which is not supported by observations. This can be considered as the most compelling evidence against significant mass-loss.

- If the significant mass-loss scenario is true and is due to gas expulsion, then it is expected that about 25% of all the GCs which have survived until today will have roughly an equal number of SG and FG stars.

The initial conditions that we derived for Galactic GCs in terms of the initial mass and half-mass radius correspond to initial birth densities of $\rho \sim 2 \times 10^6\,\mathrm{M}_\odot\,\mathrm{pc}^{-3}$ which lies in the expected range of $10^5 - 10^7\,\mathrm{M}_\odot\,\mathrm{pc}^{-3}$ derived by Marks & Kroupa (2010), meaning that our initial conditions are totally plausible. The fact that the total stellar mass and the mass of the gas in our best-fitting models are initially almost equal corresponds to star formation efficiencies of about SFE ~ 0.5. This is in agreement with Baumgardt & Kroupa (2007) who found that clusters who have survived from gas expulsion must have SFE $> 30\%$. However, the availability of a substantial amount of pristine gas in a cluster for the AGB scenario might be an issue. In the AGB scenario, SG stars form after SN explosions when dark remnants have expelled the primordial gas not accreted into stars from the clusters. As a result, the clusters need to accrete significant amounts of unprocessed new gas into their centres to start formation of SG stars, while at the same time preventing the dark remnants to immediately eject this gas. According to our scenario, when it finally happens, the gas expulsion has to be very rapid. At the moment it is completely unclear if and how this is possible. In addition, accretion of gas is only possible for clusters which move with a low relative velocity to a surrounding gaseous medium (Pflamm-Altenburg & Kroupa, 2006), however SG stars have been found in almost all massive GCs, independent of their orbits and position in the Milky Way. These problems do not exist in the FRMS scenario or any other scenario that form SG stars within a few Myr of the FG ones, since the gas out of which the SG forms is already in the cluster.

6.4   Constraints on MSPs based on the GCs of the Fornax dSph

In Chapter 5 I provided a solution to reconcile the observed metallicity distribution of GCs and field stars in Fornax with the significant mass-loss scenario. Larsen et al. (2012) found a large ratio of metal poor GCs to field stars in Fornax and showed that even under the most optimistic assumptions, the maximum mass-loss which could have happened by Fornax GCs is $\sim 80\%$. This is less than what is needed to explain the large fraction of chemically peculiar stars in GCs with MSPs, since most scenarios suggested require a mass-loss of $\sim 90\%$.

I did numerical orbit integration of runaway stars of Fornax GCs assuming different cored and cuspy models for the potential field of Fornax. I showed that if the Fornax dSph has a small core or a cuspy density profile and the runaway stars become unbound as a result of gas expulsion they can attain very high speeds ($\sim 100\,\mathrm{km\,s^{-1}}$) which exceeds the escape speed from Fornax ($\sim 20\,\mathrm{km\,s^{-1}}$). As a result, they can leave the potential field of Fornax and be stripped by the tidal force of the Milky Way.

This is however not the case if Fornax has a large core or runaway stars have become unbound by other mechanisms such as stellar evolution as proposed in the AGB scenario. I demonstrated that the exact escape rate and mass-loss from Fornax depends on the initial orbital radius of GCs and the gas expulsion time scale (Figure 5.7). Cole et al. (2012) showed that due to dynamical friction, GCs of Fornax move towards the centre of the galaxy after a Hubble time (in cuspy models) and based on their current observed distances from the center of Fornax, they should have initial orbital radii of $2 - 3\,\mathrm{kpc}$. This implies that mass-loss levels as high as $\sim 90\%$ can be achieved from Fornax in cuspy density profiles (for the large core model it is 50%). As a result, runaway stars will not contribute to the metallicity distribution of the field stars in Fornax and the limit calculated by Larsen et al. (2012) does not apply in this case. Whether significant mass-loss really happened in the GCs of the Fornax dSph can be further studied but my results conclusively show that one cannot interpret the metallicity distribution of Fornax as evidence against significant mass-loss, if mass-loss is due to gas expulsion.

6.5   Future work

Despite tremendous progress which has been made in the last decade in our knowledge about star clusters, there are still open questions in this field which await a comprehensive answer, for example the origin of MSPs or the universality of the IMF. With the launch of *Gaia* spacecraft and the ever-increasing power of computers, we are now closer than any time in the past to settle some of the ongoing debates in this field. Below I briefly suggest a number of possible research directions which can help us in this regard.

New stellar evolutionary routines with helium enhancement for N-body codes - All the simulations of GC evolution which have been done so far assume a single helium abundance of $Y \simeq 0.25$ for all stars. Moreover, the single and binary star evolution algorithms (e.g. Hurley et al. 2000, 2002) which are frequently used in N-body codes such as NBODY6 (Aarseth, 2000) are more than 20 years old. These models are by no means suitable for studying MSPs, since all the scenarios which have been proposed to explain the origin of MSPs predict a higher helium content for second generation stars which will significantly affect their evolution and lifetimes. Since dynamical evolution of a cluster is coupled to the evolution of its individual stars, it is important to incorporate stellar evolutionary tracks with enhanced helium stars (e.g. Chantereau et al. 2015), with N-body codes such as NBODY6. This enables us to obtain a better description of the long term evolution of star clusters. MESA [1] (Paxton et al., 2011, 2013, 2015) is a versatile set of modules using which the evolutionary tracks of single and binaries can be obtained (e.g. the MIST[2] project; Choi et al. 2016) and fed into N-body codes. The incorporation of new evolutionary tracks in N-body simulations, albeit being of vital importance, is not a trivial task. There are in fact uncertainties and reliability issues in the theoretical modeling of stellar evolution, i.e. isochrones, and the computer codes which deal with single and binary stars evolution. As an intermediate step toward having a better picture of the formation and evolution of MSPs, one can include the stellar evolution in the models which describe the early evolution phases of GCs with MSPs, a goal which has not been achieved yet. There are projects such as SEVN (Stellar EVolution N-body; see e.g. Spera et al. 2015) which have started to couple updated recipes for SN explosion (e.g. Fryer et al. 2012) and stellar evolution from PARSEC isochrones to N-body simulations.

Formation of GCs in the context of galaxy formation - According to the formation scenarios

---

[1]MESA (Modules for Experiments in Stellar Astrophysics) is available at http://mesa.sourceforge.net/

[2]MIST (MESA Isochrones and Stellar Tracks) is available at http://waps.cfa.harvard.edu/MIST/

of MSPs, chemically peculiar stars formed either within a few megayears of the formation of stars with normal abundance, i.e. FRMS scenario, or after a few tens of megayears when all SNe have gone off and have cleared the cluster from natal gas, i.e. the AGB scenario. If the latter is the case, then the cluster needs to accrete significant amounts of pristine gas at later stages of its evolution. One can perform realistic hydrodynamic simulations of galaxy collisions and merging which replicate the early stages of the formation of Milky Way and the environment in which GCs formed, to determine the amount of available gas for GCs to accrete (see Naiman et al. 2011) and turn into stars as they form and move through the interstellar medium in a realistic time dependent tidal field. The state-of-the-art Gadget code (Springel, 2005) or RAMSES code (Teyssier, 2002) can be used to perform the realistic galaxy collision and formation simulations combined with NBODY6TT (Renaud et al., 2011; Renaud & Gieles, 2013, 2015) to simulate GCs in arbitrary and variable tidal fields.

Coupling N-body and hydrodynamic simulations - The star formation efficiency in clusters is mainly below 100% and the gas is not completely consumed into stars. As a result, to be able to study the formation of star clusters through computer simulations, one cannot merely rely on N-body simulations. Primordial or residual gas plays a role in the dynamical evolution of star clusters which needs to be taken into account at least for the first few megayears when the gas is still present and has not been expelled. At the moment, in the N-body simulations of star clusters the effect of gas is simulated by adding an extra term to the total potential. This extra term is often time-dependent to mimic the effect of gas expulsion (e.g. Khalaj & Baumgardt 2015). However, this does not take into account the complex dynamics of the gas itself which is important for a detailed analysis of cluster formation and evolution. For example, a phenomenon such as Rayleigh–Taylor instability which is important in gas expulsion (see Krause et al. 2016) cannot be simulated this way. Therefore, one needs to couple N-body and hydrodynamic codes, e.g. NBODY6 with NIRVANA (Ziegler, 2008), to perform realistic simulations of star clusters. To achieve this goal, one can take advantage of an astrophysical software framework such as AMUSE[3] which allows coupling of different existing codes and is highly flexible.

Constraining the initial conditions of OCs and GCs using N-body simulations and *Gaia* data - *Gaia* enables us to improve the kinematic membership and distance measurements of star clusters by providing us with photometric data, proper motion and radial velocity of stars with an unprecedented accuracy. For example at $V = 15\,\text{mag}$, *Gaia*'s standard error in measuring proper

---

[3]AMUSE (Astrophysical Multipurpose Software Environment) is available at http://amusecode.orgcode

motion is $1.4 \times 10^{-5}\,\mathrm{mas\,yr^{-1}}$ (de Bruijne et al., 2014). For clusters located at distances $d = 1.5\,\mathrm{kpc}$ (distance of many OCs) and $d = 5\,\mathrm{kpc}$ (distance of 47 Tuc) this translates into a standard error of $0.1\,\mathrm{km\,s^{-1}}$ and $0.33\,\mathrm{km\,s^{-1}}$ respectively. The internal velocity dispersion of OCs and GCs are of the order of $0.5 - 5.0\,\mathrm{km\,s^{-1}}$ and $5 - 15\,\mathrm{km\,s^{-1}}$, this allows us to confidently find the members of OCs and determine their parameters such as IMF very accurately as well as detecting the internal structure of GCs. Note that MSPs in some GCs show different spatial and kinematic signatures (e.g. 47 Tuc; Kučinskas et al. 2014). As a result one can perform N-body simulations of star clusters with different initial conditions and compare the outcome of the simulations with *Gaia* data to better constrain the scenarios proposed to explain the formation and evolution of MSPs in GCs.

References

Aarseth S. J., 1963, MNRAS, 126, 223

Aarseth S. J., 2000, Advanced Series in Astrophysics and Cosmology, 10, 286

Aarseth S. J., 2003, Gravitational N-Body Simulations

Aarseth S. J., Lin D. N. C., Palmer P. L., 1993, ApJ, 403, 351

Adams J. D., Stauffer J. R., Skrutskie M. F., Monet D. G., Portegies Zwart S. F., Janes K. A., Beichman C. A., 2002, AJ, 124, 1570

Ahn C. P., et al., 2012, ApJS, 203, 21

Allard F., Homeier D., Freytag B., 2011, in Johns-Krull C., Browning M. K., West A. A., eds, Astronomical Society of the Pacific Conference Series Vol. 448, 16th Cambridge Workshop on Cool Stars, Stellar Systems, and the Sun. p. 91 (arXiv:1011.5405)

Alves D. R., Nelson C. A., 2000, ApJ, 542, 789

Amorisco N. C., Agnello A., Evans N. W., 2013, MNRAS, 429, L89

An D., Terndrup D. M., Pinsonneault M. H., Paulson D. B., Hanson R. B., Stauffer J. R., 2007, ApJ, 655, 233

Ashman K. M., Zepf S. E., 1992, in American Astronomical Society Meeting Abstracts. p. 1186

Assmann P., Fellhauer M., Kroupa P., Brüns R. C., Smith R., 2011, MNRAS, 415, 1280

Baker D. E. A., Jameson R. F., Casewell S. L., Deacon N., Lodieu N., Hambly N., 2010, MNRAS, 408, 2457

Bastian N., Lardo C., 2015, MNRAS, 453, 357

Bastian N., Lamers H. J. G. L. M., de Mink S. E., Longmore S. N., Goodwin S. P., Gieles M., 2013, MNRAS, 436, 2398

Bastian N., Hollyhead K., Cabrera-Ziri I., 2014, MNRAS, 445, 378

Bastian N., Cabrera-Ziri I., Salaris M., 2015, MNRAS, 449, 3333

Bate M. R., 2009, MNRAS, 392, 590

Baumgardt H., 2001, MNRAS, 325, 1323

Baumgardt H., Kroupa P., 2007, MNRAS, 380, 1589

Baumgardt H., Makino J., 2003, MNRAS, 340, 227

Baumgardt H., Kroupa P., Parmentier G., 2008, MNRAS, 384, 1231

Bedin L. R., Piotto G., Anderson J., Cassisi S., King I. R., Momany Y., Carraro G., 2004, ApJ, 605, L125

Bellini A., Piotto G., Bedin L. R., King I. R., Anderson J., Milone A. P., Momany Y., 2009, A&A, 507, 1393

Bertin G., Varri A. L., 2008, ApJ, 689, 1005

Binney J., Tremaine S., 2011, Galactic Dynamics: (Second Edition). Princeton Series in Astrophysics, Princeton University Press, https://books.google.com/books?id=6mF4CKxlbLsC

Boesgaard A. M., 1989, ApJ, 336, 798

Boesgaard A. M., Budge K. G., 1988, ApJ, 332, 410

Boudreault S., Bailer-Jones C. A. L., Goldman B., Henning T., Caballero J. A., 2010, VizieR Online Data Catalog, 351

Boudreault S., Lodieu N., Deacon N. R., Hambly N. C., 2012, MNRAS, 426, 3419

Bouvier J., Duchêne G., Mermilliod J.-C., Simon T., 2001, A&A, 375, 989

Bragaglia A., Carretta E., Gratton R., D'Orazi V., Lucatello S., Sneden C., 2013, Mem. Soc. Astron. Italiana, 84, 24

Bragaglia A., Sneden C., Carretta E., Gratton R. G., Lucatello S., Bernath P. F., Brooke J. S. A., Ram R. S., 2014, ApJ, 796, 68

Bressan A., Marigo P., Girardi L., Salasnich B., Dal Cero C., Rubele S., Nanni A., 2012, MNRAS, 427, 127

Brodie J. P., Strader J., 2006, ARA&A, 44, 193

Carretta E., 2013, A&A, 557, A128

Carretta E., et al., 2009, A&A, 505, 117

Carretta E., Bragaglia A., Gratton R. G., Recio-Blanco A., Lucatello S., D'Orazi V., Cassisi S., 2010, A&A, 516, A55

Carretta E., Lucatello S., Gratton R. G., Bragaglia A., D'Orazi V., 2011, A&A, 533, A69

Carretta E., et al., 2014, A&A, 564, A60

Carretta E., et al., 2015, A&A, 578, A116

Casertano S., Hut P., 1985, ApJ, 298, 80

Chabrier G., 2003, PASP, 115, 763

Chantereau W., Charbonnel C., Decressin T., 2015, A&A, 578, A117

Chantereau W., Charbonnel C., Meynet G., 2016, preprint, (arXiv:1606.01899)

Chappelle R. J., Pinfield D. J., Steele I. A., Dobbie P. D., Magazzù A., 2005, MNRAS, 361, 1323

Charbonnel C., Chantereau W., Decressin T., Meynet G., Schaerer D., 2013, A&A, 557, L17

Chen Y., Girardi L., Bressan A., Marigo P., Barbieri M., Kong X., 2014, MNRAS, 444, 2525

Choi J., Dotter A., Conroy C., Cantiello M., Paxton B., Johnson B. D., 2016, ApJ, 823, 102

Clauset A., Rohilla Shalizi C., Newman M. E. J., 2007, preprint, (arXiv:0706.1062)

Cohn H., 1979, ApJ, 234, 1036

Cole D. R., Dehnen W., Read J. I., Wilkinson M. I., 2012, MNRAS, 426, 601

Coleman M., Da Costa G. S., Bland-Hawthorn J., Martínez-Delgado D., Freeman K. C., Malin D., 2004, AJ, 127, 832

Conroy C., Spergel D. N., 2011, ApJ, 726, 36

D'Antona F., Caloi V., 2004, ApJ, 611, 871

D'Antona F., Caloi V., 2008, MNRAS, 390, 693

D'Antona F., Caloi V., D'Ercole A., Tailo M., Vesperini E., Ventura P., Di Criscienzo M., 2013, MNRAS, 434, 1138

D'Ercole A., Vesperini E., D'Antona F., McMillan S. L. W., Recchi S., 2008, MNRAS, 391, 825

D'Ercole A., D'Antona F., Ventura P., Vesperini E., McMillan S. L. W., 2010, MNRAS, 407, 854

Dabringhausen J., Kroupa P., Baumgardt H., 2009, MNRAS, 394, 1529

Dalessandro E., et al., 2014, ApJ, 791, L4

Davis D. S., Richer H. B., King I. R., Anderson J., Coffey J., Fahlman G. G., Hurley J., Kalirai J. S., 2008, MNRAS, 383, L20

Decressin T., Meynet G., Charbonnel C., Prantzos N., Ekström S., 2007a, A&A, 464, 1029

Decressin T., Charbonnel C., Meynet G., 2007b, A&A, 475, 859

Decressin T., Baumgardt H., Kroupa P., 2008, A&A, 492, 101

Decressin T., Baumgardt H., Charbonnel C., Kroupa P., 2010, A&A, 516, A73

Denissenkov P. A., Hartwick F. D. A., 2014, MNRAS, 437, L21

Dotter A., Chaboyer B., Jevremović D., Kostov V., Baron E., Ferguson J. W., 2008, ApJS, 178, 89

Ebisuzaki T., Fukushige T., Funato Y., Makino J., Taiji M., Hachisu I., Sugimoto D., 1993, in American Astronomical Society Meeting Abstracts #182. p. 813

Fan X., et al., 1996, AJ, 112, 628

Feiden G. A., Chaboyer B., Dotter A., 2011, ApJ, 740, L25

Fisher R. A., 1922, Philosophical Transactions of the Royal Society of London Series A, 222, 309

Fossati L., Bagnulo S., Landstreet J., Wade G., Kochukhov O., Monier R., Weiss W., Gebran M., 2008, A&A, 483, 891

Friel E. D., Boesgaard A. M., 1992, ApJ, 387, 170

Fryer C. L., Belczynski K., Wiktorowicz G., Dominik M., Kalogera V., Holz D. E., 2012, ApJ, 749, 91

Gieles M., Portegies Zwart S. F., Baumgardt H., Athanassoula E., Lamers H. J. G. L. M., Sipior M., Leenaarts J., 2006, MNRAS, 371, 793

Gieles M., Baumgardt H., Heggie D. C., Lamers H. J. G. L. M., 2010, MNRAS, 408, L16

Giersz M., Heggie D. C., 1997, MNRAS, 286, 709

Giersz M., Heggie D. C., Hurley J. R., 2008, MNRAS, 388, 429

Giersz M., Heggie D. C., Hurley J. R., Hypki A., 2013, MNRAS, 431, 2184

Giersz M., Leigh N., Marks M., Hypki A., Askar A., 2014, preprint, (arXiv:1411.7603)

Giersz M., Leigh N., Hypki A., Lützgendorf N., Askar A., 2015, MNRAS, 454, 3150

Girardi L., et al., 2010, ApJ, 724, 1030

Gnedin O. Y., Ostriker J. P., 1997, ApJ, 474, 223

Gnedin O. Y., Lee H. M., Ostriker J. P., 1999, ApJ, 522, 935

Gnedin O. Y., Zhao H., Pringle J. E., Fall S. M., Livio M., Meylan G., 2002, ApJ, 568, L23

Goldsbury R., Richer H. B., Anderson J., Dotter A., Sarajedini A., Woodley K., 2010, AJ, 140, 1830

González-García B. M., Zapatero Osorio M. R., Béjar V. J. S., Bihain G., Barrado Y Navascués D., Caballero J. A., Morales-Calderón M., 2006, A&A, 460, 799

Goodman J., Hut P., 1989, Nature, 339, 40

Gouliermis D., Keller S. C., Kontizas M., Kontizas E., Bellas-Velidis I., 2004, A&A, 416, 137

Gratton R., Sneden C., Carretta E., 2004, ARA&A, 42, 385

Gratton R. G., et al., 2013, A&A, 549, A41

Guszejnov D., Hopkins P. F., 2015, MNRAS, 450, 4137

Hambly N. C., Steele I. A., Hawkins M. R. S., Jameson R. F., 1995, MNRAS, 273, 505

Harris W. E., 1996, AJ, 112, 1487

Hasani Zonoozi A., Haghi H., Kroupa P., 2016, preprint, (arXiv:1605.04913)

Hauschildt P. H., Allard F., Baron E., 1999, ApJ, 512, 377

Heggie D. C., Ramamani N., 1989, MNRAS, 237, 757

Heggie D. C., Inagaki S., McMillan S. L. W., 1994, MNRAS, 271, 706

Hénon M. H., 1971, Ap&SS, 14, 151

Hillenbrand L. A., Hartmann L. W., 1998, ApJ, 492, 540

Hills J. G., 1980, ApJ, 235, 986

Hollyhead K., Bastian N., Adamo A., Silva-Villa E., Dale J., Ryon J. E., Gazak Z., 2015, MNRAS, 449, 1106

Holmberg E., 1941, ApJ, 94, 385

Hurley J., Tout C. A., 1998, MNRAS, 300, 977

Hurley J. R., Pols O. R., Tout C. A., 2000, MNRAS, 315, 543

Hurley J. R., Tout C. A., Pols O. R., 2002, MNRAS, 329, 897

Hurley J. R., Pols O. R., Aarseth S. J., Tout C. A., 2005, MNRAS, 363, 293

Hut P., Makino J., McMillan S., 1995, ApJ, 443, L93

Irrgang A., Wilcox B., Tucker E., Schiefelbein L., 2013, A&A, 549, A137

Irwin M., Hatzidimitriou D., 1995, MNRAS, 277, 1354

Ito T., Makino J., Ebisuzaki T., Sugimoto D., 1990, Computer Physics Communications, 60, 187

Janka H.-T., 2013, MNRAS, 434, 1355

Ji J., Bregman J. N., 2013, ApJ, 768, 158

Jones B. F., Cudworth K., 1983, AJ, 88, 215

Jones B. F., Stauffer J. R., 1991, AJ, 102, 1080

Joshi K. J., 2000, PhD thesis, MASSACHUSETTS INSTITUTE OF TECHNOLOGY

Kacharov N., Koch A., McWilliam A., 2013, A&A, 554, A81

Kalirai J. S., Hansen B. M. S., Kelson D. D., Reitzel D. B., Rich R. M., Richer H. B., 2008, ApJ, 676, 594

Khalaj P., Baumgardt H., 2013, MNRAS, 434, 3236

Khalaj P., Baumgardt H., 2015, MNRAS, 452, 924

Khalaj P., Baumgardt H., 2016, MNRAS, 457, 479

King I. R., 1966, AJ, 71, 64

Klein Wassink W. J., 1927, Publications of the Kapteyn Astronomical Laboratory Groningen, 41, 1

Kouwenhoven M. B. N., de Grijs R., 2008, A&A, 480, 103

Kouwenhoven M. B. N., de Grijs R., 2009, Ap&SS, 324, 171

Kouwenhoven M. B. N., Goodwin S. P., de Grijs R., Rose M., Kim S. S., 2014, MNRAS, 445, 2256

Kraus A. L., Hillenbrand L. A., 2007, AJ, 134, 2340

Krause M., Charbonnel C., Decressin T., Meynet G., Prantzos N., Diehl R., 2012, A&A, 546, L5

Krause M., Charbonnel C., Decressin T., Meynet G., Prantzos N., 2013, A&A, 552, A121

Krause M. G. H., Charbonnel C., Bastian N., Diehl R., 2016, A&A, 587, A53

Krauss L. M., Chaboyer B., 2003, Science, 299, 65

Kroupa P., 2001, MNRAS, 322, 231

Kroupa P., 2005, in Turon C., O'Flaherty K. S., Perryman M. A. C., eds, ESA Special Publication Vol. 576, The Three-Dimensional Universe with Gaia. p. 629 (arXiv:astro-ph/0412069)

Kroupa P., Weidner C., 2003, ApJ, 598, 1076

Küpper A. H. W., Kroupa P., Baumgardt H., Heggie D. C., 2010, MNRAS, 407, 2241

Kučinskas A., Dobrovolskas V., Bonifacio P., 2014, A&A, 568, L4

Lada C. J., Lada E. A., 2003, ARA&A, 41, 57

Lagarde N., Decressin T., Charbonnel C., Eggenberger P., Ekström S., Palacios A., 2012, A&A, 543, A108

Lamers H. J. G. L. M., Baumgardt H., Gieles M., 2010, MNRAS, 409, 305

Lardo C., Bellazzini M., Pancino E., Carretta E., Bragaglia A., Dalessandro E., 2011, A&A, 525, A114

Larsen S. S., Strader J., Brodie J. P., 2012, A&A, 544, L14

Larsen S. S., Brodie J. P., Forbes D. A., Strader J., 2014a, A&A, 565, A98

Larsen S. S., Brodie J. P., Grundahl F., Strader J., 2014b, ApJ, 797, 15

Larsen S. S., Baumgardt H., Bastian N., Brodie J. P., Grundahl F., Strader J., 2015, ApJ, 804, 71

Łokas E. L., 2009, MNRAS, 394, L102

Lyne A. G., Lorimer D. R., 1994, Nature, 369, 127

Lynga G., 1995, VizieR Online Data Catalog, 7092

Mackey A. D., Gilmore G. F., 2003, MNRAS, 340, 175

Madsen S., Dravins D., Lindegren L., 2002, A&A, 381, 446

Maeder A., Meynet G., 2006, A&A, 448, L37

Makino J., Fukushige T., Koga M., Namura K., 2003, PASJ, 55, 1163

Marigo P., Girardi L., Bressan A., Groenewegen M. A. T., Silva L., Granato G. L., 2008, A&A, 482, 883

Marigo P., Bressan A., Nanni A., Girardi L., Pumo M. L., 2013, MNRAS, 434, 488

Marino A. F., Villanova S., Milone A. P., Piotto G., Lind K., Geisler D., Stetson P. B., 2011, ApJ, 730, L16

Marino A. F., et al., 2012, A&A, 541, A15

Marks M., Kroupa P., 2010, MNRAS, 406, 2000

Marks M., Kroupa P., Dabringhausen J., Pawlowski M. S., 2012, MNRAS, 422, 2246

Mashchenko S., Sills A., 2005, ApJ, 619, 243

Massey P., Johnson K. E., Degioia-Eastwood K., 1995, ApJ, 454, 151

McMillan P. J., 2011, MNRAS, 414, 2446

Meza A., Navarro J. F., Abadi M. G., Steinmetz M., 2005, MNRAS, 359, 93

Milone A. P., et al., 2008, ApJ, 673, 241

Milone A. P., et al., 2012a, ApJ, 744, 58

Milone A. P., Marino A. F., Piotto G., Bedin L. R., Anderson J., Aparicio A., Cassisi S., Rich R. M., 2012b, ApJ, 745, 27

Milone A. P., et al., 2012c, ApJ, 754, L34

Minniti D., Peterson R. C., Geisler D., Claria J. J., 1996, ApJ, 470, 953

Monet D. G., et al., 2003, AJ, 125, 984

Moreno E., Pichardo B., Velázquez H., 2014, ApJ, 793, 110

Muench A. A., Lada E. A., Lada C. J., Alves J., 2002, ApJ, 573, 366

Naiman J. P., Ramirez-Ruiz E., Lin D. N. C., 2011, ApJ, 735, 25

Nataf D. M., Gould A., Pinsonneault M. H., Stetson P. B., 2011, ApJ, 736, 94

Nitadori K., Aarseth S. J., 2012, MNRAS, 424, 545

Pace G., Pasquini L., François P., 2008, A&A, 489, 403

Palacios A., Charbonnel C., Talon S., Siess L., 2006, A&A, 453, 261

Pancino E., Carrera R., Rossetti E., Gallart C., 2010, Chemical abundance analysis of the open clusters Cr 110, NGC 2099 (M 37), NGC 2420, NGC 7789, and M 67 (NGC 2682) (arXiv:0910.0723), doi:10.1051/0004-6361/200912965

Parker R. J., Goodwin S. P., 2007, MNRAS, 380, 1271

Parker R. J., Goodwin S. P., Wright N. J., Meyer M. R., Quanz S. P., 2016, MNRAS,

Parmentier G., Gilmore G., 2007, MNRAS, 377, 352

Parmentier G., Gilmore G., 2008, in Vesperini E., Giersz M., Sills A., eds, IAU Symposium Vol. 246, IAU Symposium. pp 413–417, doi:10.1017/S1743921308016062

Pattabiraman B., Umbreit S., Liao W.-k., Choudhary A., Kalogera V., Memik G., Rasio F. A., 2013, ApJS, 204, 15

Pawlowski M. S., Kroupa P., 2013, MNRAS, 435, 2116

Paxton B., Bildsten L., Dotter A., Herwig F., Lesaffre P., Timmes F., 2011, ApJS, 192, 3

Paxton B., et al., 2013, ApJS, 208, 4

Paxton B., et al., 2015, ApJS, 220, 15

Pelupessy F. I., van Elteren A., de Vries N., McMillan S. L. W., Drost N., Portegies Zwart S. F., 2013, A&A, 557, A84

Pfeffer J., Griffen B. F., Baumgardt H., Hilker M., 2014, MNRAS, 444, 3670

Pflamm-Altenburg J., Kroupa P., 2006, MNRAS, 373, 295

Pinfield D. J., Hodgkin S. T., Jameson R. F., Cossburn M. R., von Hippel T., 1997, MNRAS, 287, 180

Piotto G., et al., 2007, ApJ, 661, L53

Piskunov A. E., Schilbach E., Kharchenko N. V., Röser S., Scholz R.-D., 2007, A&A, 468, 151

Plummer H. C., 1911, MNRAS, 71, 460

Portegies Zwart S. F., Baumgardt H., McMillan S. L. W., Makino J., Hut P., Ebisuzaki T., 2006, ApJ, 641, 319

Portegies Zwart S., et al., 2009, New Astron., 14, 369

Portegies Zwart S. F., McMillan S. L. W., Gieles M., 2010, ARA&A, 48, 431

Portegies Zwart S., McMillan S. L. W., van Elteren E., Pelupessy I., de Vries N., 2013, Computer Physics Communications, 183, 456

Prantzos N., Charbonnel C., 2006, A&A, 458, 135

Prieto J. L., Gnedin O. Y., 2008, ApJ, 689, 919

Renaud F., Gieles M., 2013, MNRAS, 431, L83

Renaud F., Gieles M., 2015, MNRAS, 448, 3416

Renaud F., Gieles M., Boily C. M., 2011, MNRAS, 418, 759

Renzini A., 2008, MNRAS, 391, 354

Repetto S., Davies M. B., Sigurdsson S., 2012, MNRAS, 425, 2799

Rey S.-C., Lee Y.-W., Ree C. H., Joo J.-M., Sohn Y.-J., Walker A. R., 2004, AJ, 127, 958

Richer H. B., Heyl J., Anderson J., Kalirai J. S., Shara M. M., Dotter A., Fahlman G. G., Rich R. M., 2013, ApJ, 771, L15

Roeser S., Demleitner M., Schilbach E., 2010, AJ, 139, 2440

Rosenfield P., Marigo P., Girardi L., Dalcanton J. J., Bressan A., Williams B. F., Dolphin A., 2016, ApJ, 822, 73

Röser S., Schilbach E., Piskunov A. E., Kharchenko N. V., Scholz R.-D., 2011, A&A, 531, A92

Salpeter E. E., 1955, ApJ, 121, 161

Sana H., Gosset E., Evans C. J., 2009, MNRAS, 400, 1479

Sana H., James G., Gosset E., 2011, MNRAS, 416, 817

Searle L., Zinn R., 1978, ApJ, 225, 357

Shanahan R. L., Gieles M., 2015, MNRAS, 448, L94

Sharp D. H., 1984, Physica D Nonlinear Phenomena, 12, 3

Siess L., Dufour E., Forestini M., 2000, A&A, 358, 593

Skrutskie M. F., et al., 2006, AJ, 131, 1163

Sneden C., Kraft R. P., Guhathakurta P., Peterson R. C., Fulbright J. P., 2004, AJ, 127, 2162

Sollima A., Beccari G., Ferraro F. R., Fusi Pecci F., Sarajedini A., 2007, MNRAS, 380, 781

Solomon P. M., Rivolo A. R., Barrett J., Yahil A., 1987, ApJ, 319, 730

Spera M., Mapelli M., Bressan A., 2015, MNRAS, 451, 4086

Springel V., 2005, MNRAS, 364, 1105

Strader J., Brodie J. P., Forbes D. A., Beasley M. A., Huchra J. P., 2003, AJ, 125, 1291

Strigari L. E., Bullock J. S., Kaplinghat M., Kravtsov A. V., Gnedin O. Y., Abazajian K., Klypin A. A., 2006, ApJ, 652, 306

Tang J., Bressan A., Rosenfield P., Slemer A., Marigo P., Girardi L., Bianchi L., 2014, MNRAS, 445, 4287

Taylor B. J., 2006, AJ, 132, 2453

Teyssier R., 2002, A&A, 385, 337

Valcarce A. A. R., Catelan M., 2011, A&A, 533, A120

Ventura P., D'Antona F., 2011, MNRAS, 410, 2760

Ventura P., D'Antona F., Mazzitelli I., Gratton R., 2001, ApJ, 550, L65

Vesperini E., Heggie D. C., 1997, MNRAS, 289, 898

Vesperini E., McMillan S. L. W., Portegies Zwart S., 2009, ApJ, 698, 615

Villanova S., Geisler D., Carraro G., Moni Bidin C., Muñoz C., 2013, ApJ, 778, 186

Walcher C. J., Fried J. W., Burkert A., Klessen R. S., 2003, A&A, 406, 847

Wang W., Boudreault S., Goldman B., Henning T., Caballero J. A., Bailer-Jones C. A. L., 2011, in Johns-Krull C., Browning M. K., West A. A., eds, Astronomical Society of the Pacific Conference Series Vol. 448, 16th Cambridge Workshop on Cool Stars, Stellar Systems, and the Sun. p. 761 (arXiv:1010.4091)

Wang L., Spurzem R., Aarseth S., Giersz M., Askar A., Berczik P., Naab T., Kouwenhoven R. S. M. B. N., 2016, MNRAS,

Webb J. J., Harris W. E., Sills A., Hurley J. R., 2013, ApJ, 764, 124

Webb J. J., Leigh N., Sills A., Harris W. E., Hurley J. R., 2014, MNRAS, 442, 1569

Whitmore B. C., Schweizer F., 1995, AJ, 109, 960

Whitmore B. C., Zhang Q., Leitherer C., Fall S. M., Schweizer F., Miller B. W., 1999, AJ, 118, 1551

Wielen R., 1985, in Goodman J., Hut P., eds, IAU Symposium Vol. 113, Dynamics of Star Clusters. pp 449–460

York D. G., et al., 2000, AJ, 120, 1579

Yozin C., Bekki K., 2012, ApJ, 756, L18

Ziegler U., 2008, Computer Physics Communications, 179, 227

Zonoozi A. H., Küpper A. H. W., Baumgardt H., Haghi H., Kroupa P., Hilker M., 2011, MNRAS, 411, 1989

Zonoozi A. H., Haghi H., Küpper A. H. W., Baumgardt H., Frank M. J., Kroupa P., 2014, MNRAS, 440, 3172

de Boer T. J. L., Fraser M., 2016, A&A, 590, A35

de Bruijne J. H. J., Rygl K. L. J., Antoja T., 2014, EAS Publications Series, 67, 23

de Grijs R., Johnson R. A., Gilmore G. F., Frayn C. M., 2002a, MNRAS, 331, 228

de Grijs R., Gilmore G. F., Johnson R. A., Mackey A. D., 2002b, MNRAS, 331, 245

de Mink S. E., Pols O. R., Langer N., Izzard R. G., 2009, A&A, 507, L1

del Pino A., Aparicio A., Hidalgo S. L., 2015, MNRAS, 454, 3996

van Leeuwen F., 2009, A&A, 497, 209

von Hoerner S., 1960, Z. Astrophys., 50, 184

von Hoerner S., 1963, Z. Astrophys., 57, 47